



# Numerical Modelling of Gas Foil Journal Bearings

Analysis of High-Pressure Lubrication  
Flows

Wessel de Waart

Technische Universiteit Delft

Cover Image: Peter Chapman (n.d.). [Gas Foil Bearings]. Retrieved June 2023, from <https://www.mechsol.com/blog/foil-bearings-technology-whose-time-has-come-part-1>

# Numerical Modelling of Gas Foil Journal Bearings

Analysis of High-Pressure Lubrication Flows

by

**Wessel de Waart**

in partial fulfillment of the requirements for the degree of

**Master of Science**  
in Aerospace Engineering

at the Delft University of Technology,  
to be defended publicly on August 25<sup>th</sup>, 2023 at 09:00 AM.

Supervisor:	Dr. ir. M. Pini,	TU Delft - Propulsion & Power
Thesis committee:	Prof. dr. ir. P. Colonna,	TU Delft - Propulsion & Power
	Dr. ir. M. Pini,	TU Delft - Propulsion & Power
	Dr. S. Hulshoff,	TU Delft - Aerodynamics

An electronic version of this thesis is available at <http://repository.tudelft.nl/>.



# Acknowledgements

This master's thesis is the result of nearly a year of research and forms the conclusion of my time as a master's student at the faculty of Aerospace Engineering at the TU Delft. The work presented in this manuscript has been preceded by several years of studying at the TU Delft both as a bachelor's and a master's student and I am very grateful to have had this opportunity.

First, I would like to extend my gratitude to my thesis supervisor, Dr. Ir. Matteo Pini, for his expertise and excellent guidance during my thesis work. Matteo patiently guided me through the process one step at a time, which was fundamental for the successful completion of the research. I would also like to acknowledge Ir. Matteo Majer and Ir. Andrea Giuffr  for their helpful feedback along the way. It has been a pleasure to have the opportunity to perform my master's thesis within the turbomachinery group.

This master's thesis would not have been possible without the patience and support of my parents, Sijmen and Corine, who have supported me during my education over the years. Finally, I would like to thank my family and friends, who I can always count on.

*Wessel de Waart  
Delft, June 2023*



# Abstract

In the pursuit of reducing the climate impact of aviation, there has been an increased interest in the adoption of renewable energy technologies. Examples of revolutionary technologies include hydrogen fuel cell systems and waste heat recovery using the organic Rankine cycle. The design of viable energy conversion systems for aviation poses unique challenges in terms of efficiency, weight and size. To this end, research on small-scale turbomachinery operating at high rotational speeds is increasingly pursued in the context of, for example, fuel cell air compressors or organic Rankine cycle turbines. Such machines typically call for oil-free operation to avoid contamination of the process fluid. Gas foil bearings can prove to be an enabling technology due to their reliability, oil-free operation and compatibility with high rotational speeds.

The use of gas foil bearings to support organic Rankine cycle turbines requires lubrication with complex working fluids at operating conditions near the saturated vapour line or thermodynamic critical point. Although there has been an increased interest in high-pressure gas lubrication in recent scientific literature, there is still a lack of understanding of the effects of non-ideal compressible flows on the performance of (gas foil) journal bearings. In order to further address this knowledge gap, this work focuses on the modelling of such bearings lubricated with dense fluids made by complex molecules like those adopted for waste heat recovery at high temperatures in aviation.

The compressible Reynolds equation governing the thin-film flow within the bearing is discretized using a finite difference method. The solution to the non-linear problem is obtained using a relaxation method in which a thermodynamic software program updates the non-ideal thermodynamic state properties after each iteration. The load-carrying capacity of the bearing is obtained by integrating the resulting steady-state pressure field around the rotor shaft. A perturbation method is applied to obtain the stiffness and damping coefficients used in a linearized rotor-dynamic analysis. The developed computational tool allows for the analysis of bearing performance under varying operating conditions.

The conclusions of this work emphasize the challenge of generating sufficient load-carrying capacity and rotor-dynamic stability associated with high-pressure gas lubrication in journal bearings. Bearings operating with compressible lubricants near the thermodynamic critical point are typically characterized by turbulent thin-film flows with non-negligible molecular interactions. Reduced peak pressures within the gas film are anticipated, resulting in a reduced load-carrying capacity as compared to ideal gas lubrication flows. It is shown that non-ideal thermodynamic effects have an impact on rotor-dynamic stability by affecting the steady-state attitude angle of the bearing.

The modelling of a gas foil journal bearing used to potentially support the turbine of the organic Rankine cycle hybrid integrated device (ORCHID) of the TU Delft has finally been considered. The results show the utility of a numerical model in assessing bearing performance and understanding the associated physics. This work can be used as a basis for future analysis and design of gas foil journal bearings lubricated with high-pressure process fluids.



# List of Figures

1.1	Exemplary process flow diagram of an ORC system.[1]	1
1.2	Schematic of a typical hydrodynamic journal bearing.	2
1.3	Schematic of a first generation gas foil journal bearing.[2]	3
1.4	Gas foil journal and thrust bearings designed by NASA.	4
2.1	Schematic figure showing a plain journal bearing.	8
2.2	Contour plot of the ratio of specif heats ( $\gamma$ ) for siloxane MM created using NiceProp.[3]	11
2.3	Example of a plot showing the relevance of thermal expansions on the density field for a particular bearing lubricated with siloxane MM at $\Lambda = 0.1$ .	14
2.4	Distance from the nearest wall for determining the Prandtl mixing length.	15
2.5	Schematic of a first-generation gas foil journal bearing.[2]	19
2.6	Schematic of a gas foil bearing where the bump foil is modelled using a simple elastic model.	20
2.7	Modelling of the bump foil structure by elastic springs. Local bump foil deflections are indicated with $w_d$ .	20
2.8	Simplified schematic of a rigid rotor supported on gas dynamic bearings.	22
2.9	Discretization of the fluid domain in circumferential and axial directions.	25
2.10	Convergence of non-dimensional load capacity and critical mass as function of grid refinement for $n = m$ and $n = 3m$ . Reference solution is computed with $n = 150$ and $m = 100$ .	26
2.11	Flow diagram of the solution procedure used to obtain the steady-state bearing properties.	27
2.12	Flow diagram of the solution procedure used to obtain the dynamic bearing properties.	28
3.1	Bearing operating conditions for R134a as used for verification plotted on the reduced T-s thermodynamic plane.	30
3.2	Verification of the mid-span pressure distribution for non-ideal and ideal gasses.	30
3.3	Verification of Load capacity ratio and steady-state eccentricity.	31
3.4	Verification of the laminar critical mass ratio.	31
3.5	Verification of the turbulent load capacity ratio at different Reynolds numbers.	32
3.6	Verification of the turbulent critical mass ratio.	33
3.7	Verification of the turbulent critical mass ratio using manually set excitation frequency ratio.	33
3.8	Bearing operating conditions for siloxane MM as considered in the current analysis plotted on the reduced T-s thermodynamic plane.	34
3.9	Schematic representation of the aerodynamic wedge action generating an increase in pressure.	35
3.10	Effect of increasing shaft eccentricity on non-dimensional load capacity for a bearing lubricated with siloxane MM at $\Lambda = 3.0$ .	35
3.11	Effect of increasing bearing compressibility number on mid-span pressure distribution for siloxane MM at $T_r = 1.1$ and $P_r = 0.5$ with $\epsilon = 0.7$ .	36
3.12	Effect of increasing bearing compressibility number on non-dimensional load capacity for a bearing lubricated with siloxane MM at $\epsilon = 0.2$ .	36
3.13	Mid-span non-dimensional density and pressure distributions for siloxane MM with $\Lambda = 3.0$ and $\epsilon = 0.7$ at different reduced reference pressures.	37
3.14	Effect of fluid compressibility on load capacity ratio for a bearing lubricated with siloxane MM at $\epsilon = 0.2$ .	38
3.15	Contour plots of non-dimensional bulk modulus on the T-s thermodynamic plane for siloxane MM.	38
3.16	Compressibility factor as a function of reduced pressure for siloxane MM.	39

3.17 Comparison between non-dimensional bulk modulus and compressibility factor for siloxane MM. . . . .	39
3.18 Dominant molecular interactions for different fluid regimes. . . . .	40
3.19 Inter-molecular forces as a function of distance between molecules. . . . .	40
3.20 Contours of load capacity ratio on the T-s thermodynamic plane for siloxane MM with $\epsilon = 0.2$ and $\Lambda = 3.0$ . . . . .	41
3.21 Compressibility factor and non-dimensional bulk modulus for fluids with different molecular complexities. . . . .	41
3.22 Saturation dome for fluids of different molecular complexity in the reduced T-s plane. . . . .	42
3.23 Contour plots of non-dimensional bulk modulus for hydrogen and carbon-dioxide. . . . .	42
3.24 Effects of bearing width on non-dimensional load capacity. . . . .	43
3.25 Herringbone grooved journal bearing of EPFL.[4] . . . . .	43
3.26 Analogy between bearing impedances and mechanical spring-damper systems. . . . .	44
3.27 Non-dimensional stiffness and damping coefficients for a bearing lubricated with siloxane MM at $T_r = 1.1$ and $P_r = 0.5$ with $\epsilon = 0.2$ . . . . .	44
3.28 Attitude angle as a function of compressibility number for a plain journal bearing lubricated with siloxane MM at $\epsilon = 0.2$ . . . . .	45
3.29 Schematic illustration of sub-synchronous whirling motions in a journal bearing. . . . .	45
3.30 Schematic of a bearing at attitude angle $\psi$ supporting an external load $W_{ext}$ . Regions 1 and 2 experience positive and negative circumferential pressure gradients, respectively. . . . .	46
3.31 Exaggerated velocity profiles over the film thickness for region 1 and 2 corresponding to positive and negative pressure gradients. . . . .	47
3.32 Non-dimensional critical mass as a function of bearing compressibility number at $\epsilon = 0.2$ for a bearing lubricated with siloxane MM. . . . .	47
3.33 Critical mass ratio as a function of bearing compressibility number at $\epsilon = 0.2$ . . . . .	48
3.34 Normalized attitude angle for siloxane MM at different operating conditions with $\epsilon = 0.2$ . . . . .	49
3.35 Contours of critical mass ratio on the T-s thermodynamic plane for siloxane MM with $\epsilon = 0.2$ at $\Lambda = 0.1$ and $\Lambda = 3.0$ . . . . .	49
3.36 Contour plots of normalized dynamic viscosity on the T-s thermodynamic plane relative to sea level pressure air. . . . .	50
3.37 Non-dimensional load capacity for siloxane MM at $T_r = 1.1$ and $P_r = 0.5$ with $\epsilon = 0.2$ for various ambient Reynolds numbers. . . . .	51
3.38 Qualitative shapes of the velocity profiles for laminar and turbulent Poiseuille and Couette flow. . . . .	52
3.39 Attitude angle for siloxane MM at $T_r = 1.1$ and $P_r = 0.5$ with $\epsilon = 0.2$ for various ambient Reynolds numbers. . . . .	52
3.40 Non-dimensional critical mass for siloxane MM at $T_r = 1.1$ and $P_r = 0.5$ with $\epsilon = 0.2$ for various ambient Reynolds numbers. . . . .	53
3.41 Non-dimensional direct and cross-coupled stiffness coefficients for a bearing lubricated with siloxane MM at $T_r = 1.1$ and $P_r = 0.5$ with $\epsilon = 0.2$ at various Reynolds numbers. . . . .	53
3.42 Non-dimensional direct and cross-coupled damping coefficients for a bearing lubricated with siloxane MM at $T_r = 1.1$ and $P_r = 0.5$ with $\epsilon = 0.2$ at various Reynolds numbers. . . . .	54
3.43 Load capacity and critical mass ratios for a bearing lubricated with siloxane MM at $T_r = 1.1$ and $P_r = 0.5$ with $\epsilon = 0.2$ at various Reynolds numbers. . . . .	54
3.44 Contours of load capacity and critical mass ratio on the reduced T-s thermodynamic plane for siloxane MM with $\epsilon = 0.2$ and $\Lambda = 3.0$ for turbulent flow at $Re = 15000$ . . . . .	55
4.1 Verification of the eccentricity, attitude angle and minimum film thickness versus load capacity for a gas foil journal bearing. . . . .	58
4.2 Verification of the direct and cross-coupled dimensional stiffness coefficients. . . . .	59
4.3 Verification of the direct damping coefficients. . . . .	59
4.4 Dimensional load capacity as a function of minimum film thickness for a gas foil bearing (GFB) and a plain journal bearing (PJB) at $\Lambda = 0.1$ and $\Lambda = 1.0$ for a nominal film thickness of $h_0 = 21.8\mu m$ . . . . .	60
4.5 Dimensional load capacity as a function of bearing speed number $\Lambda$ for a PJB and a GFB. . . . .	61
4.6 Attitude angle as a function of bearing speed number $\Lambda$ for a PJB and a GFB. . . . .	62

---

4.7	Non-dimensional critical mass as a function of bearing speed number $\Delta$ for a PJB and a GFB. . . . .	62
4.8	Assumed bearing operating conditions for siloxane MM for operation with the ORCHID turbine plotted on the reduced T-s thermodynamic plane. . . . .	63
4.9	Plot showing the validity of the assumptions of the compressible Reynolds equation for the GFB operating with siloxane MM at 98000 RPM. . . . .	64
4.10	Journal eccentricity, minimum film thickness and attitude angle versus load capacity for a gas foil journal bearing with suitable dimensions for operation with the ORCHID turbine. . . . .	65



# List of Tables

2.1	Summary of the different flow physics captured by the different forms of the Reynolds equation. . . . .	13
2.2	Form of the (Reynolds) equation used to solve for the perturbed film thickness and performance parameters of plain journal bearings and gas foil bearings. . . . .	24
2.3	Summary of the steps and equations involved in computing the steady-state load capacity of a gas foil bearing. . . . .	27
2.4	Summary of the steps and equations involved in computing the rotor-dynamic critical mass of a gas foil bearing. . . . .	28
4.1	Bearing parameters used in the work of Kim and San Andrés. [5] . . . . .	57
4.2	Bearing geometry and design operating conditions of the ORCHID turbine. . . . .	63



# List of Symbols

## Acronyms

<i>ACM</i>	Air cycle machine
<i>ECS</i>	Environmental control system
<i>GFB</i>	Gas foil bearing
<i>mORC</i>	Mini-organic Rankine cycle
<i>ORC</i>	Organic Rankine cycle
<i>ORCHID</i>	Organic Rankine Cycle Hybrid Integrated Device
<i>PEMFC</i>	Proton exchange membrane fuel cell
<i>PJB</i>	Plain journal bearing
<i>RANS</i>	Reynolds-averaged Navier-Stokes
<i>RPM</i>	Rotations per minute

## Symbols

$\vec{b}$	Right-hand-side vector of the finite difference linear system of equations
$\vec{q}$	Vector containing amplitudes of rotor motions
$\vec{v}$	Velocity vector
$A$	Matrix of the finite difference linear system of equations
$a$	Speed of sound
$Br$	Brinkman number
$c$	Damping coefficient
$c_p$	Isobaric specific heat
$D$	Bearing diameter
$e_{i,j}$	Strain-rate tensor
$Ec$	Eckert number
$G$	Grüneisen parameter
$G_{x,z}$	Turbulence correction factor in circumferential or axial direction
$h$	Film thickness or enthalpy
$k$	Stiffness coefficient, thermal conductivity or Prandtl mixing length constant
$K_f$	Bump foil structural stiffness per unit area
$L$	Bearing axial width
$M$	Mach number

$m$	Grid intervals in axial direction or mass
$M_{cr}$	Critical mass
$n$	Grid intervals in circumferential direction
$p$	Pressure
$Pr$	Prandtl number
$q$	Thermal conduction
$R$	Shaft radius or gas constant
$Re$	Reynolds number
$S$	Gas foil bearing compliance ratio
$s$	Entropy or Laplace variable
$T$	Temperature
$t$	Time
$u$	Component of velocity in x-direction or equivalent bearing stiffness
$v$	Component of velocity in y-direction or equivalent bearing damping
$W$	Load carrying capacity
$w$	Component of velocity in z-direction
$w_d$	Bump foil structural deflection
$X$	Bearing inertial coordinate
$x$	Spatial coordinate in circumferential direction
$Y$	Bearing inertial coordinate
$y$	Spatial coordinate in film thickness direction
$Z$	Bearing impedance or compressibility factor
$z$	Spatial coordinate in axial direction

### **Greek Symbols**

$\alpha$	Isobaric expansion coefficient
$\alpha_{x,z}$	Empirical constant for turbulence correction factors
$\beta$	Bulk modulus
$\beta_{x,z}$	Empirical constant for turbulence correction factors
$\delta_{i,j}$	Kronecker delta
$\epsilon$	Eccentricity ratio
$\epsilon_m$	Eddy viscosity
$\gamma$	Ratio of excitation frequency to shaft rotational speed or ratio of specific heats
$\gamma_S$	Gas foil bearing structural loss factor
$\gamma_{pv}$	Generalized isentropic pressure-volume exponent

$\kappa$	Gauss-Seidel relaxation factor
$\kappa_{Te}$	Effective bulk modulus
$\Lambda$	Bearing compressibility number/Bearing speed number
$\lambda$	Laplace damping coefficient
$\mu$	Dynamic viscosity
$\Omega$	Shaft rotational speed
$\omega$	Excitation frequency
$\Phi$	Viscous dissipation
$\psi$	Attitude angle
$\rho$	Density
$\tau$	Shear stress
$\xi$	General flow parameter

**Superscripts**

'	Turbulent fluctuation
-	Non-dimensional

**Subscripts**

0	Nominal or Steady state
<i>cr</i>	Critical
<i>ex</i>	Excitation frequency
<i>ext</i>	External
<i>i</i>	Indicial notation
<i>ig</i>	Ideal gas
<i>j</i>	Indicial notation
<i>lam</i>	Laminar
<i>m</i>	Mean property
<i>min</i>	Minimum
<i>ng</i>	Non-ideal gas
<i>r</i>	Reduced thermodynamic properties or ratio of non-ideal to ideal bearing properties
<i>ref</i>	Reference state
<i>rot</i>	Rotor
<i>turb</i>	Turbulent



# Contents

<b>Acknowledgements</b>	<b>iii</b>
<b>Abstract</b>	<b>v</b>
<b>List of Figures</b>	<b>vii</b>
<b>List of Tables</b>	<b>xi</b>
<b>List of Symbols</b>	<b>xiii</b>
<b>1 Introduction</b>	<b>1</b>
1.1 Context	1
1.2 Gas Foil Bearings	2
1.3 Motivation of the Work	3
1.4 Research Questions and Objectives	4
1.5 Report Outline	5
<b>2 Methodology</b>	<b>7</b>
2.1 Compressible Reynolds Equation	7
2.2 Temperature Equation & Thermal Expansions	11
2.3 Turbulence Effects	14
2.4 Perturbed Reynolds Equation	16
2.5 Foil Modelling in Gas Bearings	18
2.6 Bearing Performance Characteristics	21
2.7 Numerical Solution Method for the Reynolds Equation	24
<b>3 Results for Rigid Gas Bearings</b>	<b>29</b>
3.1 Verification of the Numerical Model	29
3.1.1 Laminar Flow	29
3.1.2 Turbulent Flow	32
3.2 Steady-State Bearing Performance	34
3.2.1 Fundamental Operating Principles	34
3.2.2 Non-dimensional Bulk Modulus	36
3.2.3 Effect of Molecular Interactions	38
3.2.4 Effect of Working Fluid	41
3.2.5 Effect of Bearing Width	42
3.3 Dynamic Bearing Performance	43
3.3.1 Fundamental Operating Principles	44
3.3.2 Non-dimensional Bulk Modulus & Compressibility Number	46
3.4 Effect of Viscosity	49
3.5 Turbulence Effects	50
3.5.1 Effect on Steady-State Characteristics	51
3.5.2 Effect on Dynamic Characteristics	52
3.5.3 Connection with Non-Ideal Thermodynamic Effects	54
3.6 Chapter Conclusion	55
<b>4 Results for Gas Foil Bearings</b>	<b>57</b>
4.1 Verification	57
4.2 Analysis of Gas Foil Bearings	60
4.2.1 Load Capacity	60
4.2.2 Attitude Angle and Stability	61
4.3 Application to the ORCHID turbine	63
4.4 Chapter Conclusion	65

---

<b>5</b>	<b>Conclusion &amp; Recommendations</b>	<b>67</b>
5.1	Conclusion . . . . .	67
5.2	Recommendations . . . . .	68
	<b>Bibliography</b>	<b>69</b>
	<b>Appendices</b>	<b>71</b>
<b>A</b>	<b>Link to the Python Repository</b>	<b>73</b>

# 1

## Introduction

### 1.1. Context

The Paris agreement is considered as a turning point in the approach of tackling global warming. The agreement aims to significantly reduce global greenhouse gas emissions over all industry sectors. The long-term mean global temperature rise should be limited to well below  $2^{\circ}\text{C}$ . Furthermore, European carbon emissions should reach net zero by the second half of the 21st century. The aviation industry currently accounts for approximately 2% to 3% of carbon dioxide emissions globally, and about 4% in Europe. [6] With other emitting sectors taking action to improve sustainability, this proportion of emissions attributable to aviation is expected to grow in the near future if no drastic measures are taken.

In recent years, revolutionary new technologies have been presented to reduce carbon emissions in aviation. Liquid hydrogen has been considered as a promising alternative for jet fuel in commercial airliners. With hydrogen as an energy carrier, the use of fuel cells could be an attractive option to convert stored chemical energy into electrical energy. Fuel cells could power propeller-driven aircraft allowing for efficient transportation on short- to medium-haul airliners. Proton exchange membrane fuel cells (PEMFC) are a promising fuel cell technology for efficient conversion of the chemical energy in hydrogen. However, if the technology is to be applied in aviation, large power densities are required.[7] Supplying pressurized air to the fuel cell stack can increase power density and electrical efficiency. The pressurization of the air to the stack can typically be done using a compact centrifugal compressor operating at high rotational speeds.

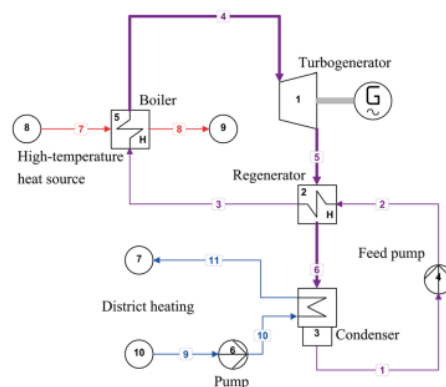


Figure 1.1: Exemplary process flow diagram of an ORC system.[1]

A key aspect in the design of more sustainable aircraft will be to effectively exploit all the available energy streams. Irrespective of the configuration in terms of gas turbine or fuel cell driven propulsion, waste heat recovery has the potential of significantly increasing the net conversion efficiency of propulsion or thermal management systems. The organic Rankine cycle (ORC) turbogenerator could

be an effective technology for the conversion of wasted thermal energy into useful power aboard the aircraft. An exemplary process flow diagram of such an ORC system is shown in Figure 1.1. [1] For aviation, a large power density ORC system is desired in which the size and weight of the various system components are minimized. The performance of an ORC system is largely dependent on the performance of the expander and a radial inflow turbine operating at high rotational speeds is arguably the most attractive option in terms of efficiency, size and weight.

Fuel cells are very sensitive to pollutants. Contamination of the pressurised air stream to the fuel cell can cause damage and loss of performance of the electrodes in the stack. For ORC systems, the properties of the organic fluid and its thermal stability are important characteristics determining the performance of the cycle.[1] Contamination of the working fluid can negatively affect the performance of the system components. Oils trapped in the heat exchangers, for example, can cause deteriorated heat transfer coefficients. The use of conventional rolling element bearings in the turbomachinery components of aforementioned systems requires oil lubrication systems. Such oil lubrication systems add complexity and weight and the oil can contaminate the working fluid, which brings up the demand for oil-free turbomachinery. Furthermore, the high rotational speeds as a result of the small scales of the turbomachinery components as well as the requirements for extended lifetimes makes the use of gas dynamic bearings an attractive option for such systems.

## 1.2. Gas Foil Bearings

Research on hydrodynamic bearings has been pursued for more than half a century. Due to the lack of physical contact between mechanical parts such bearings allow for operation at high rotational speeds and increased operational lifetime. Within hydrodynamic bearings, the rotation of the shaft drags the fluid as a result of viscous shear stresses. The fluid is dragged into a hydrodynamic wedge which generates pressure. A schematic of a typical hydrodynamic journal bearing is shown in Figure 1.2. The hydrodynamic wedge is facilitated by the offset of the shaft centre from the centre of the bearing housing, which is generally referred to as the eccentricity  $e$  or eccentricity ratio  $\epsilon$ . As illustrated in the figure, the generated pressure allows the bearing to carry an external load  $W_{ext}$ .

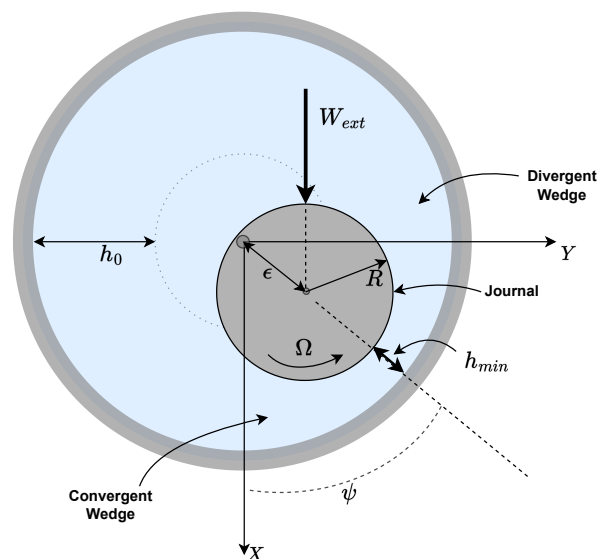


Figure 1.2: Schematic of a typical hydrodynamic journal bearing.

For applications such as the organic Rankine cycle or fuel cell systems, it is desirable to rely on oil-free turbomachinery. Instead of making use of oil, the working fluid of the system could be used as a lubricant. Gasses and vapors typically have a much lower density and viscosity than oil, allowing for reduced power losses within the bearing. However, this also results in relatively low load-carrying capacities. As a result, gas dynamic bearings are suitable only for supporting rotors of compact systems typically operating at very large rotational speeds.

Another result of the lower lubricant viscosity in gas-lubricated bearings compared to oil-lubricated

bearings is the reduced damping of the gas film.[8] Journal bearings suffer from cross-coupled reaction forces to perturbations in the journal position. This can result in an unstable whirling motion typically referred to as sub-synchronous or half-frequency whirl. This instability is characterized by a whirling motion around the shaft equilibrium position with a frequency of about half the shaft rotational speed. Such instabilities can significantly limit the operating range of gas dynamic bearings in particular.

In order to increase the performance of rigid plain gas bearings, the geometry could be altered to include features such as compliant foundations or grooved surfaces. A common compliant surface gas bearing is referred to as the gas foil bearing. A schematic of a first-generation gas foil journal bearing is shown in Figure 1.3.[2] The compliant structure consists of a bump foil or bump strip layer which is welded to the housing at the trailing edge. The top foil is spot welded to the housing at the same point and laid on top of the bump foil loosely, thereby separating the gas film and the ambient pressure gas underneath the top foil. The gas foil journal bearing as depicted in the figure can carry radial loads whereas axial loads on the rotor are supported using gas foil thrust bearings such as the one shown in Figure 1.4b.

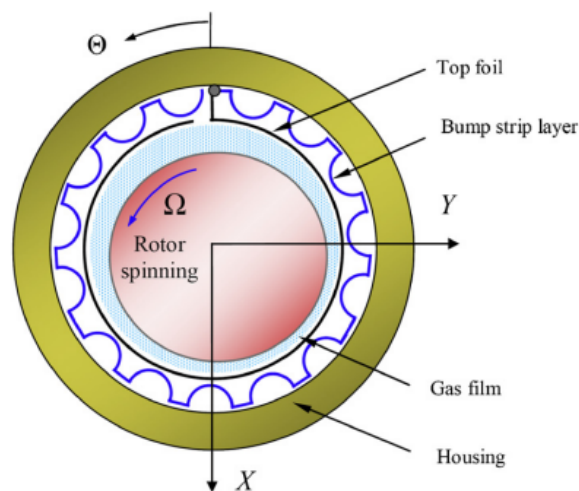


Figure 1.3: Schematic of a first generation gas foil journal bearing.[2]

An example of a widespread application of gas foil bearings is in aircraft environmental control systems (ECS). The air cycle machine (ACM) is a commonly used refrigeration unit of this environmental control system in gas-turbine powered aircraft. The system is used to provide cooled air to the cabin and any possible contamination of the process air should therefore be avoided. A similar argument applies to the application of gas foil bearings in waste-water treatment blowers which is a relatively large market for the technology nowadays. Such blowers are used to create air bubbles to aid the biological processes of aeration and agitation. Other applications include micro-turbines, cryogenic pumps and possibly fuel cell air compressors.

### 1.3. Motivation of the Work

Extensive research on the design and performance of gas foil thrust and journal bearings has been carried out by NASA around the start of the 21st century. One of the goals of the research was to improve familiarity with the foil bearing design and manufacturing processes.[9] Experimental studies have been performed on prototype bearings of which examples are shown in Figure 1.4. Modelling of gas foil bearings was typically done by solving the Reynolds equation under the assumption of ideal gas behaviour. Since most applications at the time involved bearing operation with ambient air at standard sea level conditions, there was no need to investigate the effect of high pressure and non-ideal flows.

In recent years, there has been an increasing interest in the application of gas dynamic bearings for applications such as organic Rankine cycle turbines or compressors for super-critical carbon-dioxide power systems.[10] Such applications are characterized by high-pressure working fluids typically near the vapour saturation line or the thermodynamic critical point. Under these circumstances the compressibility of the fluid becomes significant and the ideal gas law is no longer applicable.

Although there is an increased interest in high-pressure gas lubrication, there is still a lack of generalization of the effects of non-ideal compressible lubrication flows. Guenat investigated the characteristics of bearings operating in proximity to the thermodynamic critical point where increased compressibility of the fluid is observed.[11] In his work, the effect of compressibility on bearing load capacity and stability was analysed mainly for grooved dynamic bearings.

The work presented in this manuscript aims to address this knowledge gap further by first investigating these effects from a conceptual point of view in terms of non-dimensional numbers. In particular, the work focuses on the modelling of gas bearings lubricated with fluids made by complex molecules like those adopted for waste heat recovery at high temperatures in aviation. Furthermore, the work aims to implement numerical models that capture the complex fluid-structure interaction characteristic of gas foil journal bearings as an initial step to verify the feasibility of this particular technology for application with (mini-)organic Rankine cycle turbo-generators.

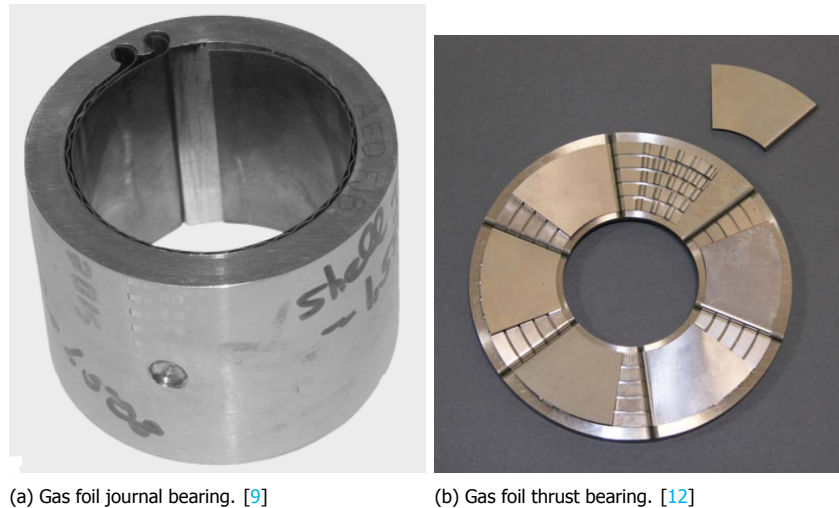


Figure 1.4: Gas foil journal and thrust bearings designed by NASA.

## 1.4. Research Questions and Objectives

The goal of this research is to investigate the performance of gas dynamic bearings lubricated with non-ideal compressible flows at high pressure. The work will focus primarily on modelling gas bearings lubricated with fluids composed of complex molecules suitable for waste heat recovery in aviation. The first step will be to implement numerical models capturing the behaviour of (rigid) plain journal bearings. Afterwards, the models will be extended to include the fluid-structure interaction characteristic of compliant surface bearings. In particular, the goal is to implement a numerical tool that captures the behaviour of gas foil bearings used to support high-speed rotors of (mini)-ORC turbines. As such, this work is intended to aid in verifying the feasibility of this technology for application with the turbine of the Organic Rankine Cycle Hybrid Integrated Device (ORCHID) of the TU Delft. To this end, the following research questions are formulated in this work:

- How do non-ideal thermodynamic effects and effects related to the type of fluid molecule affect the performance of gas dynamic bearings in terms of load-carrying capacity and stability in comparison to bearings lubricated with ideal gasses?
- Can gas foil journal bearings lubricated with siloxane MM generate sufficient load-carrying capacity to support the rotor of the Organic Rankine Cycle Hybrid Integrated Device (ORCHID) turbine at design conditions?

In order to answer the research questions, a number of research objectives are formulated. These objectives are listed as follows:

- Implement the relevant numerical models into a computational tool that allows for the prediction of gas film properties such as density and pressure for bearings lubricated with arbitrary working fluids at different thermodynamic conditions.

- Predict steady-state and dynamic bearing performance characteristics including load-carrying capacity and rotor-dynamic critical mass using the gas film properties calculated by the developed tool.
- Verify the computational tool and the computed bearing characteristics by using openly available data in scientific literature.
- Use the numerical predictions to assess the influence of non-ideal thermodynamic effects on bearing performance characteristics including load capacity and rotor-dynamic critical mass for laminar and turbulent lubrication flows.
- Assess the influence of structural compliance in gas dynamic bearings lubricated with dense vapors by comparing numerical results for plain journal bearings and gas foil bearings.
- Use the computational tool to calculate the load-carrying capacity of a gas foil bearing lubricated with siloxane MM at suitable dimensions and operating conditions for application with the ORCHID turbine.

## 1.5. Report Outline

The report is structured in the following way:

- [Chapter 2](#) presents the methodology used in this research. The compressible Reynolds equation governing the gas film properties is derived for three-dimensional unsteady lubrication flows. The effects of thermal expansions and the limitations of the compressible Reynolds equation are discussed. Furthermore, the gas film models are extended to account for turbulence effects which become increasingly important for supercritical or dense fluids. The frequency perturbation method is introduced as a means of obtaining the steady-state density field and the perturbed density field used to compute bearing impedances. Models used to compute the structural deflections in gas foil bearings are presented. Finally, the numerical methods used to solve the differential equations are discussed. The chapter and the developed computational tool are summarized by means of two flow diagrams presenting the steady and dynamic solution procedures.
- [Chapter 3](#) discusses the influence of non-ideal compressible flows on plain journal bearings. First, the results computed with the developed tools are verified using data from scientific literature. The non-ideal steady-state load capacity is shown to be influenced primarily by the non-dimensional bulk modulus. Next, the onset of a self-sustained instability in gas bearings is discussed and the analysis of the non-dimensional bulk modulus is extended to the dynamic bearing characteristics. The influence of variations in dynamic viscosity is briefly addressed. The chapter is concluded by assessing the effects of turbulence in non-ideal gas lubrication.
- In [chapter 4](#) the step towards gas foil bearings is made. The models applicable to gas foil bearings are verified using data from literature. The data correspond to lubrication with laminar flows of sea-level pressure air. Next, the differences between rigid surface and compliant surface bearings are analysed by comparing numerical results for plain journal bearings and gas foil bearings. Finally, the load capacity is plotted as a function of journal eccentricity, minimum film thickness and attitude angle for a gas foil bearing suitable for operation with the ORCHID turbine. The bearing is shown to operate at a Reynolds number within the limits of the turbulence model and the assumptions made in the derivation of the compressible Reynolds equation are shown to hold at design conditions.



# 2

## Methodology

The models and mathematical equations used to analyse the performance of gas dynamic bearings will be presented in this chapter. The motion of the gas film is governed by the Reynolds equation. The Reynolds equation was first derived by Osborne Reynolds in 1886 for incompressible flows [13] and it has since been an instrumental mathematical tool in the research on lubrication. Since its first derivation, the Reynolds equation has been extended to include compressible, three-dimensional, unsteady and turbulent effects. In this chapter, such a derivation of the compressible Reynolds equation is presented.

To capture the deflections of compliant surfaces in gas foil bearings a simple structural model will be presented which is coupled to the Reynolds equation. Furthermore, some relevant bearing characteristics including load-carrying capacity and a rotor-dynamic critical mass will be defined. The chapter is concluded with a description of the numerical solver used to iteratively solve the partial differential equations.

### 2.1. Compressible Reynolds Equation

Since its first derivation for incompressible flows in 1886 the Reynolds equation has been used extensively in scientific literature on lubrication theory. Often the equation was coupled to an ideal gas equation of state. The recent shift towards high-pressure lubrication, however, requires the inclusion of non-ideal compressible flow effects in the Reynolds equation. Conboy, for example, simulated the non-ideal gas lubrication in gas foil thrust bearings operating with supercritical carbon dioxide. [14] Kim presented a three-dimensional thermo-hydrodynamic design tool for radial foil bearings using the Reynolds equation including turbulent and non-ideal thermodynamic effects. [15]

The compressible Reynolds equation is derived from the Navier-Stokes equations and governs the density and pressure field within the thin fluid film. The method of deriving the equation as presented in this section is based on the work of Chien, Cramer and Untaroiu [16], extended to include three-dimensional and unsteady effects.

In Figure 2.1 a schematic figure is shown of a plain journal bearing indicating the nomenclature to be used in the equations. The nominal bearing clearance  $h_0$  is defined as the film thickness for a bearing with zero eccentricity, i.e. when the shaft and the bearing housing are concentric. This eccentricity, defined as the offset between the shaft centre and the centre of the bearing housing, is denoted with the symbol  $e$ . Often, however, the eccentricity ratio  $\epsilon$  is stated which is defined as the eccentricity normalized with the nominal bearing clearance. The attitude angle  $\psi$  is defined as the angle between the inertial  $X$ -axis and the eccentricity as shown in the figure. The circumferential coordinate  $\bar{x}$  measures the circumferential distance from the inertial  $X$ -axis in counterclockwise direction normalized by the bearing radius  $R$ . The axial  $\bar{z}$  component extends into or out of the page in the direction of the bearing width and is also normalized using the bearing radius. The non-dimensional film thickness  $\bar{h}$  is, in general, a function of the circumferential coordinate  $\bar{x}$  and can be computed using the eccentricity ratio  $\epsilon$  and attitude angle  $\psi$  for a plain journal bearing as:

$$\bar{h}(\bar{x}) = 1 - \epsilon \cos(\bar{x} - \psi) \quad (2.1)$$

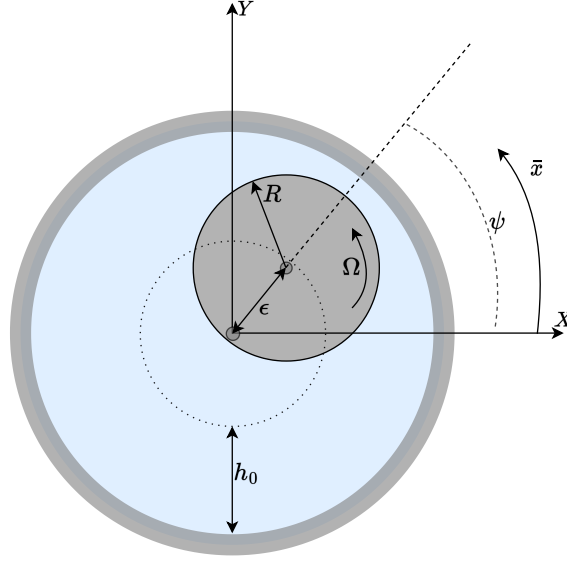


Figure 2.1: Schematic figure showing a plain journal bearing.

Where the film thickness  $h$  is normalized using the nominal film thickness. The flow properties such as the density and pressure distribution are directly affected by the film thickness distribution and this relation is captured by the Reynolds equation. Within the derivation in this section, the following assumptions are made:

- The film thickness is negligible compared to other length scales of the bearing.
- The lubricating film is laminar.
- Inertia effects are negligible relative to viscous shear stresses.
- The fluid is characterized by a Newtonian stress-strain relationship.
- Thermodynamic properties such as density and pressure are constant over the film thickness.

The compressible Navier-Stokes equations without body forces [17] form the starting point of the derivation and are presented using tensor notation in Equation 2.2:

$$\rho \frac{\partial u_i}{\partial t} + \rho u_j \frac{\partial u_i}{\partial x_j} = -\frac{\partial p}{\partial x_i} + \frac{\partial}{\partial x_j} \left( 2\mu e_{ij} - \frac{2}{3}\mu \frac{\partial u_k}{\partial x_k} \delta_{ij} \right) \quad (2.2)$$

In which the strain-rate tensor  $e_{ij}$  can be written as:

$$e_{ij} = \frac{1}{2} \left( \frac{\partial u_i}{\partial x_j} + \frac{\partial u_j}{\partial x_i} \right) \quad (2.3)$$

In order to derive the Reynolds equation and apply the corresponding assumptions, it is useful to normalize the Navier-Stokes equations using the definition of the non-dimensional parameters as presented in Equation 2.4:

$$\begin{aligned} \bar{u} &= \frac{u}{\Omega R} & \bar{v} &= \frac{vR}{\Omega R h_0} & \bar{w} &= \frac{w}{\Omega R} & \bar{x} &= \frac{x}{R} & \bar{y} &= \frac{y}{h_0} & \bar{z} &= \frac{z}{R} \\ \bar{t} &= t\Omega & \bar{p} &= (p - p_{ref}) \frac{h_0^2}{\mu_{ref} \Omega R^2} & \bar{\rho} &= \frac{\rho}{\rho_{ref}} & \bar{\mu} &= \frac{\mu}{\mu_{ref}} \end{aligned} \quad (2.4)$$

Using the normalized variables and Equation 2.2, the  $x$ -  $y$ - and  $z$ -components of the Navier-Stokes equation are written in non-dimensional form as:

$$Re \frac{h_0}{R} \frac{\partial \bar{u}}{\partial \bar{t}} + Re \frac{h_0}{R} (\vec{v} \cdot \vec{\nabla}) \bar{u} + \frac{\partial \bar{p}}{\partial \bar{x}} = \frac{h_0^2}{R^2} \frac{\partial}{\partial \bar{x}} \left[ 2\bar{\mu} \frac{\partial \bar{u}}{\partial \bar{x}} - \frac{2}{3} \bar{\mu} \left( \frac{\partial \bar{u}}{\partial \bar{x}} + \frac{\partial \bar{v}}{\partial \bar{y}} + \frac{\partial \bar{w}}{\partial \bar{z}} \right) \right] + \frac{\partial}{\partial \bar{y}} \left[ \bar{\mu} \left( \frac{\partial \bar{u}}{\partial \bar{y}} + \frac{h_0^2}{R^2} \frac{\partial \bar{v}}{\partial \bar{x}} \right) \right] + \frac{h_0^2}{R^2} \frac{\partial}{\partial \bar{z}} \left[ \bar{\mu} \left( \frac{\partial \bar{u}}{\partial \bar{z}} + \frac{\partial \bar{w}}{\partial \bar{x}} \right) \right] \quad (2.5)$$

$$Re \frac{h_0^3}{R^3} \frac{\partial \bar{v}}{\partial \bar{t}} + Re \frac{h_0^3}{R^3} (\vec{v} \cdot \vec{\nabla}) \bar{v} + \frac{\partial \bar{p}}{\partial \bar{y}} = \frac{h_0^2}{R^2} \frac{\partial}{\partial \bar{x}} \left[ \bar{\mu} \left( \frac{\partial \bar{u}}{\partial \bar{y}} + \frac{h_0^2}{R^2} \frac{\partial \bar{v}}{\partial \bar{x}} \right) \right] + \frac{h_0^2}{R^2} \frac{\partial}{\partial \bar{y}} \left[ 2\bar{\mu} \frac{\partial \bar{v}}{\partial \bar{y}} - \frac{2}{3} \bar{\mu} \left( \frac{\partial \bar{u}}{\partial \bar{x}} + \frac{\partial \bar{v}}{\partial \bar{y}} + \frac{\partial \bar{w}}{\partial \bar{z}} \right) \right] + \frac{h_0^2}{R^2} \frac{\partial}{\partial \bar{z}} \left[ \bar{\mu} \left( \frac{h_0^2}{R^2} \frac{\partial \bar{v}}{\partial \bar{z}} + \frac{\partial \bar{w}}{\partial \bar{y}} \right) \right] \quad (2.6)$$

$$Re \frac{h_0}{R} \frac{\partial \bar{w}}{\partial \bar{t}} + Re \frac{h_0}{R} (\vec{v} \cdot \vec{\nabla}) \bar{w} + \frac{\partial \bar{p}}{\partial \bar{z}} = \frac{h_0^2}{R^2} \frac{\partial}{\partial \bar{x}} \left[ \bar{\mu} \left( \frac{\partial \bar{u}}{\partial \bar{z}} + \frac{\partial \bar{w}}{\partial \bar{x}} \right) \right] + \frac{\partial}{\partial \bar{y}} \left[ \bar{\mu} \left( \frac{h_0^2}{R^2} \frac{\partial \bar{v}}{\partial \bar{z}} + \frac{\partial \bar{w}}{\partial \bar{y}} \right) \right] + \frac{h_0^2}{R^2} \frac{\partial}{\partial \bar{z}} \left[ 2\bar{\mu} \frac{\partial \bar{w}}{\partial \bar{z}} - \frac{2}{3} \bar{\mu} \left( \frac{\partial \bar{u}}{\partial \bar{x}} + \frac{\partial \bar{v}}{\partial \bar{y}} + \frac{\partial \bar{w}}{\partial \bar{z}} \right) \right] \quad (2.7)$$

In order to simplify the equations, the assumption is made that the film thickness is much smaller as compared to a characteristic length scale in either of the two orthogonal directions. That is, the film thickness  $h$  is negligible compared to the bearing radius  $R$  or bearing axial width  $L$ :

$$\frac{h_0^2}{R^2} \ll 1 \quad (2.8)$$

Furthermore, the assumption is made that the inertia of the flow is negligible compared to the viscous forces of the fluid:

$$Re \frac{h_0}{R} \ll 1 \quad (2.9)$$

In which the Reynolds number is defined based on the film thickness  $h$  and the peripheral speed of the rotor  $U = \Omega R$ . The density and dynamic viscosity are evaluated at a reference thermodynamic state which is typically the state of the ambient fluid in the compartment in which the bearing is located:

$$Re = \frac{\rho_{ref} \Omega R h_0}{\mu_{ref}} \quad (2.10)$$

Under the aforementioned assumptions, the non-dimensional Navier-Stokes equations simplify to the following relations:

$$\frac{\partial \bar{p}}{\partial \bar{x}} = \frac{\partial}{\partial \bar{y}} \left( \bar{\mu} \frac{\partial \bar{u}}{\partial \bar{y}} \right) \quad (2.11)$$

$$\frac{\partial \bar{p}}{\partial \bar{y}} = 0 \quad (2.12)$$

$$\frac{\partial \bar{p}}{\partial \bar{z}} = \frac{\partial}{\partial \bar{y}} \left( \bar{\mu} \frac{\partial \bar{w}}{\partial \bar{y}} \right) \quad (2.13)$$

Equation 2.12 states that the pressure can be considered constant over the film thickness. Equation 2.11 and Equation 2.13 can be integrated twice to obtain expressions for the circumferential and axial velocity components, respectively. In order to do so the following no-slip boundary conditions are applied:

$$\begin{aligned} \bar{u}(y=0) &= 0 & \bar{w}(y=0) &= 0 \\ \bar{u}(y=h) &= 1 & \bar{w}(y=h) &= 0 \end{aligned} \quad (2.14)$$

Note that  $y = 0$  refers to the surfaces of the bearing housing and  $y = h$  indicates the surface of the rotating shaft. The boundary conditions lead to the following expressions for the non-dimensional velocity profiles in circumferential and axial directions:

$$\bar{u} = \frac{1}{2\bar{\mu}} \frac{\partial \bar{p}}{\partial \bar{x}} (\bar{y}^2 - \bar{h}\bar{y}) + \frac{1}{\bar{h}} \bar{y} \quad (2.15)$$

$$\bar{w} = \frac{1}{2\bar{\mu}} \frac{\partial \bar{p}}{\partial \bar{z}} (\bar{y}^2 - \bar{h}\bar{y}) \quad (2.16)$$

The terms proportional to the pressure gradients in Equation 2.15 and Equation 2.16 are referred to as the Poiseuille flow terms whereas the term proportional to the peripheral speed of the rotor in Equation 2.15 is referred to as the Couette flow term.

In order to connect the velocity profile to the density field, the conservation of mass equation is integrated over the film thickness:

$$\int_0^{\bar{h}} \left( \frac{\partial \bar{\rho}}{\partial \bar{t}} + \vec{\nabla} \cdot (\bar{\rho} \vec{v}) \right) d\bar{y} = 0 \quad (2.17)$$

By substituting Equation 2.15 and Equation 2.16 and applying Leibnitz's integration rule<sup>1</sup> the following expression is obtained.

$$\int_0^{\bar{h}} \frac{\partial \bar{\rho}}{\partial \bar{t}} d\bar{y} + \frac{\partial}{\partial \bar{x}} \left( \bar{\rho} \int_0^{\bar{h}} \left[ \frac{1}{2\bar{\mu}} \frac{\partial \bar{p}}{\partial \bar{x}} (\bar{y}^2 - \bar{h}\bar{y}) + \frac{1}{\bar{h}} \bar{y} \right] d\bar{y} \right) - \bar{\rho} \frac{\partial \bar{h}}{\partial \bar{x}} + \frac{\partial}{\partial \bar{z}} \left( \bar{\rho} \int_0^{\bar{h}} \left[ \frac{1}{2\bar{\mu}} \frac{\partial \bar{p}}{\partial \bar{z}} (\bar{y}^2 - \bar{h}\bar{y}) \right] d\bar{y} \right) = 0 \quad (2.19)$$

Performing the integration and rearranging leads to the following form of the non-dimensional Reynolds equation:

$$\frac{\partial}{\partial \bar{x}} \left( \frac{\bar{\rho} \bar{h}^3}{12\bar{\mu}} \frac{\partial \bar{p}}{\partial \bar{x}} \right) + \frac{\partial}{\partial \bar{z}} \left( \frac{\bar{\rho} \bar{h}^3}{12\bar{\mu}} \frac{\partial \bar{p}}{\partial \bar{z}} \right) = \frac{1}{2} \frac{\partial (\bar{\rho} \bar{h})}{\partial \bar{x}} + \frac{\partial \bar{\rho} \bar{h}}{\partial \bar{t}} \quad (2.20)$$

For a compressible flow, the above equation can be rewritten as a partial differential equation for the density field which leads to the following compressible Reynolds equation, that is the model considered in this work:

$$\frac{\partial}{\partial \bar{x}} \left( \frac{\bar{\beta} \bar{h}^3}{\bar{\mu}} \frac{\partial \bar{\rho}}{\partial \bar{x}} \right) + \frac{\partial}{\partial \bar{z}} \left( \frac{\bar{\beta} \bar{h}^3}{\bar{\mu}} \frac{\partial \bar{\rho}}{\partial \bar{z}} \right) = \Lambda \frac{\partial (\bar{\rho} \bar{h})}{\partial \bar{x}} + 2\Lambda \frac{\partial \bar{\rho} \bar{h}}{\partial \bar{t}} \quad (2.21)$$

In which  $\bar{\beta}$  is the non-dimensional bulk modulus written as:

$$\bar{\beta} = \frac{\rho}{p_{ref}} \frac{\partial p}{\partial \rho} \Big|_T \quad (2.22)$$

The bulk modulus relates to the compressibility of the fluid as it is a measure of the resistance of a substance to volume changes. The effect of the bulk modulus on bearing performance will be discussed in detail in subsequent chapters. It should be noted that the compressible Reynolds equation in the form of Equation 2.21 is only valid if the effects of thermal expansion can be neglected. The potential relevance of thermal expansion in thin films will be discussed in the next section. The compressibility number or bearing speed number in Equation 2.21 is defined as:

$$\Lambda = \frac{6\mu_{ref}\Omega R^2}{p_{ref}h_0^2} \quad (2.23)$$

<sup>1</sup>Leibnitz's integration rule can be written for example for the partial derivative in circumferential direction as:

$$\int_0^{\bar{h}} \frac{\partial}{\partial \bar{x}} f(\bar{x}, \bar{y}, \bar{z}) d\bar{y} = \frac{\partial}{\partial \bar{x}} \int_0^{\bar{h}} f(\bar{x}, \bar{y}, \bar{z}) d\bar{y} - f(\bar{x}, \bar{h}, \bar{z}) \frac{\partial \bar{h}}{\partial \bar{x}} \quad (2.18)$$

As mentioned, the reference thermodynamic state used in this definition is typically the state of the fluid in the bearing compartment. The compressibility number is an indication of the relative balance between Poiseuille flow and Couette flow in the Reynolds equation. Large compressibility numbers can be the result of high rotor speeds and indicate that the driving Couette flow is increasingly dominant. This can typically lead to larger load capacities as elaborated in subsequent chapters. The compressibility number is sometimes also referred to as the bearing number or bearing speed number.

This section is concluded by indicating a limitation of the compressible Reynolds equation beyond the presented assumptions. Equation 2.12 shows that the pressure can be considered constant across the film thickness as long as the film thickness is small compared to the radius of the bearing. In the integration of the conservation of mass equation (Equation 2.19) it was implicitly assumed that the variation of the density over the film thickness is therefore negligible as well. In order to verify this assumption, the variation of the non-dimensional density can be written as a function of non-dimensional pressure and temperature variations through an equation of state model as:[16]

$$\frac{d\bar{\rho}}{\rho} = \frac{\gamma}{\bar{\rho}\bar{a}^2} \frac{M_{ref}^2}{Re \frac{h_0}{R}} d\bar{p} - \alpha \Delta T d\bar{T} \quad (2.24)$$

Equation 2.24 shows that the density variations might be significantly larger than the pressure variations when the ratio of specific heats ( $\gamma$ ) becomes singular. If this is the case, the density cannot be considered constant over the film thickness and the integration of conservation of mass as done in Equation 2.19 is no longer correct. This indicates the impossibility of using the Reynolds equation for modeling the motion of the fluid film close to the critical point. The singularity of  $\gamma$  is the result of a singularity in  $c_p$  near the critical point as shown in Figure 2.2 for siloxane MM.

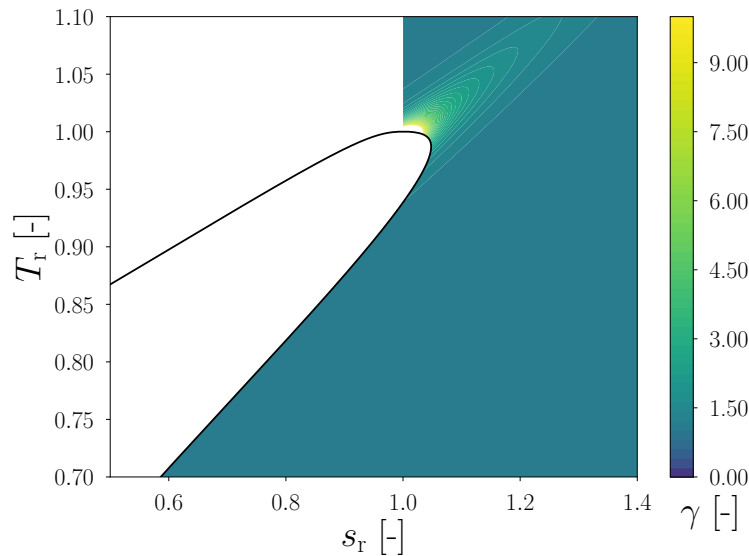


Figure 2.2: Contour plot of the ratio of specif heats ( $\gamma$ ) for siloxane MM created using NiceProp.[3]

## 2.2. Temperature Equation & Thermal Expansions

In the previous section, the compressible Reynolds equation was presented. This equation constitutes a second-order non-linear partial differential equation through the presence of the bulk modulus and dynamic viscosity. The bulk modulus and dynamic viscosity are thermodynamic variables and are therefore a function of both density and temperature for example ( $\beta(\rho, T)$  and  $\mu(\rho, T)$ ). For compressible flows, the temperature is, in general, not constant throughout the flow field. Chien, Cramer and Untaroiu presented the non-dimensional energy equation for steady two-dimensional flows.[16] In this section, this procedure is followed and the unsteady three-dimensional energy equation is derived.

Finally, the assumption of negligible thermal expansion in thin film flows as applied in this work is discussed.

Conservation of energy can be written in differential form in terms of enthalpy for a flow without internal heat sources as: [17]

$$\rho \frac{Dh}{Dt} = \frac{Dp}{Dt} - \frac{\partial q_i}{\partial x_i} + \tau_{ij} \frac{\partial u_i}{\partial x_j} \quad (2.25)$$

In which thermal conduction can be modelled using Fourier's law:

$$q_i = -k \frac{\partial T}{\partial x_i} \quad (2.26)$$

Enthalpy changes can be related to temperature and pressure changes through an equation of state model:

$$dh = \left( \frac{\partial h}{\partial T} \right)_p dT + \left( \frac{\partial h}{\partial p} \right)_T dp = c_p dT + \left( \frac{\partial h}{\partial p} \right)_T dp \quad (2.27)$$

Furthermore, by resorting to Gibb's equation and utilizing Maxwell's relations the following identity can be written for the partial derivative of enthalpy with respect to pressure at constant temperature:

$$\rho \left( \frac{\partial h}{\partial p} \right)_T = \rho T \left( \frac{\partial s}{\partial p} \right)_T + 1 = \frac{T}{\rho} \left( \frac{\partial \rho}{\partial T} \right)_p + 1 = 1 - \alpha T \quad (2.28)$$

In which  $\alpha = -\frac{1}{\rho} \left( \frac{\partial \rho}{\partial T} \right)_p$  is defined as the isobaric expansion coefficient. Using this identity and Equation 2.27, conservation of energy Equation 2.25 can be written by making the temperature variations explicit as follows:

$$\rho c_p \frac{DT}{Dt} = \alpha T \frac{Dp}{Dt} + \frac{\partial}{\partial x_i} \left( k \frac{\partial T}{\partial x_i} \right) + \tau_{ij} \frac{\partial u_i}{\partial x_j} \quad (2.29)$$

Following the procedure proposed by Chien, Cramer and Untaroiu, the temperature equation Equation 2.29 can be normalized using the definitions given in Equation 2.4 along with the following definitions:

$$\begin{aligned} \bar{T} &= \frac{T - T_{ref}}{\Delta T} & \bar{c}_p &= \frac{c_p}{c_{pref}} & \bar{k} &= \frac{k}{k_{ref}} \\ Pr &= \frac{\mu_{ref} c_{pref}}{k_{ref}} & Ec &= \frac{\Omega^2 R^2}{c_{pref} \Delta T} \end{aligned} \quad (2.30)$$

In which  $\Delta T$  is some representative temperature difference occurring in the flow,  $Ec$  is the Eckert number and  $Pr$  is the Prandtl number. Using the above-mentioned normalization the temperature equation is written in non-dimensional form as:

$$\begin{aligned} Re \frac{h_0}{R} Pr \bar{\rho} \bar{c}_p \frac{\partial \bar{T}}{\partial \bar{t}} + Re \frac{h_0}{R} Pr \bar{\rho} \bar{c}_p (\vec{\bar{v}} \cdot \vec{\bar{\nabla}}) \bar{T} &= \frac{\partial}{\partial \bar{y}} \left( \bar{k} \frac{\partial \bar{T}}{\partial \bar{y}} \right) + \frac{h_0^2}{R^2} \left[ \frac{\partial}{\partial \bar{x}} \left( \bar{k} \frac{\partial \bar{T}}{\partial \bar{x}} \right) + \frac{\partial}{\partial \bar{z}} \left( \bar{k} \frac{\partial \bar{T}}{\partial \bar{z}} \right) \right] + \\ &Pr Ec \left[ \bar{\Phi} + \alpha T \frac{\partial \bar{p}}{\partial \bar{t}} + \alpha T (\vec{\bar{v}} \cdot \vec{\bar{\nabla}}) \bar{p} \right] \end{aligned} \quad (2.31)$$

The normalized viscous dissipation in the above equation is defined as:

$$\bar{\Phi} = \frac{h_0^2}{\mu_{ref} \Omega^2 R^2} \tau_{ij} \frac{\partial u_i}{\partial x_j} \approx \bar{\tau}_{xy} \frac{\partial \bar{u}}{\partial \bar{y}} + \bar{\tau}_{zy} \frac{\partial \bar{w}}{\partial \bar{y}} \quad (2.32)$$

Applying the assumption that inertia effects are negligible compared to viscous shear stresses, convection of energy becomes negligible. For thin lubrication films as considered in this research, Equation 2.31 states a balance between work done by pressure forces, viscous dissipation and thermal

conduction along the film thickness. In the vast amount of scientific literature on the modelling of gas dynamic bearings, the assumption is made that the flow within the bearing is iso-thermal. This assumption can typically be justified on the basis that the aspect ratio of the gas film is very large.[11] In other words, the heat transfer area over which conduction in film thickness direction occurs is large relative to the bulk flow. This allows the temperature differences as a result of viscous dissipation to be smoothed out by thermal conduction as shown by the temperature equation Equation 2.31. Most of the scientific literature, however, deals with ideal gas lubrication and for compressible flows thermal expansions might play a significant role. These thermal expansions relate to changes in the thin film density distribution as a result of temperature variations. To analyse the relevance of thermal expansion in the thin film flows of interest, the variations in non-dimensional density can be written as a function of pressure and temperature changes as: [16]

$$\frac{d\bar{\rho}}{\rho} = \frac{\gamma}{\bar{\rho}\bar{a}^2} \frac{M_{ref}^2}{Re \frac{h_0}{R}} d\bar{p} - \alpha\Delta T d\bar{T} \quad (2.33)$$

Equation 2.33 indicates that the effect of thermal expansion is characterized by the product  $\alpha\Delta T$ . If the characteristic temperature difference of the flow is determined by the flow dynamics, a typical scaling can be determined by considering the product of the Eckert and Prandtl number, referred to as the Brinkman number, to be equal to one ( $EcPr = Br = 1$ ). A Brinkman number of one is characteristic for flows in which there is a balance between thermal conduction and heat produced by viscous dissipation. Using the definition of the Eckert number and assuming  $Br = 1$ , the thermal expansion can then be expressed as:

$$\alpha\Delta T = \alpha \frac{\Omega^2 R^2}{c_{pref}} Pr = \frac{\alpha a_{ref}^2}{c_{pref}} M_{ref}^2 Pr = \mathcal{O}(G_{ref} M_{ref}^2 Pr) \quad (2.34)$$

In which  $G = \alpha a^2 c_p^{-1}$  is the Grüneisen parameter and  $a$  is the speed of sound. If the flow is to be assumed iso-thermal, the effects of thermal expansion should be negligible. Equation 2.34 as derived by Chien, Cramer and Untaroiu presents a useful guideline for verifying this assumption.[16] For negligible thermal expansion the inequality  $\mathcal{O}(G_{ref} M_{ref}^2 Pr) \ll 1$  should hold true. This limit depends on the thermodynamic reference state in which the bearing is operating as well as the peripheral speed of the rotor. In the computational tool developed in this work, this parameter is plotted on the  $T - s$  plane for a particular bearing by utilizing NiceProp.[3] An example of a bearing operating at  $\Lambda = 0.1$  using siloxane MM as a lubricant is shown in Figure 2.3. The figure shows that the assumption breaks down near the critical point where the compressibility effects and the Prandtl number increase.

In this work, the numerical investigations are limited to the analysis of iso-thermal lubrication flows. The effects of thermal expansion are neglected. It can be shown that in the domain of interest, the effect of temperature variations on bulk modulus and dynamic viscosity is limited as well.[16] The bulk modulus and viscosity will be taken to depend on the local density within the thin film and the reference temperature ( $\beta(\rho, T_{ref})$  and  $\mu(\rho, T_{ref})$ ).

To summarize the mathematical derivations up to this point, Table 2.1 presents the relevant form of the Reynolds equation for the different flow physics involved in the analysis. The table indicates that Equation 2.21 is more restrictive than Equation 2.20 as it cannot be used to model incompressible thin film flows and it cannot be coupled with an energy equation in order to include thermal expansions. These effects, however, will not be considered in this work. Equation 2.21 is used in this research as it allows for straightforward implementation. Furthermore, this form is useful in analysing how the (non-ideal) thermodynamic effects enter the flow models through the Reynolds equation.

Modelled flow physics	Form of Reynolds equation	Notes
Incompressible	Equation 2.20	Density is kept constant in the analysis.
Compressible with thermal effects	Equation 2.20	Requires coupling with the energy equation for the temperature distribution.
Compressible without thermal effects	Equation 2.20 & Equation 2.21	Equation 2.21 allows easier implementation and generalization of physical concepts.

Table 2.1: Summary of the different flow physics captured by the different forms of the Reynolds equation.

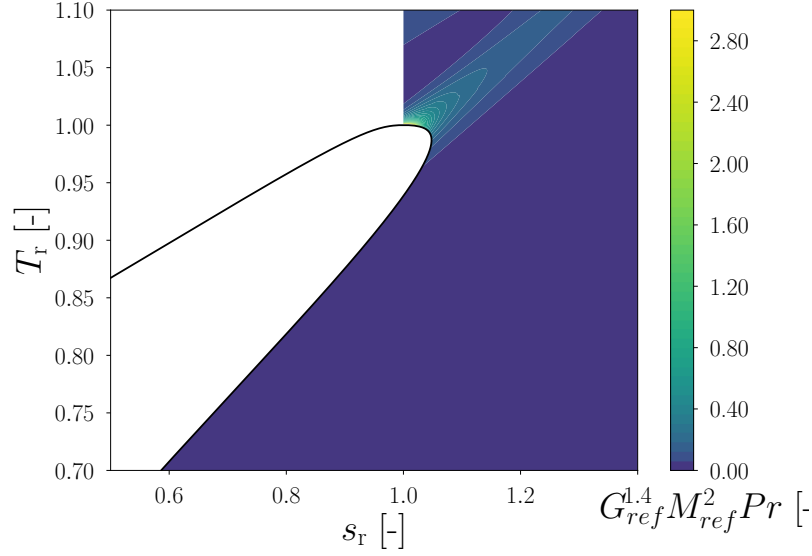


Figure 2.3: Example of a plot showing the relevance of thermal expansions on the density field for a particular bearing lubricated with siloxane MM at  $\Lambda = 0.1$ .

### 2.3. Turbulence Effects

One of the main assumptions within the derivation of the Reynolds equation is that fluid inertia is negligible relative to the viscous stresses. This allows for a balance between pressure and viscous forces. Due to the small film thickness characteristic for thin film flows, the Reynolds number is often sufficiently small to justify this assumption. For high-pressure gasses, however, the Reynolds number can get increasingly large. Bruckner performed experimental studies using high-pressure lubricants in gas foil bearings and showed increased power losses as a result of turbulence effects. [18] His work indicates the relevance of fluid inertia for high-pressure lubricants as this can lead to the onset of turbulence in thin film flows.

There exists a variety of different approaches within the scientific literature to model the effects of turbulence in thin films. Among the first turbulence models derived to account for inertia effects within the Reynolds equation is the work of Constantinescu and it dates back to the previous century.[19] By using the Prandtl mixing length hypothesis, approximate relations for the turbulent velocity profiles within the fluid film are derived. These expressions are used to propose semi-empirical turbulence correction factors applied to the Reynolds equation. In this work, the approach proposed by Constantinescu is followed. The approach is presented in detail in literature.[20] In this section, a summary is given on the background of these correction factors.

A common approach in the analysis of turbulent flows is to use a Reynolds decomposition where the instantaneous quantities are decomposed into the time-averaged component and the fluctuations. For the pressure and circumferential velocity for example:

$$p = \bar{p} + p' \quad u = \bar{u} + u' \quad (2.35)$$

This decomposition can subsequently be substituted into the Navier-Stokes equations (Equation 2.2). By averaging the resulting equations, the so called Reynolds averaged Navier-Stokes (RANS) equations are obtained. The assumptions as discussed in section 2.1 can again be applied to the RANS equations leading to the following momentum conservation equations in circumferential and axial directions for turbulent fluid films:

$$\frac{\partial p}{\partial x} = \frac{\partial}{\partial y} \left( \mu \frac{\partial u}{\partial y} - \overline{\rho u' v'} \right) \quad (2.36)$$

$$\frac{\partial p}{\partial z} = \frac{\partial}{\partial y} \left( \mu \frac{\partial w}{\partial y} - \rho \overline{v'w'} \right) \quad (2.37)$$

The  $\overline{\rho u'u'}$ ,  $\overline{\rho u'v'}$  and  $\overline{\rho u'w'}$  components of the Reynolds stress tensor have dropped out as a result of the thin film assumption similar to the derivation of the laminar Reynolds equation in [section 2.1](#). Note that in the above equations the components  $p$ ,  $u$ ,  $v$  and  $w$  indicate dimensional mean values. The over-bar notation has been dropped on these parameters since these variables will always represent mean values. From now on, if these parameters are indicated with an over-bar this indicates normalization as presented in [Equation 2.4](#).

In order to close the system of equations, the Reynolds stress tensor needs to be modelled. A common approach is to use an Eddy viscosity model, where the Reynolds stress tensor is modelled as being proportional to the strain-rate tensor:

$$-\rho \overline{u'_i u'_j} = \epsilon_m \left( \frac{\partial u_i}{\partial x_j} + \frac{\partial u_j}{\partial x_i} \right) \quad (2.38)$$

In Constantinescu's approach, Prandtl's mixing length hypothesis is used in order to model the Eddy viscosity  $\epsilon_m$ . This allows the  $x$ -component of the momentum equation for example to be written as:

$$\frac{\partial p}{\partial x} = \frac{\partial}{\partial y} \left( \mu \frac{\partial u}{\partial y} + \rho l^2 \left| \frac{\partial u}{\partial y} \right| \frac{\partial u}{\partial y} \right) \quad (2.39)$$

In order to determine the mixing length  $l$  in the above equation, the nearest wall is considered: [\[20\]](#)

$$\begin{aligned} l &= ky & 0 \leq y \leq \frac{h}{2} \\ l &= ky' & 0 \leq y' \leq \frac{h}{2} \end{aligned} \quad (2.40)$$

The definition of  $y$  and  $y'$  is shown in [Figure 2.4](#). The film thickness is divided into the top and bottom half with the nearest wall being either the rotor or the housing of the bearing.

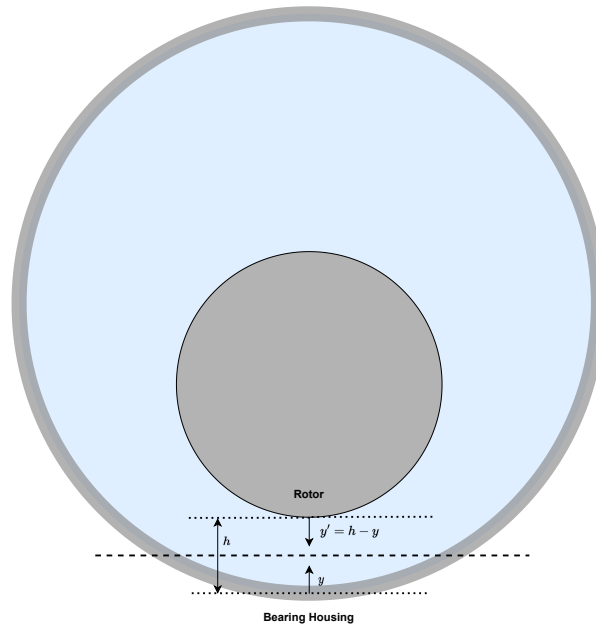


Figure 2.4: Distance from the nearest wall for determining the Prandtl mixing length.

In principle, [Equation 2.39](#) can be integrated at this point. However, Constantinescu followed Prandtl's approach and subdivided both the top and bottom half of the film thickness in a viscous sub-layer and a log-law region resulting in a total of four distinct regions throughout the film thickness.

In the viscous sub-layer it is assumed that the turbulent fluctuations are damped out by the presence of the wall and the viscous stresses are dominant. In the log-law region the molecular viscosity is assumed negligible compared to the components of the Reynolds stress tensor. By applying these assumptions in the analysis of different flow situations (corresponding to positive or negative pressure or velocity gradients for example), the velocity profile throughout the entire thin film is approximated. These velocity profiles indicate that the mean velocity as a result of pure shear (Couette flow) is equal for laminar and turbulent flows. The mean velocity as a result of pressure-induced flow (Poiseuille flow), however, is reduced for turbulent flows as compared to laminar flows. Constantinescu plotted the different values of the mean pressure flow as a function of both axial and circumferential pressure gradients and Reynolds number. Empirical relationships for axial and circumferential flow follow by curve fitting of the data. These empirical relations can then be used to correct the pressure terms in a derivation similar to the procedure presented in [section 2.1](#). The final result is the following form of the Reynolds equation in which the Poiseuille flow terms are corrected for the effects of turbulence:

$$\frac{\partial}{\partial \bar{x}} \left( \frac{\bar{\beta} \bar{h}^3}{\bar{\mu}} G_x \frac{\partial \bar{\rho}}{\partial \bar{x}} \right) + \frac{\partial}{\partial \bar{z}} \left( \frac{\bar{\beta} \bar{h}^3}{\bar{\mu}} G_z \frac{\partial \bar{\rho}}{\partial \bar{z}} \right) = \Lambda \frac{\partial(\bar{\rho} \bar{h})}{\partial \bar{x}} + 2\Lambda \frac{\partial \bar{\rho} \bar{h}}{\partial \bar{t}} \quad (2.41)$$

With  $\alpha_x = 0.0136$ ,  $\beta_x = 0.90$ ,  $\alpha_z = 0.0043$  and  $\beta_z = 0.96$ , the semi-empirical turbulence correction factors are written as:

$$G_x = \left( 1 + \frac{\alpha_x}{12} Re^{\beta_x} \right)^{-1} \quad (2.42)$$

$$G_z = \left( 1 + \frac{\alpha_z}{12} Re^{\beta_z} \right)^{-1} \quad (2.43)$$

The correction factors [Equation 2.42](#) and [Equation 2.43](#) are valid for Reynolds numbers within the range of  $1000 < Re < 30000$ .

The governing equations presented above are based on simplified turbulent theory in which the effect of turbulent fluctuations on the mean flow is modelled using the Prandtl mixing length hypothesis. The result is the inclusion of turbulent viscosity into the Reynolds equation. Durany, Pereira-Pérez and Varas performed a 3D large Eddy simulation using a Smagorinsky-type model in order to determine the range of validity of the simplified turbulent model as presented in this section. [21] In their work they considered the modelling of thrust pad bearings. They concluded that the results in terms of pressure and load capacity are adequate for lubrication flows in the laminar-turbulent transient regimes. In fully turbulent flow regimes the pressures and load capacities were underestimated by the model of Constantinescu. Considering that the models as discussed in this section are computationally efficient and seem to present conservative estimates of the bearing performance characteristics they are deemed sufficient for the current analysis.

## 2.4. Perturbed Reynolds Equation

In the previous sections, the unsteady Reynolds equation was derived. In principle, a time-integration of the Reynolds equation could be coupled with the rotor-dynamic equations of motion in order to analyse the dynamic characteristics of gas bearing supported rotors. This would allow for determining the complete non-linear rotor orbits, but such a procedure is rather computationally expensive. In this work, a perturbation method is used to solve the equations instead. By introducing small harmonic motions around the journal equilibrium position a perturbed density field can be computed. This allows for the calculation of stiffness and damping coefficients to be used in a linearized rotor-dynamic model. Since the purpose of the analysis is only to predict the onset of instability and not to compute the evolution of rotor orbits, this perturbation method is deemed sufficient.

The perturbation method for solving the Reynolds equations and obtaining the stiffness and damping coefficients was first published by Lund.[22] Lund used the method to obtain the bearing impedances for tilting pad journal bearing and a three-lobe journal bearing. For compressible flows, the bearing impedances are a function of the excitation frequency of the journal. Guenat and Schiffmann applied the method to obtain a frequency-dependent perturbed density field for bearings subject to non-ideal thermodynamic effects.[23] In their work, the viscosity of the fluid was assumed to be constant. Bi, Han and Yang applied the frequency perturbation method to obtain a perturbed pressure field by embracing

perturbations in all variables including viscosity.[24] Dynamic characteristics were presented for a plain journal bearing operating with supercritical carbon dioxide as a lubricant.

In this work, a similar approach will be used where the Reynolds equation is solved using the perturbation method in order to obtain the perturbed density field. The starting point of the derivation is the unsteady, turbulent Reynolds equation written in terms of the effective bulk modulus  $\kappa_{Te}$ :

$$\frac{\partial}{\partial \bar{x}} \left( \bar{h}^3 \bar{\kappa}_{Te} G_x \frac{\partial \bar{\rho}}{\partial \bar{x}} \right) + \frac{\partial}{\partial \bar{z}} \left( \bar{h}^3 \bar{\kappa}_{Te} G_z \frac{\partial \bar{\rho}}{\partial \bar{z}} \right) = \Lambda \frac{\partial (\bar{\rho} \bar{h})}{\partial \bar{x}} + 2\Lambda \frac{\partial (\bar{\rho} \bar{h})}{\partial \bar{t}} \quad (2.44)$$

The effective bulk modulus is defined in terms of the bulk modulus and dynamic viscosity as:

$$\kappa_{Te} = \frac{\beta}{\mu} \quad (2.45)$$

The effective bulk modulus is normalized using the conventions of the bulk modulus and viscosity. It is used here mainly as a short-hand notation since the effects of bulk modulus and viscosity will be analysed separately.

In a stable, steady-state condition the bearing will operate at a steady eccentricity  $\epsilon_0$  and attitude angle  $\psi_0$  otherwise expressed as the  $X$ - and  $Y$ -components of the eccentricity as:

$$\begin{aligned} \epsilon_{0X} &= \epsilon_0 \cos(\psi_0) \\ \epsilon_{0Y} &= \epsilon_0 \sin(\psi_0) \end{aligned} \quad (2.46)$$

A small harmonic motion with non-dimensional excitation frequency  $\gamma = \frac{\omega}{\Omega}$  is introduced around this equilibrium position leading to a disturbance in the steady state film thickness given by:

$$\bar{h}(\bar{x}) = \bar{h}_0(\bar{x}) + \bar{h}_d(\bar{x}) = 1 - \epsilon_{0X} \cos(\bar{x}) - \epsilon_{0Y} \sin(\bar{x}) - \epsilon_{1X} \cos(\bar{x}) e^{i\gamma \bar{t}} - \epsilon_{1Y} \sin(\bar{x}) e^{i\gamma \bar{t}} \quad (2.47)$$

This disturbed film thickness will in turn lead to a disturbance in the steady state density field  $\bar{\rho}_0$  and effective bulk modulus  $\bar{\kappa}_{Te0}$ :

$$\bar{\rho} = \bar{\rho}_0 + \epsilon_{1X} \bar{\rho}_{1X} e^{i\gamma \bar{t}} + \epsilon_{1Y} \bar{\rho}_{1Y} e^{i\gamma \bar{t}} \quad (2.48)$$

$$\bar{\kappa}_{Te} = \bar{\kappa}_{Te0} + \epsilon_{1X} \left( \frac{\partial \bar{\kappa}_{Te}}{\partial \bar{\rho}} \right)_0 \bar{\rho}_{1X} e^{i\gamma \bar{t}} + \epsilon_{1Y} \left( \frac{\partial \bar{\kappa}_{Te}}{\partial \bar{\rho}} \right)_0 \bar{\rho}_{1Y} e^{i\gamma \bar{t}} \quad (2.49)$$

The partial derivative of the effective bulk modulus with respect to density at constant temperature can be evaluated by applying the chain rule:

$$\left. \frac{\partial \kappa_{Te}}{\partial \rho} \right|_T = \frac{\kappa_{Te}}{\rho} + \frac{\rho}{\mu} \left. \frac{\partial^2 p}{\partial \rho^2} \right|_T - \frac{\kappa_{Te}}{\mu} \left. \frac{\partial \mu}{\partial \rho} \right|_T \quad (2.50)$$

Furthermore, the turbulence correction factors are a function of the local Reynolds number and therefore of film thickness  $\bar{h}$ , density  $\bar{\rho}$  and viscosity  $\bar{\mu}$ . The perturbed turbulence correction factors can be derived using the chain rule and are presented below:

$$\begin{aligned} G = G_0 + \epsilon_{1X} \left[ \left( \frac{\partial G}{\partial \bar{\rho}} \right)_0 \bar{\rho}_{1X} + \left( \frac{\partial G}{\partial \bar{h}} \right)_0 \cos(\bar{x}) + \left( \frac{\partial G}{\partial \bar{\mu}} \right)_0 \left( \frac{\partial \bar{\mu}}{\partial \bar{\rho}} \right)_0 \bar{\rho}_{1X} \right] e^{i\gamma \bar{t}} + \\ \epsilon_{1Y} \left[ \left( \frac{\partial G}{\partial \bar{\rho}} \right)_0 \bar{\rho}_{1Y} + \left( \frac{\partial G}{\partial \bar{h}} \right)_0 \sin(\bar{x}) + \left( \frac{\partial G}{\partial \bar{\mu}} \right)_0 \left( \frac{\partial \bar{\mu}}{\partial \bar{\rho}} \right)_0 \bar{\rho}_{1Y} \right] e^{i\gamma \bar{t}} \end{aligned} \quad (2.51)$$

The partial derivatives of the turbulence correction factors are written as:

$$\left( \frac{\partial G}{\partial \bar{\rho}} \right)_0 = -G_0^2 \beta \frac{\alpha}{12} Re_0^\beta \frac{1}{\bar{\rho}_0} \quad (2.52)$$

$$\left(\frac{\partial G}{\partial \bar{h}}\right)_0 = -G_0^2 \beta \frac{\alpha}{12} R e_0^\beta \frac{1}{\bar{h}_0} \quad (2.53)$$

$$\left(\frac{\partial G}{\partial \bar{\mu}}\right)_0 = G_0^2 \beta \frac{\alpha}{12} R e_0^\beta \frac{1}{\bar{\mu}_0} \quad (2.54)$$

Finally, now that expressions have been obtained for all the perturbed quantities of interest [Equation 2.47](#), [Equation 2.48](#), [Equation 2.49](#) and [Equation 2.51](#) can be substituted into the unsteady Reynolds equation [Equation 2.44](#). All higher-order terms are neglected and only the zeroth order and first-order terms remain. The zeroth order terms and the first order terms in  $X$ - and  $Y$ - directions can be grouped and separated. The zeroth order equation is written as:

$$\frac{\partial}{\partial \bar{x}} \left( \bar{h}_0^3 G_{0x} \bar{\kappa}_{Te0} \frac{\partial \bar{\rho}_0}{\partial \bar{x}} \right) + \frac{\partial}{\partial \bar{z}} \left( \bar{h}_0^3 G_{z0} \bar{\kappa}_{Te0} \frac{\partial \bar{\rho}_0}{\partial \bar{z}} \right) = \Lambda \frac{\partial (\bar{\rho}_0 \bar{h}_0)}{\partial \bar{x}} \quad (2.55)$$

The first order equation for a perturbation in  $X$ -direction:

$$\begin{aligned} & \frac{\partial}{\partial \bar{x}} \left( \bar{h}_0^3 \bar{\kappa}_{Te0} G_{x0} \frac{\partial \bar{\rho}_{1X}}{\partial \bar{x}} \right) + \frac{\partial}{\partial \bar{z}} \left( \bar{h}_0^3 \bar{\kappa}_{Te0} G_{z0} \frac{\partial \bar{\rho}_{1X}}{\partial \bar{z}} \right) + \\ & \quad \frac{\partial}{\partial \bar{x}} \left( \bar{h}_0^3 \left( \frac{\partial \bar{\kappa}_{Te}}{\partial \bar{\rho}} \right)_0 \bar{\rho}_{1X} G_{x0} \frac{\partial \bar{\rho}_0}{\partial \bar{x}} \right) + \frac{\partial}{\partial \bar{z}} \left( \bar{h}_0^3 \left( \frac{\partial \bar{\kappa}_{Te}}{\partial \bar{\rho}} \right)_0 \bar{\rho}_{1X} G_{z0} \frac{\partial \bar{\rho}_0}{\partial \bar{z}} \right) + \\ & \frac{\partial}{\partial \bar{x}} \left( \bar{h}_0^3 \bar{\kappa}_{Te0} \left[ \left( \frac{\partial G_x}{\partial \bar{\rho}} \right)_0 + \left( \frac{\partial G_x}{\partial \bar{\mu}} \right)_0 \left( \frac{\partial \bar{\mu}}{\partial \bar{\rho}} \right)_0 \right] \bar{\rho}_{1X} \frac{\partial \bar{\rho}_0}{\partial \bar{x}} \right) + \frac{\partial}{\partial \bar{z}} \left( \bar{h}_0^3 \bar{\kappa}_{Te0} \left[ \left( \frac{\partial G_z}{\partial \bar{\rho}} \right)_0 + \left( \frac{\partial G_z}{\partial \bar{\mu}} \right)_0 \left( \frac{\partial \bar{\mu}}{\partial \bar{\rho}} \right)_0 \right] \bar{\rho}_{1X} \frac{\partial \bar{\rho}_0}{\partial \bar{z}} \right) \\ & = -\frac{\partial}{\partial \bar{x}} \left( \bar{h}_0^3 \bar{\kappa}_{Te0} \left[ 3G_{x0} + \left( \frac{\partial G_x}{\partial \bar{h}} \right)_0 \right] \cos(\bar{x}) \frac{\partial \bar{\rho}_0}{\partial \bar{x}} \right) - \frac{\partial}{\partial \bar{z}} \left( \bar{h}_0^3 \bar{\kappa}_{Te0} \left[ 3G_{z0} + \left( \frac{\partial G_z}{\partial \bar{h}} \right)_0 \right] \cos(\bar{x}) \frac{\partial \bar{\rho}_0}{\partial \bar{z}} \right) + \\ & \quad \Lambda \frac{\partial}{\partial \bar{x}} (\bar{\rho}_0 \cos(\bar{x}) + \bar{\rho}_{1X} \bar{h}_0) + i2\gamma \Lambda (\bar{\rho}_0 \cos(\bar{x}) + \bar{\rho}_{1X} \bar{h}_0) \quad (2.56) \end{aligned}$$

Similarly, the first order equation for a perturbation in  $Y$ -direction:

$$\begin{aligned} & \frac{\partial}{\partial \bar{x}} \left( \bar{h}_0^3 \bar{\kappa}_{Te0} G_{x0} \frac{\partial \bar{\rho}_{1Y}}{\partial \bar{x}} \right) + \frac{\partial}{\partial \bar{z}} \left( \bar{h}_0^3 \bar{\kappa}_{Te0} G_{z0} \frac{\partial \bar{\rho}_{1Y}}{\partial \bar{z}} \right) + \\ & \quad \frac{\partial}{\partial \bar{x}} \left( \bar{h}_0^3 \left( \frac{\partial \bar{\kappa}_{Te}}{\partial \bar{\rho}} \right)_0 \bar{\rho}_{1Y} G_{x0} \frac{\partial \bar{\rho}_0}{\partial \bar{x}} \right) + \frac{\partial}{\partial \bar{z}} \left( \bar{h}_0^3 \left( \frac{\partial \bar{\kappa}_{Te}}{\partial \bar{\rho}} \right)_0 \bar{\rho}_{1Y} G_{z0} \frac{\partial \bar{\rho}_0}{\partial \bar{z}} \right) + \\ & \frac{\partial}{\partial \bar{x}} \left( \bar{h}_0^3 \bar{\kappa}_{Te0} \left[ \left( \frac{\partial G_x}{\partial \bar{\rho}} \right)_0 + \left( \frac{\partial G_x}{\partial \bar{\mu}} \right)_0 \left( \frac{\partial \bar{\mu}}{\partial \bar{\rho}} \right)_0 \right] \bar{\rho}_{1Y} \frac{\partial \bar{\rho}_0}{\partial \bar{x}} \right) + \frac{\partial}{\partial \bar{z}} \left( \bar{h}_0^3 \bar{\kappa}_{Te0} \left[ \left( \frac{\partial G_z}{\partial \bar{\rho}} \right)_0 + \left( \frac{\partial G_z}{\partial \bar{\mu}} \right)_0 \left( \frac{\partial \bar{\mu}}{\partial \bar{\rho}} \right)_0 \right] \bar{\rho}_{1Y} \frac{\partial \bar{\rho}_0}{\partial \bar{z}} \right) \\ & = -\frac{\partial}{\partial \bar{x}} \left( \bar{h}_0^3 \bar{\kappa}_{Te0} \left[ 3G_{x0} + \left( \frac{\partial G_x}{\partial \bar{h}} \right)_0 \right] \sin(\bar{x}) \frac{\partial \bar{\rho}_0}{\partial \bar{x}} \right) - \frac{\partial}{\partial \bar{z}} \left( \bar{h}_0^3 \bar{\kappa}_{Te0} \left[ 3G_{z0} + \left( \frac{\partial G_z}{\partial \bar{h}} \right)_0 \right] \sin(\bar{x}) \frac{\partial \bar{\rho}_0}{\partial \bar{z}} \right) + \\ & \quad \Lambda \frac{\partial}{\partial \bar{x}} (\bar{\rho}_0 \sin(\bar{x}) + \bar{\rho}_{1X} \bar{h}_0) + i2\gamma \Lambda (\bar{\rho}_0 \sin(\bar{x}) + \bar{\rho}_{1X} \bar{h}_0) \quad (2.57) \end{aligned}$$

[Equation 2.55](#) can be solved for the steady-state density field along with the steady effective bulk modulus and turbulence correction factors. Once this steady-state solution is obtained, the second-order linear partial differential equations [Equation 2.56](#) and [Equation 2.57](#) can be solved for  $\bar{\rho}_{1X}$  and  $\bar{\rho}_{1Y}$  respectively.

## 2.5. Foil Modelling in Gas Bearings

The theory presented in the previous sections dealt with the modelling of the gas film as applicable to rigid bearings. A simple example of a rigid bearing is a plain journal bearing in which no enhancements to the geometry are made to increase overall bearing performance. Such bearings typically lack sufficient load capacity and stability for practical applications. Amongst the most promising bearing

geometries is the gas foil bearing. Gas foil bearings are compliant surface bearings which deform under the action of increased pressure in the gas film. A schematic of a first-generation gas foil journal bearing is shown in Figure 2.5. [2] The compliant geometry consists of a bump foil and a top foil. Both the bump and top foil are typically spot welded to the housing of the bearing. The gas film is entrapped between the top foil and the surface of the shaft. The aerodynamic pressures that are generated as a result of the rotation of the shaft cause the elastic bump foils to deform leading to a redistribution of the film thickness. This will in turn lead to a redistribution of the pressure field as compared to rigid bearings.

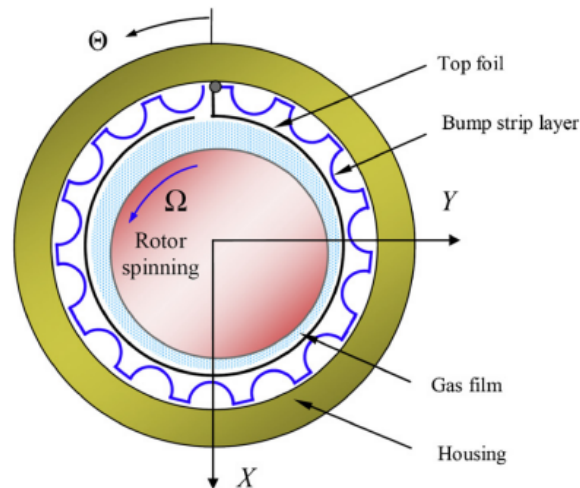


Figure 2.5: Schematic of a first-generation gas foil journal bearing.[2]

The so-called first-generation gas foil bearings have a constant structural stiffness in circumferential and axial directions. More advanced designs in which the structural stiffness is varied in one or more directions are typically referred to as second and third-generation gas foil bearings, respectively. [9] In this work, only the modelling of first-generation gas foil journal bearings will be considered.

The first models of gas foil journal bearings were presented by Heshmat, Walowit and Pinkus as early as 1983.[25] In their work the compliant structure of bump and top foil is modelled as a simple elastic foundation in which the structural deformation is linearly proportional to the pressures within the gas film. In the following decades, more sophisticated models have been proposed in scientific literature. San Andrés and Ho Kim, for example, present a model of gas foil journal bearings in which the top foil is modelled using a finite element method. [2] In their work both a 1D and 2D finite element model are presented accounting for the sagging of the top foil as a result of pressure variations in either circumferential or both circumferential and axial direction. Carpino and Talmaga have presented a method in which the fluid dynamics governed by the Reynolds equation is combined with the structural deflections in a single fully coupled finite element.[26] The use of elaborate finite element models for the structural deflections, however, can significantly increase the complexity and computational time of the solver. Furthermore, the improved accuracy of such methods compared to simple elastic models has proven to be relatively modest relative to the increased complexity of the computation. For this reason, the methods presented by Heshmat, Walowit and Pinkus still find application in recent literature on the modelling of gas foil bearings. In this work, this simple elastic model will be used in order to analyse the performance of gas foil journal bearings operating with non-ideal compressible flows.

A schematic of a gas foil bearing in which the structural deformations are approximated using a simple elastic model is shown in Figure 2.6. As shown in the figure, the bump foil structure is replaced with linear springs around the circumference of the bearing. The pressure exerted on the top foil will cause these springs to locally deform which will lead to an increase of the film thickness as compared to a rigid foundation.

In Figure 2.7 a schematic is shown in which a local bump structure is replaced with an elastic spring. Following the work of San Andrés and Ho Kim, the deformation of the bump foil structure is denoted by  $w_d$ . [5] The structural deflections as shown in the figure can be calculated using the pressure in the lubricating film:

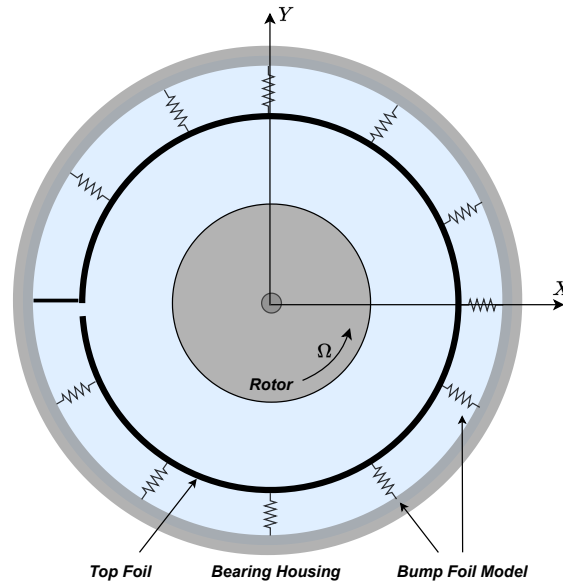


Figure 2.6: Schematic of a gas foil bearing where the bump foil is modelled using a simple elastic model.

$$w_d = \frac{\delta p}{K_f} \quad (2.58)$$

The parameter  $\delta p$  refers to an axially averaged pressure difference between the fluid above and underneath the top foil. For the steady-state pressure field, this pressure difference is written as:

$$\delta p_0 = \frac{1}{L} \int_{-L/2}^{L/2} (p_0 - p_{ref}) dz \quad (2.59)$$

The steady non-dimensional film thickness accounting for the bump foil structural deflections can now be written as:

$$\bar{h}_0 = 1 - \epsilon \cos(\bar{x} - \psi) + S \delta \bar{p}_0 \quad (2.60)$$

Where  $S = \frac{p_{ref}}{h_0 K_f}$  is defined as the compliance ratio. It is a non-dimensional parameter defining the ratio of fluid film stiffness to structural stiffness. Note that the film thickness depends on the structural deflections through Equation 2.60. Solving the steady-state Reynolds equation (Equation 2.55) requires knowledge of the film thickness distribution and therefore of the bump foil deflections. Since the structural deflections are in turn dependent on the fluid film pressures the numerical procedure will involve the simultaneous solution of the fluid and structural models.

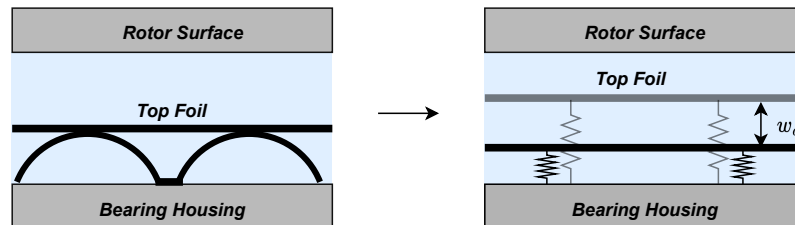


Figure 2.7: Modelling of the bump foil structure by elastic springs. Local bump foil deflections are indicated with  $w_d$ .

Similar to the analysis of plain journal bearings, the calculation of the linearized stiffness and damping coefficients requires the solution of the perturbed density field. For gas foil bearings, however, the perturbations in the pressure field will lead to small changes in the structural deflections. The perturbed film thickness for a gas foil journal bearing is computed as:

$$\bar{h} = 1 - \epsilon_{0X} \cos(\bar{x}) - \epsilon_{0Y} \sin(\bar{x}) + S \delta \bar{p}_0 - \epsilon_{1X} \cos(\bar{x}) e^{i\gamma \bar{t}} - \epsilon_{1Y} \sin(\bar{x}) e^{i\gamma \bar{t}} + \frac{S}{(1 + i\gamma_S)} (\delta \bar{p}_{1X} \epsilon_{1X} + \delta \bar{p}_{1Y} \epsilon_{1Y}) e^{i\gamma \bar{t}} \quad (2.61)$$

With  $\delta \bar{p}_{1X}$  and  $\delta \bar{p}_{1Y}$  representing the axially averaged perturbation in the pressure field in response to a journal displacement in  $X$ - and  $Y$ - direction respectively:

$$\begin{aligned} \delta \bar{p}_{1X} &= \frac{1}{L} \int_{-L/2}^{L/2} \left. \frac{\partial \bar{p}}{\partial \bar{\rho}} \right|_T \bar{\rho}_{1X} dz \\ \delta \bar{p}_{1Y} &= \frac{1}{L} \int_{-L/2}^{L/2} \left. \frac{\partial \bar{p}}{\partial \bar{\rho}} \right|_T \bar{\rho}_{1Y} dz \end{aligned} \quad (2.62)$$

The parameter  $\gamma_S$  represents a structural damping coefficient.[5] This parameter represents the effects of material hysteresis and dry-sliding friction between the top and bump foils and is typically taken to be around 0.40. The derivation of the first-order equations for the perturbed density field is as presented before and the resulting equation applicable for gas foil bearings is shown below for  $\bar{\rho}_{1X}$ :

$$\begin{aligned} &\frac{\partial}{\partial \bar{x}} \left( \bar{h}_0^3 \bar{\kappa}_{Te0} G_{x0} \frac{\partial \bar{\rho}_{1X}}{\partial \bar{x}} \right) + \frac{\partial}{\partial \bar{z}} \left( \bar{h}_0^3 \bar{\kappa}_{Te0} G_{z0} \frac{\partial \bar{\rho}_{1X}}{\partial \bar{z}} \right) + \\ &\quad \frac{\partial}{\partial \bar{x}} \left( \bar{h}_0^3 \left( \frac{\partial \bar{\kappa}_{Te}}{\partial \bar{\rho}} \right)_0 \bar{\rho}_{1X} G_{x0} \frac{\partial \bar{\rho}_0}{\partial \bar{x}} \right) + \frac{\partial}{\partial \bar{z}} \left( \bar{h}_0^3 \left( \frac{\partial \bar{\kappa}_{Te}}{\partial \bar{\rho}} \right)_0 \bar{\rho}_{1X} G_{z0} \frac{\partial \bar{\rho}_0}{\partial \bar{z}} \right) + \\ &\frac{\partial}{\partial \bar{x}} \left( \bar{h}_0^3 \bar{\kappa}_{Te0} \left[ \left( \frac{\partial G_x}{\partial \bar{\rho}} \right)_0 + \left( \frac{\partial G_x}{\partial \bar{\mu}} \right)_0 \left( \frac{\partial \bar{\mu}}{\partial \bar{\rho}} \right)_0 \right] \bar{\rho}_{1X} \frac{\partial \bar{\rho}_0}{\partial \bar{x}} \right) + \frac{\partial}{\partial \bar{z}} \left( \bar{h}_0^3 \bar{\kappa}_{Te0} \left[ \left( \frac{\partial G_z}{\partial \bar{\rho}} \right)_0 + \left( \frac{\partial G_z}{\partial \bar{\mu}} \right)_0 \left( \frac{\partial \bar{\mu}}{\partial \bar{\rho}} \right)_0 \right] \bar{\rho}_{1X} \frac{\partial \bar{\rho}_0}{\partial \bar{z}} \right) + \\ &\quad \frac{\partial}{\partial \bar{x}} \left( 3 \bar{h}_0^2 \frac{S}{(1 + i\gamma_S)} \delta \bar{p}_{1X} \bar{\kappa}_{Te0} G_{x0} \frac{\partial \bar{\rho}_0}{\partial \bar{x}} \right) + \frac{\partial}{\partial \bar{z}} \left( 3 \bar{h}_0^2 \frac{S}{(1 + i\gamma_S)} \delta \bar{p}_{1X} \bar{\kappa}_{Te0} G_{z0} \frac{\partial \bar{\rho}_0}{\partial \bar{z}} \right) = \\ &\quad - \frac{\partial}{\partial \bar{x}} \left( \bar{h}_0^2 \bar{\kappa}_{Te0} \left[ 3G_{x0} + \left( \frac{\partial G_x}{\partial \bar{h}} \right)_0 \right] \cos(\bar{x}) \frac{\partial \bar{\rho}_0}{\partial \bar{x}} \right) - \frac{\partial}{\partial \bar{z}} \left( \bar{h}_0^2 \bar{\kappa}_{Te0} \left[ 3G_{z0} + \left( \frac{\partial G_z}{\partial \bar{h}} \right)_0 \right] \cos(\bar{x}) \frac{\partial \bar{\rho}_0}{\partial \bar{z}} \right) + \\ &\Lambda \frac{\partial}{\partial \bar{x}} \left( \bar{\rho}_0 \cos(\bar{x}) + \bar{\rho}_0 \frac{S}{(1 + i\gamma_S)} \delta \bar{p}_{1X} + \bar{\rho}_{1X} \bar{h}_0 \right) + i2\gamma\Lambda \left( \bar{\rho}_0 \cos(\bar{x}) + \bar{\rho}_0 \frac{S}{(1 + i\gamma_S)} \delta \bar{p}_{1X} + \bar{\rho}_{1X} \bar{h}_0 \right) \end{aligned} \quad (2.63)$$

An equation similar to Equation 2.63 can be written for  $\bar{\rho}_{1Y}$ .

## 2.6. Bearing Performance Characteristics

Once the steady-state and perturbed density fields are computed, the bearing performance characteristics can be obtained. Within this work, the load-carrying capacity will be used as a measure of the steady-state bearing performance. The critical mass is used to investigate effects related to rotor-dynamic stability.

In order to compute the bearing load capacity, the static pressure field is integrated around the shaft. The components of the bearing load capacity are obtained as:

$$W_x = -R^2 p_{ref} \int_{-L/D}^{L/D} \int_0^{2\pi} \bar{p} \cos(\bar{x}) d\bar{x} d\bar{z} \quad (2.64)$$

$$W_y = -R^2 p_{ref} \int_{-L/D}^{L/D} \int_0^{2\pi} \bar{p} \sin(\bar{x}) d\bar{x} d\bar{z} \quad (2.65)$$

$$W = \sqrt{W_x^2 + W_y^2} \quad (2.66)$$

In which the non-dimensional pressure is redefined as  $\bar{p} = \frac{p}{p_{ref}}$  and can be computed as a function of the density field and the reference temperature using the thermodynamic software programs. A non-dimensional form of the bearing load capacity is defined as:

$$\bar{W} = \frac{W}{R^2 p_{ref}} \quad (2.67)$$

The dynamic characteristics are governed by the bearing impedances which are determined using the components of the perturbed pressure field as:

$$Z_{xx} = -R^2 p_{ref} \int_{-L/D}^{L/D} \int_0^{2\pi} \bar{p}_x \cos(\bar{x}) d\bar{x} d\bar{z} \quad (2.68)$$

$$Z_{yx} = -R^2 p_{ref} \int_{-L/D}^{L/D} \int_0^{2\pi} \bar{p}_x \sin(\bar{x}) d\bar{x} d\bar{z} \quad (2.69)$$

$$Z_{xy} = -R^2 p_{ref} \int_{-L/D}^{L/D} \int_0^{2\pi} \bar{p}_y \cos(\bar{x}) d\bar{x} d\bar{z} \quad (2.70)$$

$$Z_{yy} = -R^2 p_{ref} \int_{-L/D}^{L/D} \int_0^{2\pi} \bar{p}_y \sin(\bar{x}) d\bar{x} d\bar{z} \quad (2.71)$$

Where the non-dimensional perturbed pressure field can again be computed using a thermodynamic software program and the perturbed density field as:

$$\bar{p}_{x,y} = \frac{\rho_{ref}}{p_{ref}} \left. \frac{\partial p}{\partial \rho} \right|_T \bar{\rho}_{x,y} \quad (2.72)$$

Note that the bearing impedance consists of the stiffness and damping coefficients. For the  $Z_{xy}$  component for example:

$$Z_{xy} = K_{xy} + i\omega C_{xy} \quad (2.73)$$

With  $\omega_{ex}$  the excitation frequency at which the shaft is perturbed.

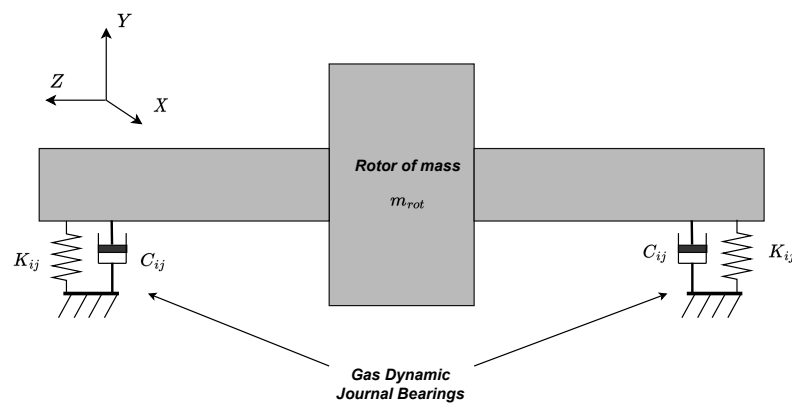


Figure 2.8: Simplified schematic of a rigid rotor supported on gas dynamic bearings.

The stiffness and damping coefficients can be used in a linearized rotor-dynamic model in order to analyse the stability of the rotor. Rotors supported by gas dynamic bearings typically operate at a rotational speed well below the first rotor bend mode. In this work, the dynamics of a rigid rotor-bearing system will therefore be considered. As an example, a simplified schematic is shown of a

symmetric rotor-bearing system with two identical bearings in [Figure 2.8](#). The cylindrical rigid body mode will be analysed where the longitudinal axis of the rotor remains parallel to the initial orientation and the whirl motions within both bearings are in phase.

The equations of motion of the rotating system with the linearized bearing reaction forces can then be written as:

$$\begin{bmatrix} m_{rot} & 0 \\ 0 & m_{rot} \end{bmatrix} \begin{bmatrix} \Delta\ddot{X} \\ \Delta\ddot{Y} \end{bmatrix} + \begin{bmatrix} C_{xx} & C_{xy} \\ C_{yx} & C_{yy} \end{bmatrix} \begin{bmatrix} \Delta\dot{X} \\ \Delta\dot{Y} \end{bmatrix} + \begin{bmatrix} K_{xx} & K_{xy} \\ K_{yx} & K_{yy} \end{bmatrix} \begin{bmatrix} \Delta X \\ \Delta Y \end{bmatrix} = \begin{bmatrix} 0 \\ 0 \end{bmatrix} \quad (2.74)$$

With  $m_{rot}$  the mass of the rotor and  $\Delta X$  and  $\Delta Y$  indicating the deviation from the rotor equilibrium position in  $X$ - and  $Y$ -direction respectively. Note that [Equation 2.74](#) is valid for a rotor without external forcing caused by mass imbalance. In this analysis, only the self-sustained motions are considered. The potential growth of small amplitude journal motions from the equilibrium position leading to sub-synchronous vibration is a typical instability observed in hydrodynamic journal bearings.[\[27\]](#)

The Laplace transformed notation of [Equation 2.74](#) with the mass matrix indicated with  $M$  and the impedance matrix indicated with  $Z$  can be written as: [\[28\]](#)

$$[Ms^2 + Z] \vec{q} e^{st} \quad (2.75)$$

The impedance matrix is written using the components defined by [Equation 2.73](#). The vector  $\vec{q}$  contains the amplitudes of the journal motion around the equilibrium rotor position. Whether these amplitudes grow or decay in time is governed by the sign of the damping coefficient  $\lambda$  of the Laplace variable  $s = \lambda + i\omega$ . [Equation 2.75](#) can be split into two independent equations governing the forward and backward rotor whirls by diagonalization of the impedance matrix leading to the equivalent bearing impedances:[\[27\]](#)

$$Z_{eq} = \frac{1}{2} (Z_{xx} + Z_{yy}) \pm \sqrt{\frac{1}{4} (Z_{xx} - Z_{yy})^2 + Z_{xy}Z_{yx}} = u(\omega_{ex}) + iv(\omega_{ex}) \quad (2.76)$$

The parameters  $u$  and  $v$  in [Equation 2.76](#) represent the equivalent stiffness and damping of the bearing, respectively. As the equation indicates, these parameters both depend on the rotor excitation frequency  $\omega_{ex} = \gamma\Omega$ . This is also apparent from the appearance of the ratio of excitation frequency to rotor speed  $\gamma$  in the perturbed density equations ([Equation 2.56](#) and [Equation 2.57](#)) and this is a result of the compressibility of the gas. In order to find the point where the rotor motion just becomes unstable, the neutral stability point is considered. At neutral stability the real part of the Laplace variable  $s$  is zero ( $\lambda = 0$ ). In order for the diagonalized [Equation 2.75](#) to hold, the equivalent damping ( $v(\omega_{ex})$ ) must be zero. At this condition the critical mass can be written as:

$$m_{cr} = \frac{u(\omega_{ex})}{\omega_{ex}^2} \quad (2.77)$$

In other words, in order for the rotor-bearing system to become unstable at a given rotational speed  $\Omega$  the mass carried by one journal bearing is given by [Equation 2.77](#). The whirling motion or excitation frequency  $\omega_{ex}$  at which this instability occurs is such that the bearing equivalent damping is zero. Note that [Equation 2.77](#) can be re-arranged as:

$$\omega_{ex} = \sqrt{\frac{u(\omega_{ex})}{m_{cr}}} \quad (2.78)$$

Indicating that the whirl frequency is equal to the undamped natural frequency of the rotor-bearing system with mass  $m_{cr}$ . This mass will be referred to as the critical mass and it indicates a limit mass that the bearing can carry dynamically. The difference between the critical mass and the actual rotor mass presents a stability margin for bearing operation at a given rotational speed. Note that a rotor is typically supported by two journal bearings. The system would then become unstable at a given  $\Omega$  if the total rotor mass  $m_{rot}$  is larger than twice the critical mass assuming that the two bearings are identical. A non-dimensional form of the critical mass parameter will be used in this work defined as:

$$\bar{m}_{cr} = \frac{m_{cr}\Omega^2 h_0}{R^2 p_{ref}} \quad (2.79)$$

This section is concluded with a summary of the different equations used to obtain the performance parameters for either a plain journal bearing or a gas foil bearing as shown in [Table 2.2](#). The table indicates that the same steady-state or zeroth-order Reynolds equation is solved for both types of bearings. The difference, however, is in how the film thickness is evaluated. This difference also translates into different forms of the first-order or perturbed Reynolds equation used to obtain the critical mass.

Bearing Performance Parameter	Bearing Type	Equation Label
Perturbed film thickness	PJB	<a href="#">Equation 2.47</a>
Load capacity	PJB	<a href="#">Equation 2.55</a>
Critical mass	PJB	<a href="#">Equation 2.56</a> & <a href="#">Equation 2.57</a>
Perturbed film thickness	GFB	<a href="#">Equation 2.61</a>
Load capacity	GFB	<a href="#">Equation 2.55</a>
Critical mass	GFB	<a href="#">Equation 2.63</a> (similar form for $Y$ -component)

Table 2.2: Form of the (Reynolds) equation used to solve for the perturbed film thickness and performance parameters of plain journal bearings and gas foil bearings.

## 2.7. Numerical Solution Method for the Reynolds Equation

In the previous sections, the flow equations governing the gas dynamic bearings have been presented. The steady-state non-dimensional density field can be obtained by solving [Equation 2.55](#). The perturbed density field is governed by [Equation 2.56](#) and [Equation 2.57](#) for a plain journal bearing and can be extended for gas foil bearings as done for the  $X$ -component in [Equation 2.63](#). In this section, the numerical solution of these equations is discussed as implemented in the computational tool developed as part of this research. The tool is called GasBearingSim and the link to the GitHub repository can be found in [Appendix A](#). Finally, this chapter and the computational tool are summarized by means of flow diagrams indicating the step-by-step procedure used to obtain the steady-state and dynamic characteristics of gas foil journal bearings. An overview will be given of the equations solved at each step of the numerical procedure.

In order to solve the partial differential equations the appropriate boundary conditions need to be specified. For the steady-state or zeroth order Reynolds equation, a Dirichlet boundary condition is applied at the axial sides of the bearing imposing a steady-state density equal to the density in the surrounding compartment. A periodic boundary condition is applied in circumferential direction. For gas foil bearings the density at the circumferential location of the top and bump foil spot weld is also imposed to equal the reference density due to a slight gap between the top foil leading and trailing edges. The boundary conditions for the zeroth order equation are written formally as:

$$\begin{aligned}
 \bar{\rho}_0(\bar{x}, -L/D) &= \bar{\rho}_0(\bar{x}, L/D) = 1 \\
 \bar{\rho}_0(0, \bar{z}) &= \bar{\rho}_0(2\pi, \bar{z}) \quad \text{for a PJB} \\
 \bar{\rho}_0(0, \bar{z}) &= \bar{\rho}_0(2\pi, \bar{z}) = 1 \quad \text{for a GFB}
 \end{aligned} \tag{2.80}$$

For the perturbed Reynolds equations and the associated perturbed density fields a Dirichlet boundary condition is again applied at the axial sides of the bearing. The perturbations from the steady-state density are imposed to be zero at the sides. The perturbed density field is periodic in circumferential direction with zero perturbations at the foil weld location for a gas foil bearing:

$$\begin{aligned}
 \bar{\rho}_{1x,y}(\bar{x}, -L/D) &= \bar{\rho}_{1x,y}(\bar{x}, L/D) = 0 \\
 \bar{\rho}_{1x,y}(0, \bar{z}) &= \bar{\rho}_{1x,y}(2\pi, \bar{z}) \quad \text{for a PJB} \\
 \bar{\rho}_{1x,y}(0, \bar{z}) &= \bar{\rho}_{1x,y}(2\pi, \bar{z}) = 0 \quad \text{for a GFB}
 \end{aligned} \tag{2.81}$$

To solve the equations, the partial derivatives need to be discretized. In literature the finite difference and finite element methods are the most common approaches to solving the Reynolds equation.[\[29\]](#) The Reynolds equation is a convection-diffusion equation in which the compressibility number  $\Lambda$  determines the relative significance of the convective terms compared to the diffusive terms.

For low bearing numbers, the equation has an elliptic nature where the diffusive terms dominate the solution. For large bearing numbers, the convective terms become dominant and the equation becomes increasingly parabolic. In the latter case, the numerical scheme might have trouble satisfying the downstream boundary conditions with numerical oscillations as a result. A typical remedy of this problem is the use of upwind schemes in the numerical procedures. In this research, however, the compressibility numbers of interest are well below 100 and numerical oscillations do not cause significant problems. Therefore, a second-order central differencing scheme is used. The first- and second-order derivatives of the general flow parameter  $\xi$  indicating, for example, the density can then be written in circumferential and axial direction as:

$$\left(\frac{\partial \xi}{\partial \bar{x}}\right)_{i,j} = \frac{\xi_{i+1,j} - \xi_{i-1,j}}{2\Delta\bar{x}} + O(\Delta\bar{x}^2) \quad (2.82)$$

$$\left(\frac{\partial^2 \xi}{\partial \bar{x}^2}\right)_{i,j} = \frac{\xi_{i+1,j} - 2\xi_{i,j} + \xi_{i-1,j}}{\Delta\bar{x}^2} + O(\Delta\bar{x}^2) \quad (2.83)$$

$$\left(\frac{\partial \xi}{\partial \bar{z}}\right)_{i,j} = \frac{\xi_{i,j+1} - \xi_{i,j-1}}{2\Delta\bar{z}} + O(\Delta\bar{z}^2) \quad (2.84)$$

$$\left(\frac{\partial^2 \xi}{\partial \bar{z}^2}\right)_{i,j} = \frac{\xi_{i,j+1} - 2\xi_{i,j} + \xi_{i,j-1}}{\Delta\bar{z}^2} + O(\Delta\bar{z}^2) \quad (2.85)$$

In order to evaluate the finite difference equations, the gas film is discretized using the computational grid shown in Figure 2.9. The grid contains  $n + 1$  nodal points in circumferential direction and  $m + 1$  points in axial direction. The parameters  $\Delta\bar{x}$  and  $\Delta\bar{z}$  represent the spacing between the nodes in circumferential and axial direction, respectively.

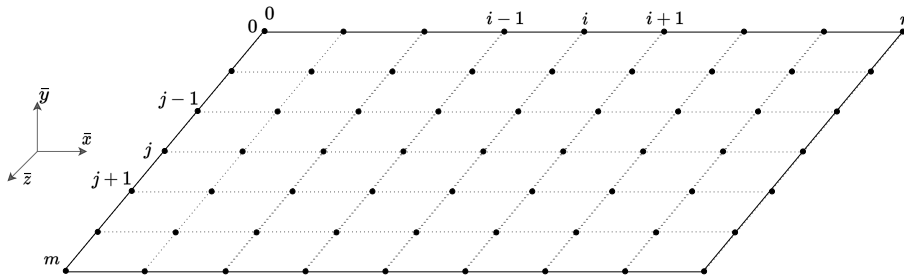


Figure 2.9: Discretization of the fluid domain in circumferential and axial directions.

In order to determine a suitable number of grid nodes in circumferential and axial direction for the computational mesh, a grid refinement study is performed. In Figure 2.10 the relative error is plotted in terms of load capacity and critical mass as compared to a reference solution on a refined mesh with  $n = 150$  and  $m = 100$ . The relative error is defined for the load capacity as:

$$\text{Relative Error} = \frac{\bar{W} - \bar{W}_{ref}}{\bar{W}_{ref}} \quad (2.86)$$

With a similar definition of the relative error for the critical mass. The plots show a relative error of load capacity smaller than 1% for a mesh with about 300 nodes, whereas the critical mass requires more refinement in order to obtain the same accuracy. The load capacity ratio seems to converge faster for equal number of intervals in axial and circumferential direction for an axial width-to-diameter ratio of 1. The relative distribution of grid points in axial and circumferential direction seems to have less of an influence on the critical mass as compared to the load capacity according to the figures.

The Reynolds equation is non-linear since the bulk modulus and dynamic viscosity depend on the local value of the density. Furthermore, for gas foil bearings the foil deflections and thus film thickness depend on the local pressure difference between the thin film and the fluid under the top foil. This pressure difference is in turn a function of the density field. In order to linearize the equation, the thermodynamic fluid properties and the foil deflections are evaluated using the density computed at the

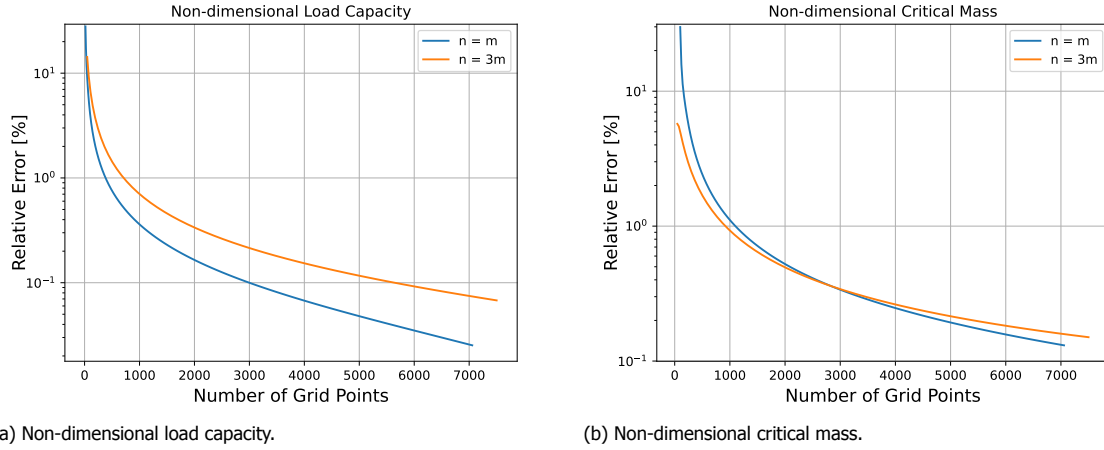


Figure 2.10: Convergence of non-dimensional load capacity and critical mass as function of grid refinement for  $n = m$  and  $n = 3m$ . Reference solution is computed with  $n = 150$  and  $m = 100$ .

previous iteration. Therefore, to start the iteration procedure an initial estimate of the non-dimensional density field is required which is typically taken to be  $\bar{\rho} = 1$  throughout the domain. The bulk modulus and viscosity are then computed as a function of this local density and the reference temperature  $T_{ref}$  by means of the thermodynamic software programs RefProp or CoolProp. [30], [31] The discretization of the Reynolds equation then leads to the following linear system to be solved for the non-dimensional density:

$$A(\bar{\rho}) \cdot \vec{\rho} = \vec{b} \quad (2.87)$$

In which the matrix  $A$  is a function of the density and therefore needs to be re-evaluated at each iteration. A Gauss-Seidel successive under-relaxation method is applied to iteratively compute the solution of the non-linear problem through successive solution of the discretized linear system of equations:

$$\vec{\rho}^{k+1} = \vec{\rho}^k + \kappa \left( A^{-1}(\vec{\rho}^k) \cdot \vec{b} - \vec{\rho}^k \right) \quad (2.88)$$

For most computations in this research, a relaxation factor of  $\kappa = 0.3$  to  $0.5$  was found to be sufficient for convergence. A convergence threshold can be defined as follows:

$$\max \left( \left| \frac{\bar{\rho}^{k+1} - \bar{\rho}^k}{\bar{\rho}^k} \right| \right) < 10^{-6} \quad (2.89)$$

Although for coarser meshes this threshold can typically be set to a larger value (e.g.  $10^{-4}$ ).

Note that the procedure described above assumes that the film thickness is known, which requires the knowledge of bearing eccentricity  $\epsilon$  and attitude angle  $\psi$ . In practice, the applied external load is often known instead or the bearing eccentricity is known but the attitude angle is unknown. In these cases, a Newton-Raphson procedure is applied in order to find the equilibrium position of the shaft.

In order to solve the first-order equations governing the perturbed density field again a second-order central differencing scheme is applied. The equations are second order, linear partial differential equations and discretization directly leads to a linear system for the perturbed density requiring no successive approximation method. In order to set up the linear system, however, the steady-state solution needs to be computed first.

The complete procedure of computing the performance characteristics of a gas foil bearing can be summarized using flow diagrams. In Figure 2.11 a flow diagram is shown indicating the steps in obtaining the solution to the steady-state or zeroth order Reynolds equation. The diagram summarizes the computation for a given external load to be supported by the bearing at a given rotational speed. The different steps and iterative methods involved are indicated. Some of the steps shown in Figure 2.11 are numbered in green. In Table 2.3 an overview is given of the associated equations solved in the corresponding steps. The rows of the table are ordered in accordance with the flow diagram. Some of the most important parameters obtained upon solving the equations are indicated in the table as well.

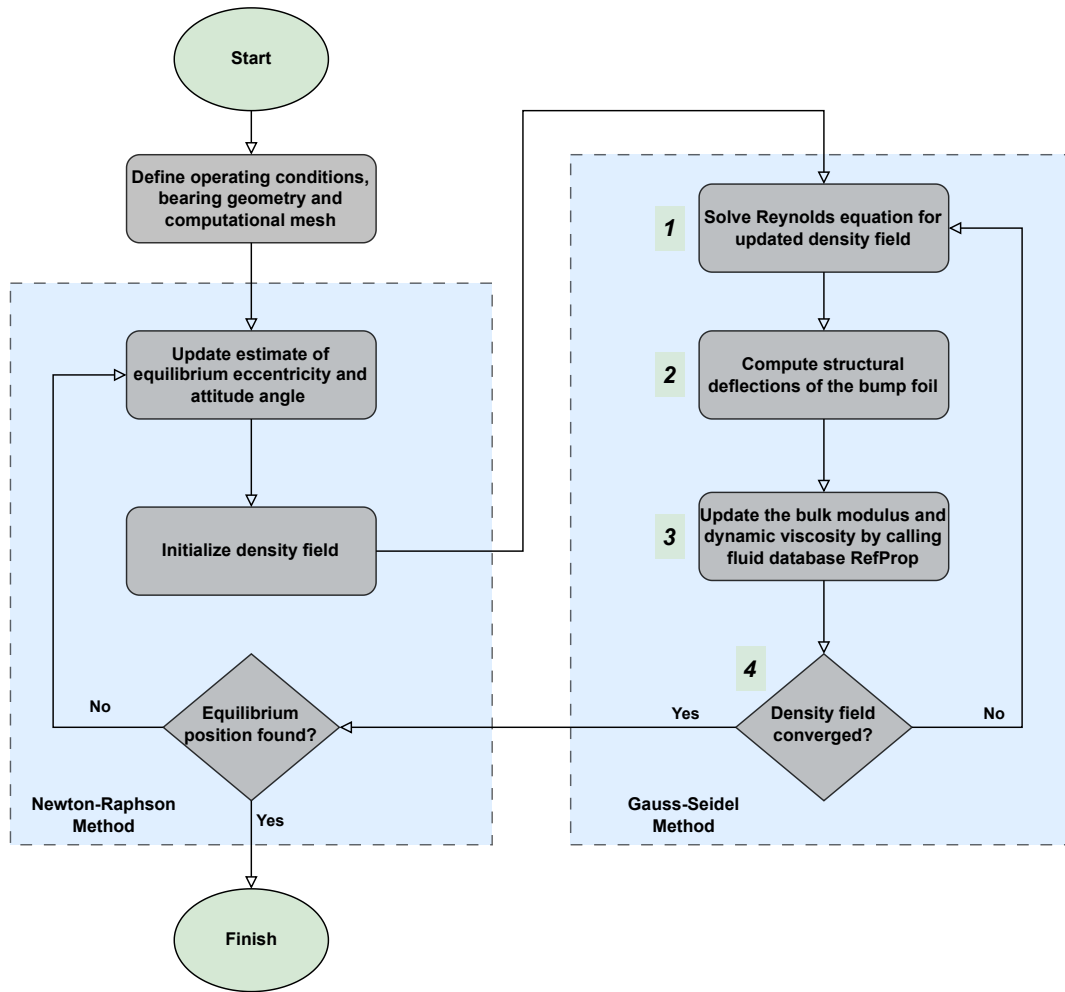


Figure 2.11: Flow diagram of the solution procedure used to obtain the steady-state bearing properties.

Step	Objective	In Iterative Loop	Type of Model	Parameters Solved For	Equation
1a	Discretize Reynolds equation	Yes	Partial differential equation	$A(\bar{\rho})$ and $\bar{b}$	Equation 2.55
1b	Update density field	Yes	Discretized linear system	$\bar{\rho}^{k+1}$	Equation 2.88
2	Update foil deflections and film thickness	Yes	Algebraic	$w_d$ and $\bar{h}$	Equation 2.58 & Equation 2.60
3	Compute thermodynamic parameters	Yes	Thermodynamic software	$\bar{\beta}$ and $\bar{\mu}$	RefProp/CoolProp
4	Check convergence of density field	Yes	Algebraic	$\left  \frac{\bar{\rho}^{k+1} - \bar{\rho}^k}{\bar{\rho}^k} \right $	Equation 2.89
5	Compute thin film pressure distribution	No	Thermodynamic software	$\bar{p}_0$	RefProp/CoolProp
6	Compute load capacity	No	Integration	$W_x$ and $W_y$	Equation 2.64 & Equation 2.65

Table 2.3: Summary of the steps and equations involved in computing the steady-state load capacity of a gas foil bearing.

The procedure for calculating the solution to the first-order perturbed Reynolds equation and obtaining the dynamic bearing characteristics is shown in Figure 2.12. The figure shows how the iterative method is applied to approximate the shaft excitation frequency at which the bearing has zero equivalent damping. The steps are again numbered in green to the right of the blocks. The numbers refer to Table 2.4, which indicates the relevant equations that are solved at each step. Note that the equations presented in the table are associated to the analysis of gas foil bearings. The relevant equations might differ slightly for plain journal bearings as was shown in Table 2.2.

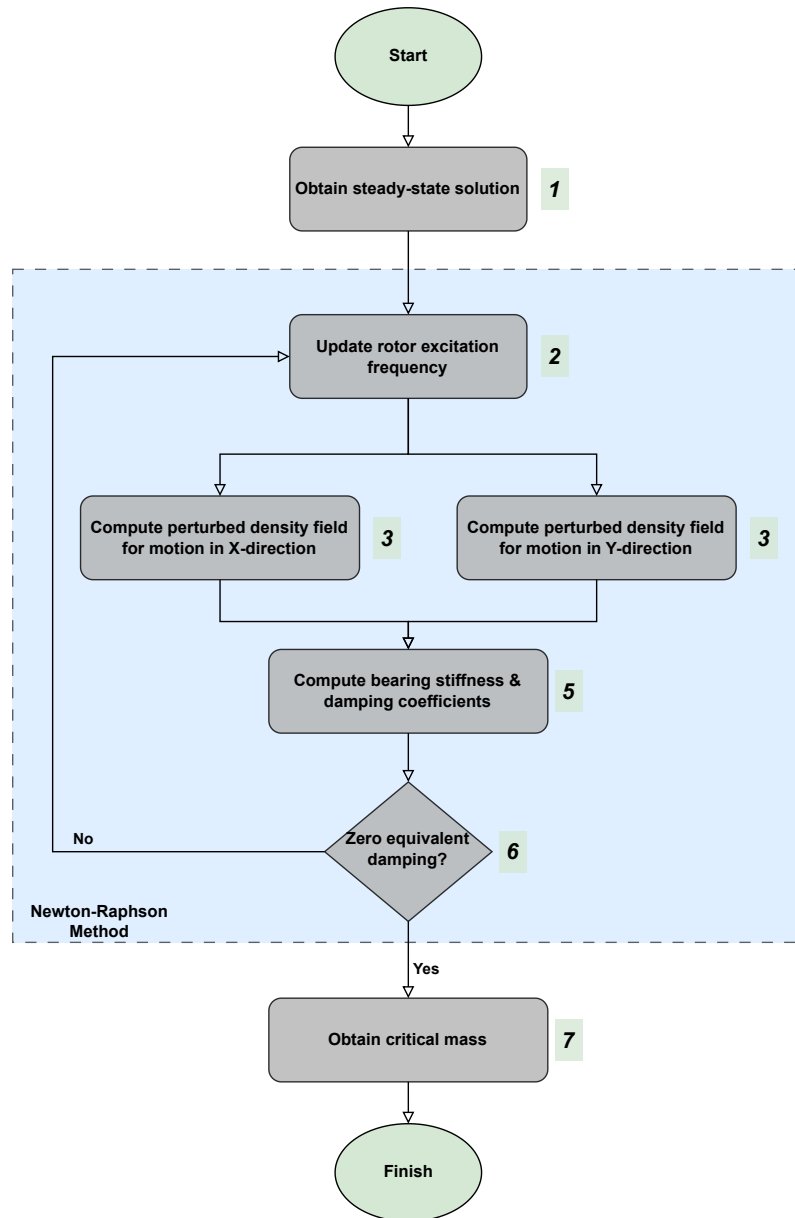


Figure 2.12: Flow diagram of the solution procedure used to obtain the dynamic bearing properties.

Step	Objective	In Iterative Loop	Type of Model	Parameters Solved For	Equation
1	Obtain steady-state solution	No	Steady-state analysis	$\bar{\rho}_0, \bar{\kappa}_{Te0}, G_0$ and $\bar{h}_0$	Table 2.3
2	Update excitation frequency	Yes	Root-finding procedure	$\omega_{ex}$	Newton-Raphson
3a	Discretize perturbed Reynolds equations	Yes	Partial differential equation	$A(\bar{\rho})$ and $\bar{b}$	Equation 2.63
3b	Solve both first order perturbed Reynolds equations	Yes	Discretized linear system	$\bar{\rho}_x$ and $\bar{\rho}_y$	Equation 2.87
4	Compute perturbed pressure field	Yes	Thermodynamic software	$\bar{p}_x$ and $\bar{p}_y$	Equation 2.72 & RefProp/CoolProp
5	Compute bearing stiffness and damping coefficients	Yes	Integration	$K_{i,j}$ and $C_{i,j}$	Equation 2.68 - Equation 2.71
6	Check if equivalent damping equals zero	Yes	Algebraic	$v(\omega_{eq})$	Equation 2.76
7	Compute critical mass	No	Algebraic	$m_{cr}$	Equation 2.77

Table 2.4: Summary of the steps and equations involved in computing the rotor-dynamic critical mass of a gas foil bearing.

# 3

## Results for Rigid Gas Bearings

Over the last decades, gas dynamic bearings have found application in small-scale turbomachinery such as air cycle machines, environmental control systems or cryogenic pumps. For most of these applications, the lubricant behaves like an ideal gas and there has been no necessity to investigate the effects of non-ideal flows on the bearing performance. Modelling of bearings operating under such conditions allowed the governing equations to be simplified considerably. Although there is an increased interest in high-pressure gas lubrication in recent scientific literature, there is still a lack of generalization of non-ideal thermodynamic effects on lubrication flows. In this chapter, the performance of rigid gas bearings or plain journal bearings will be addressed. The focus is on how the bearing performance is affected by non-ideal thermodynamic effects in terms of steady-state load capacity and rotor-dynamic critical mass. The numerical results as obtained using the models presented in [chapter 2](#) will be verified and interpreted from a conceptual point of view. Initially, the discussion will be limited to laminar lubrication flows, followed by an analysis of the effects of turbulence in the final section of the chapter.

### 3.1. Verification of the Numerical Model

The computational model developed in this research will be used as a tool for gaining understanding of the physics in thin films of fluids in ideal and non-ideal thermodynamic conditions. Since there is little experimental data available at this stage for validation purposes, the software tool will be verified using numerical results available in scientific literature. The work of Guenat will be used to this end since his work shows results including non-ideal thermodynamic effects on steady and dynamic characteristics of plain journal bearings. [11] The solution of the Reynolds equation for laminar flows will be verified first. Afterwards, the inclusion of turbulence effects through the turbulent correction factors will be discussed.

The results presented in this section are for a plain journal bearing lubricated with the refrigerant R134a. For the simulations including non-ideal thermodynamic effects a reduced temperature of 1.0 was considered. Values between 0.1 and 0.8 have been used for the reduced pressure. The considered thermodynamic states are plotted on the reduced T-s thermodynamic plane of R134a along with the contours of the generalized isentropic pressure-volume exponent in [Figure 3.1](#).

#### 3.1.1. Laminar Flow

The first simulation is done for a bearing operating at a compressibility number of  $\Lambda = 1$ . The shaft has a non-dimensional eccentricity ratio of  $\epsilon = 0.6$ . The pressure distribution is calculated at the mid-span of the bearing as shown in [Figure 3.2](#). Results are shown for a computation using non-ideal flow effects with an ambient thermodynamic state of  $P_r = 0.75$  and  $T_r = 1.0$  in [Figure 3.2a](#). The same computation is done by applying the ideal gas assumption as shown in [Figure 3.2b](#). The results show a decrease in peak pressure and a redistribution of the pressure field for non-ideal flows. A good agreement is shown between the computed results and the results presented by Guenat.

In order to characterize the influence of non-ideal thermodynamic effects and fluid compressibility on the bearing load capacity, the load capacity ratio is introduced:

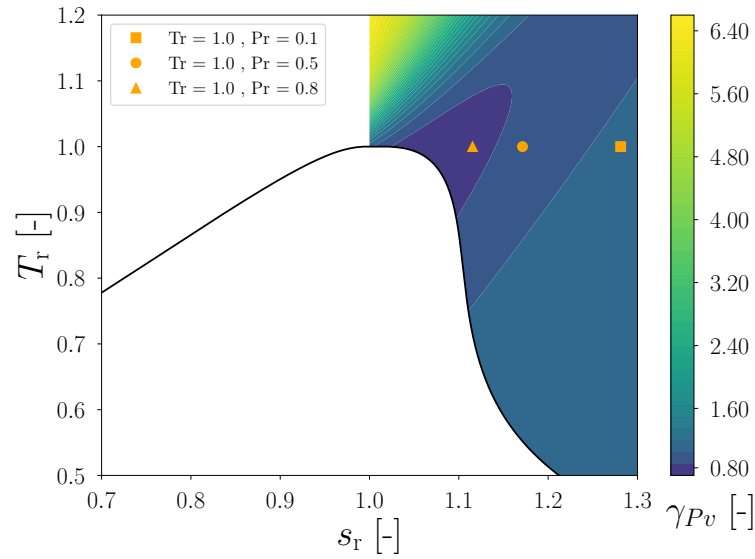
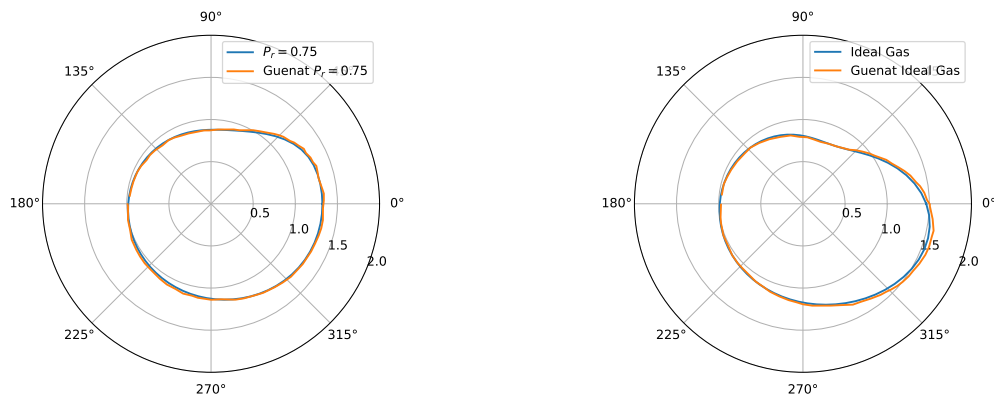


Figure 3.1: Bearing operating conditions for R134a as used for verification plotted on the reduced T-s thermodynamic plane.



(a) Non-Ideal Gas.

(b) Ideal Gas

Figure 3.2: Verification of the mid-span pressure distribution for non-ideal and ideal gasses.

$$\bar{W}_r = \frac{\bar{W}_{ng}}{\bar{W}_{ig}} \quad (3.1)$$

Where the subscripts  $ng$  and  $ig$  indicate non-ideal gas and ideal gas respectively. In Figure 3.3a the load capacity ratio is plotted for R134a at  $\epsilon = 0.2$ . The plot shows different values of the reduced temperature and pressure corresponding to different degrees of fluid compressibility. A decreasing trend is shown for the load capacity ratio versus compressibility number. The numerical results compare well with the results of Guenat.

In Figure 3.3b the locus of eccentricity is shown upon increasing the applied load. The results correspond to a bearing operating with R134a at  $\Lambda = 1$ . The components  $\epsilon_x$  and  $\epsilon_y$  relate to the eccentricity  $\epsilon$  and  $\psi$  according to:

$$\begin{aligned} \epsilon_x &= \epsilon \cos(\psi) \\ \epsilon_y &= \epsilon \sin(\psi) \end{aligned} \quad (3.2)$$

For increasing load on the bearing the eccentricity increases. The plot shows an initial attitude

angle of almost 90 degrees with a decreasing trend with increasing load. The eccentricity and attitude angle are shown to be different for different levels of fluid compressibility. Good agreement is obtained between numerical results and the results of Guenat.

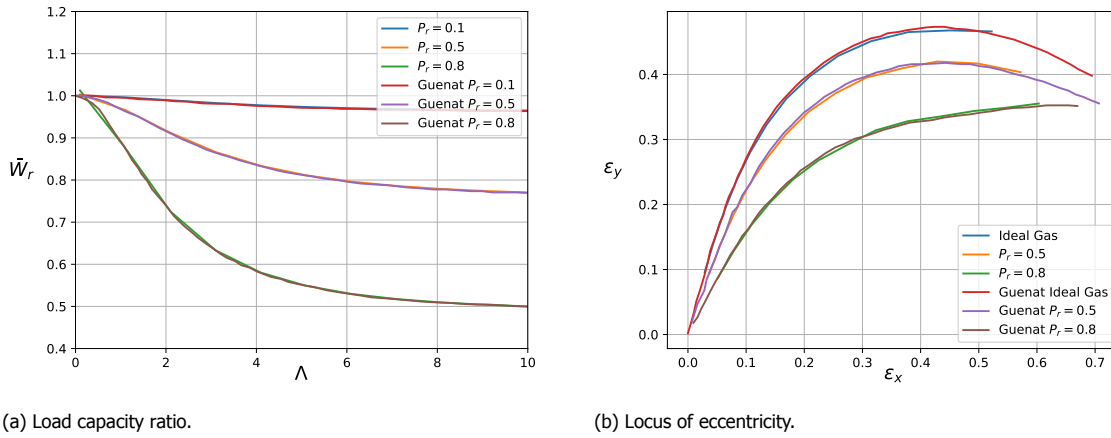


Figure 3.3: Verification of Load capacity ratio and steady-state eccentricity.

In order to characterize the influence of fluid compressibility on the dynamic characteristics of bearings, the critical mass ratio is introduced. The critical mass ratio specifies the ratio of the critical mass for a bearing lubricated with a non-ideal gas to a bearing lubricated with an ideal gas:

$$\bar{M}_r = \frac{\bar{M}_{cr,ng}}{\bar{M}_{cr,ig}} \tag{3.3}$$

The critical mass ratio is plotted for a plain journal bearing lubricated with R134a at  $\epsilon = 0.2$  in Figure 3.4. Note that the figure shows results of two different simulations. In Figure 3.4a the critical excitation frequency at which instability occurs is found using a root finding procedure for the imaginary part of the equivalent bearing impedance as explained in the previous chapter. Qualitatively, the trends agree with the results of Guenat. However, there is a small offset between the presented results. A possible explanation is the fact that there is a slight discrepancy between the excitation frequency found. The critical mass is sensitive to changes in the ratio of excitation frequency to shaft rotational speed as found in the root-finding procedure. In Figure 3.4b the same plot is shown in which the normalized excitation frequency is tuned manually and a better agreement is shown. The normalized excitation frequency as found manually is within 4% of the value found by a root finding procedure.

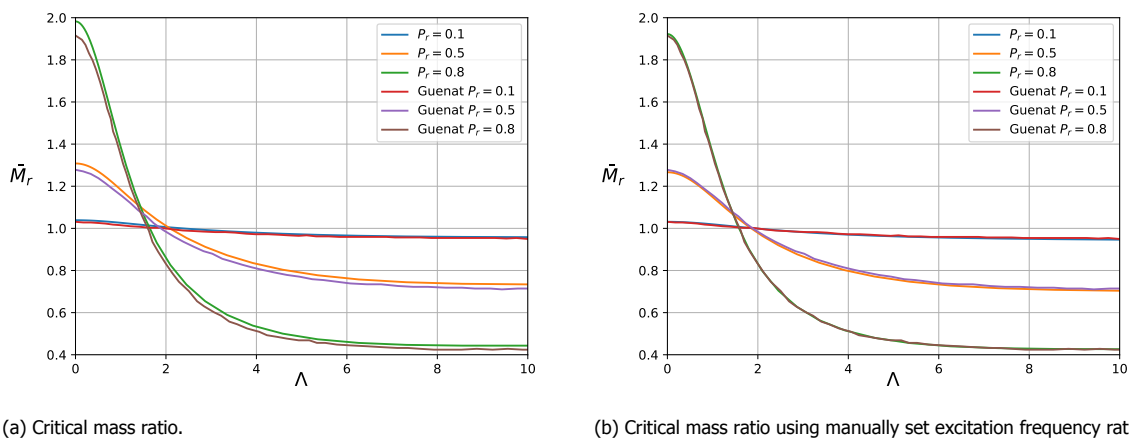


Figure 3.4: Verification of the laminar critical mass ratio.

### 3.1.2. Turbulent Flow

In order to investigate the effect of different Reynolds numbers on the bearing performance in a conceptual way, the Reynolds number can be set manually within the developed computational tool. In this section, the load capacity ratio and critical mass ratio are computed as a function of the bearing compressibility number for different Reynolds numbers. The numerical results are again compared to results presented by Guenat. [11]

The load capacity ratio for turbulent flow is presented in Figure 3.5. Results are shown for Reynolds numbers of  $Re = 5000, 10000$  and  $20000$ . The plot shows a larger decrease in load capacity ratio for increasing Reynolds numbers which will be discussed later in this chapter. A good agreement is shown with the data from literature.

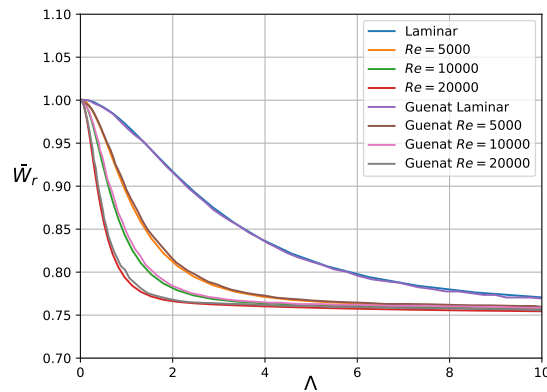


Figure 3.5: Verification of the turbulent load capacity ratio at different Reynolds numbers.

Finally, the dynamic bearing performance is verified for bearings operating in the turbulent regime. The critical mass ratio is plotted for Reynolds numbers of  $Re = 5000, 10000$  and  $20000$  as shown in Figure 3.6. Similar to the steady-state load capacity ratio, the critical mass ratio drops faster as a function of compressibility number for increasing Reynolds numbers. Note that the plots show a discrepancy with the results from literature similar to the laminar critical mass ratio presented before. The discrepancy appears to be larger for increasing Reynolds numbers.

In Figure 3.7 the same plot is shown in which the normalized excitation frequency is tuned manually to within 4% of the value found in a root finding procedure. In this way the agreement with data from literature can be improved, reinforcing the hypothesis that the error is due to a discrepancy in critical normalized excitation frequency. Note that although a slight offset is found in numerical results in the comparison with the results of Guenat, the discrepancy seems to be relatively small for compressibility numbers of interest. Given that the root finding procedure for obtaining the critical mass, this procedure has been applied in all subsequent analyses of bearing stability.

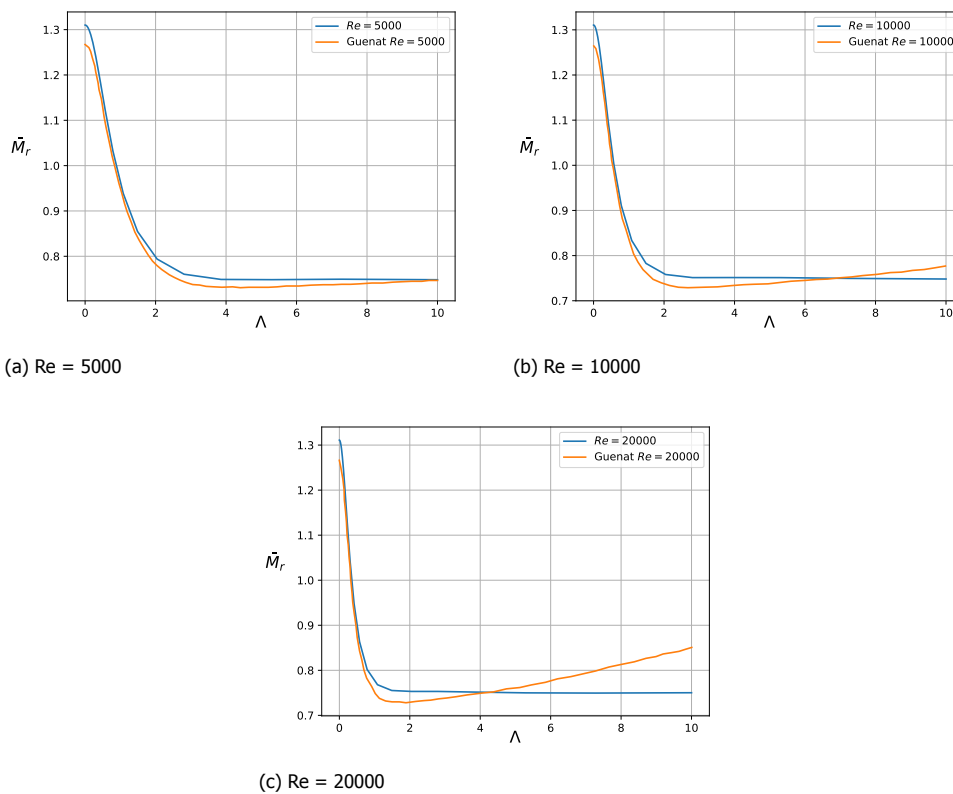


Figure 3.6: Verification of the turbulent critical mass ratio.

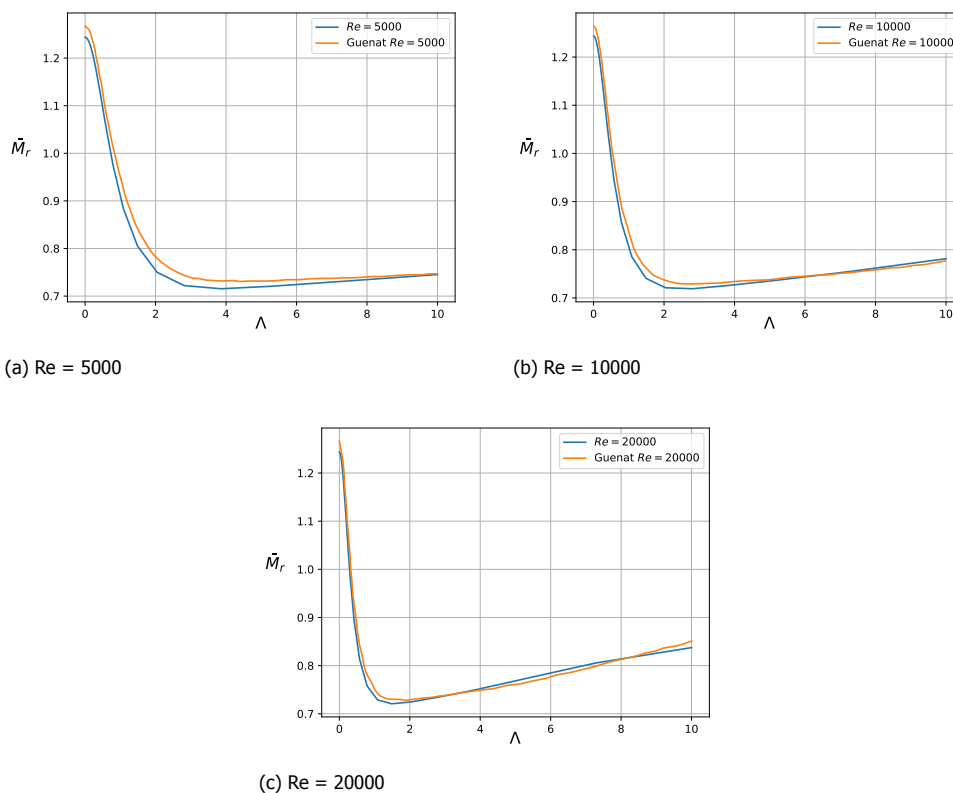


Figure 3.7: Verification of the turbulent critical mass ratio using manually set excitation frequency ratio.

### 3.2. Steady-State Bearing Performance

In this section, the steady-state bearing performance will be addressed. The steady-state performance is characterized by the bearing load capacity in this research. The basic principles of the generation of hydrodynamic pressure in journal bearings are discussed along with the influence of non-ideal thermodynamic effects on the resulting pressure field. The non-dimensional bulk modulus is shown to be the governing parameter introducing the non-ideal thermodynamic effects on bearing performance.

The results presented in this section are mostly for plain journal bearings lubricated with siloxane MM. For the simulations including non-ideal thermodynamic effects a reduced temperature of 1.1 was considered. For the reduced pressure, values between 0.5 and 2.2 have been considered in order to illustrate the physical concepts. The aforementioned thermodynamic states are plotted on the reduced T-s thermodynamic plane of siloxane MM along with the contours of the generalized isentropic pressure-volume exponent in [Figure 3.8](#).

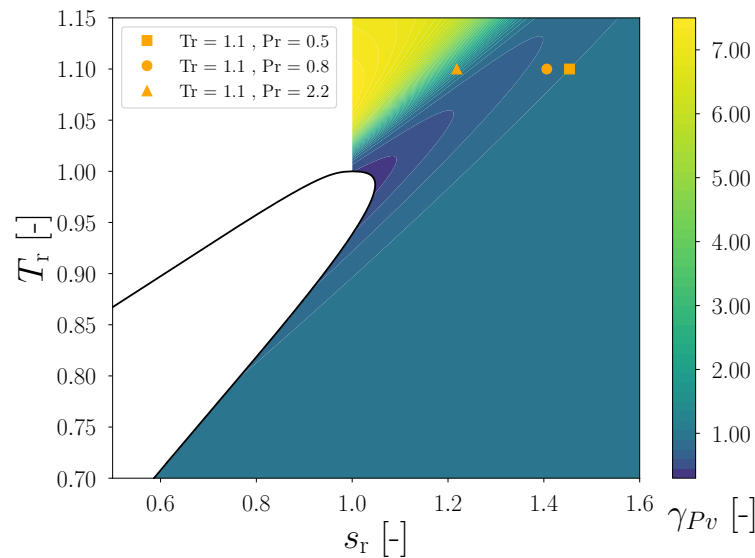


Figure 3.8: Bearing operating conditions for siloxane MM as considered in the current analysis plotted on the reduced T-s thermodynamic plane.

#### 3.2.1. Fundamental Operating Principles

The steady-state Reynolds equation ([Equation 2.55](#)) as derived in [chapter 2](#) is repeated below. The different terms related to Poiseuille flow and Couette flow are indicated in the equation.

$$\underbrace{\frac{\partial}{\partial \bar{x}} \left( \bar{h}_0^3 G_{0x} \frac{\bar{\rho}_0}{\bar{\mu}_0} \frac{\partial \bar{\rho}_0}{\partial \bar{x}} \right)}_{\text{Circumferential Poiseuille Flow Term}} + \underbrace{\frac{\partial}{\partial \bar{z}} \left( \bar{h}_0^3 G_{z0} \frac{\bar{\rho}_0}{\bar{\mu}_0} \frac{\partial \bar{\rho}_0}{\partial \bar{z}} \right)}_{\text{Axial Poiseuille Flow Term}} = \underbrace{\Lambda \frac{\partial (\bar{\rho}_0 \bar{h}_0)}{\partial \bar{x}}}_{\text{Couette Flow Term}} \quad (3.4)$$

As indicated in the equation, the fluid film is governed by the combined effects of Poiseuille flow and Couette flow. In order to generate a converging gap, an offset exists between the centre of the rotor and the centre of the bearing housing. This offset is referred to as the eccentricity. The driving Couette flow drags the fluid into an aerodynamic wedge which results in increased hydrodynamic pressure as illustrated in [Figure 3.9](#). The largest pressures are typically found near the point of minimum film thickness and as a result, a net pressure force is exerted on the rotor.

The trend of load capacity as a function of bearing eccentricity is shown in [Figure 3.10](#). The figure shows zero load capacity for a bearing at zero eccentricity. For a given rotational speed  $\Omega$  or bearing compressibility number  $\Lambda$  an increase in eccentricity will result in an increased non-dimensional load capacity. Initially, a linear trend can be observed which ultimately gives way to a strong rise in non-dimensional load capacity at large eccentricities. The plot also shows a larger sensitivity to the

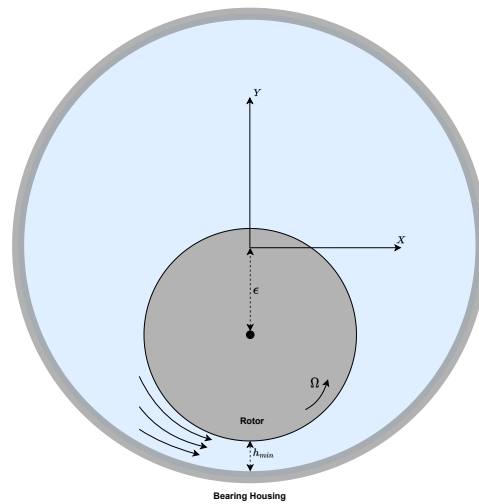


Figure 3.9: Schematic representation of the aerodynamic wedge action generating an increase in pressure.

lubricant thermodynamic state at large eccentricities. Note that increasing the load on the bearing for a given rotational speed or reducing the rotational speed for a given bearing loading will result in larger eccentricities.

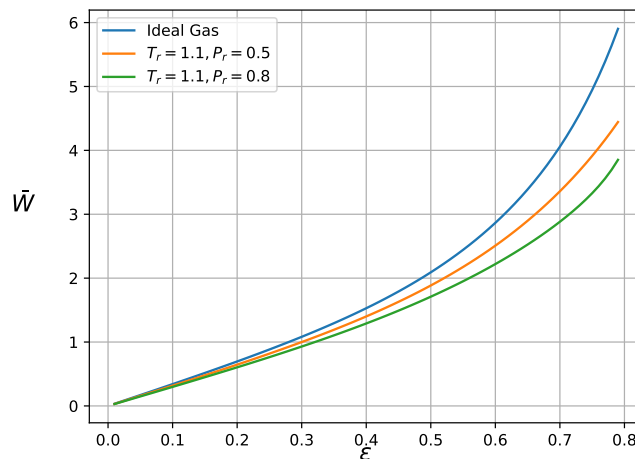


Figure 3.10: Effect of increasing shaft eccentricity on non-dimensional load capacity for a bearing lubricated with siloxane MM at  $\Lambda = 3.0$ .

By increasing the compressibility number, the driving Couette flow will start to dominate the flow physics in the Reynolds equation as indicated in Equation 3.4. The increasing compressibility number will directly affect the pressure distribution in the fluid film. In Figure 3.11 the mid-span pressure distribution is shown in a polar plot for a bearing lubricated with siloxane MM at an eccentricity of  $\epsilon = 0.7$ . Increased bearing compressibility numbers lead to larger pressures. Note that the results are plotted for operation at equal attitude angles.

The effect of increased compressibility number on load capacity is shown in Figure 3.12. The figure shows results for a bearing lubricated with siloxane MM at  $\epsilon = 0.2$ . A strong rise in non-dimensional load capacity is shown for low speed numbers. At large rotational speed, the Couette flow becomes dominant and the non-dimensional load capacity ultimately reaches a plateau.

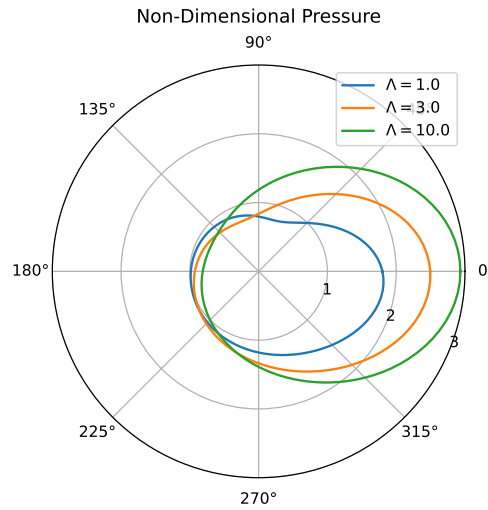


Figure 3.11: Effect of increasing bearing compressibility number on mid-span pressure distribution for siloxane MM at  $T_r = 1.1$  and  $P_r = 0.5$  with  $\epsilon = 0.7$ .

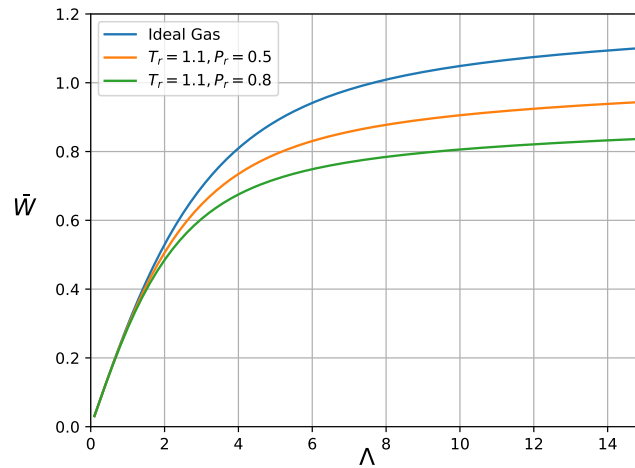


Figure 3.12: Effect of increasing bearing compressibility number on non-dimensional load capacity for a bearing lubricated with siloxane MM at  $\epsilon = 0.2$ .

### 3.2.2. Non-dimensional Bulk Modulus

In [Figure 3.12](#) the results are plotted for bearings operating in the dense gas regime and for an ideal gas. It is observed that the non-ideal flows exhibit a lower non-dimensional load capacity in particular for large  $\Lambda$ . To see how the non-ideal thermodynamic effects influence the flow dynamics the compressible Reynolds equation ([Equation 3.4](#)) is consulted. The equation shows that the non-dimensional bulk modulus and dynamic viscosity are the only fluid properties that enter the computational model and influence the resulting density field. In order to analyse the effect of the non-dimensional bulk modulus the normalized density field is plotted at mid-span for a bearing lubricated with siloxane MM at  $\Lambda = 3.0$  and  $\epsilon = 0.7$  assuming iso-viscous flow in [Figure 3.13a](#). Results are shown for a computation assuming ideal gas conditions as well as for  $P_r = 0.5$  and  $P_r = 0.8$  at  $T_r = 1.1$ . Note that the two latter cases correspond to a non-dimensional bulk modulus of  $\bar{\beta} = 0.86$  and  $\bar{\beta} = 0.76$  respectively. The figure shows an increase in the maximum density for a decrease in non-dimensional bulk modulus. Referring to [Equation 3.4](#) this increased density can be attributed to a decreased Poiseuille flow. The Poiseuille flow components in the Reynolds equation have a diffusive nature and therefore act to smoothen out the density field. A reduced non-dimensional bulk modulus corresponds to a fluid with increased

compressibility and this effectively has a similar impact as increasing the compressibility number  $\Lambda$  in the Reynolds equation.

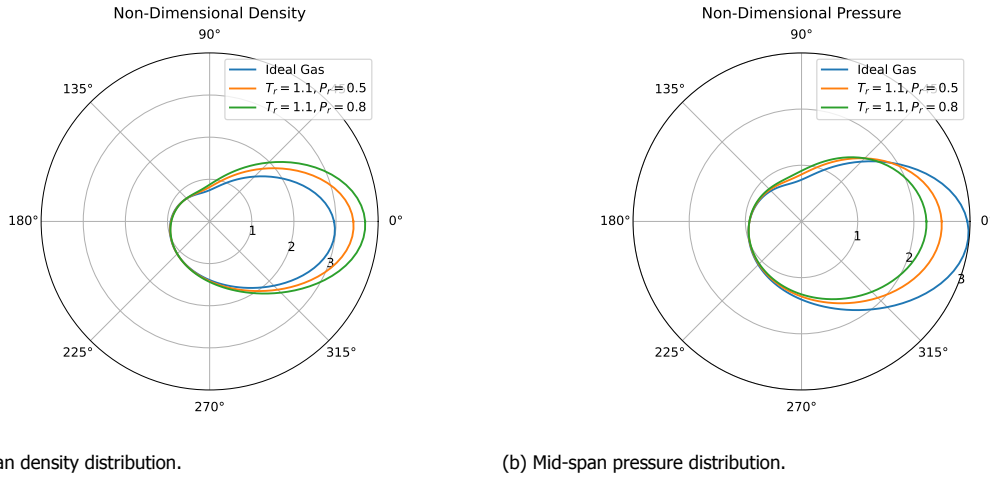


Figure 3.13: Mid-span non-dimensional density and pressure distributions for siloxane MM with  $\Lambda = 3.0$  and  $\epsilon = 0.7$  at different reduced reference pressures.

Although a decreased non-dimensional bulk modulus leads to an increase in maximum density in the fluid film, Figure 3.13b shows a decreased maximum pressure for the  $P_r = 0.5$  and  $P_r = 0.8$  solutions. The increased compressibility of the fluid closer to the thermodynamic critical point results in larger densities but lower peak pressures. In order to investigate the effects on overall load capacity from a different perspective, the ratio of non-ideal to ideal load capacity is used:

$$\bar{W}_r = \frac{\bar{W}_{n,g}}{\bar{W}_{i,g}} \quad (3.5)$$

The load capacity ratio is plotted for siloxane MM operating at different thermodynamic states in Figure 3.14. As a result of the reduced peak pressures compared to an ideal gas the solutions for  $P_r = 0.5$  and  $P_r = 0.8$  show load capacity ratios below one. The effect is more pronounced at increasing bearing speed numbers  $\Lambda$  as the driving Couette flow generates larger densities and therefore locally the influence of fluid compressibility is increased. Furthermore, a solution is shown for super-critical siloxane at  $T_r = 1.1$  and  $P_r = 2.2$ . This bearing is operating with large densities in the liquid-like part of the super-critical regime where the non-dimensional bulk modulus is increased to  $\bar{\beta} = 1.07$  resulting in load capacity ratios larger than one. Increased values of the bulk modulus result in larger film pressures and therefore larger load capacity. Due to its association with increased pressure variations for given density variations the bulk modulus is sometimes referred to as the stiffness of the fluid.

Contour plots of the non-dimensional bulk modulus are visualized on the reduced T-s thermodynamic plane for siloxane MM using NiceProp in Figure 3.15.[3] For large temperatures and low pressures the plot shows values of non-dimensional bulk modulus closer to one. In the limit of an ideal gas, the non-dimensional bulk modulus is equal to one, as:

$$\bar{\beta}_{ref} \equiv \left. \frac{\rho_{ref}}{p_{ref}} \frac{\partial p}{\partial \rho} \right|_T = \frac{\rho_{ref}}{p_{ref}} RT_{ref} = 1 \quad \text{for an ideal gas.} \quad (3.6)$$

Near the saturated vapour line and in the proximity of the thermodynamic critical point the fluid exhibits increased compressibility leading to values of  $\bar{\beta} < 1$  with a limiting value of  $\bar{\beta}_c = 0$  at the critical point. For super-critical fluids, the non-dimensional bulk modulus can be either lower than or larger than the value for ideal gasses. In particular Figure 3.15 shows strongly increasing values in the liquid-like regime where the fluid increasingly behaves like an incompressible medium.

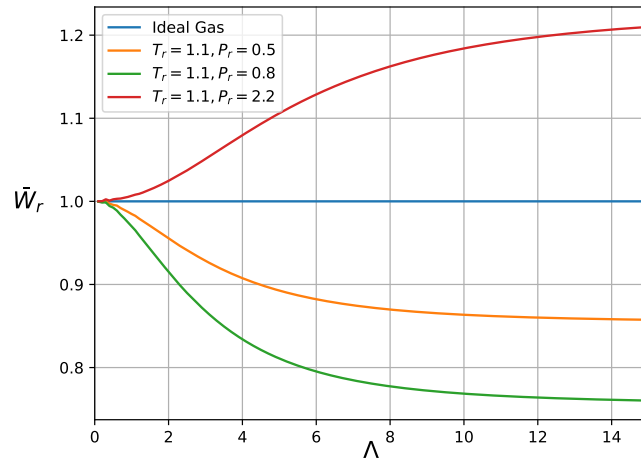


Figure 3.14: Effect of fluid compressibility on load capacity ratio for a bearing lubricated with siloxane MM at  $\epsilon = 0.2$ .

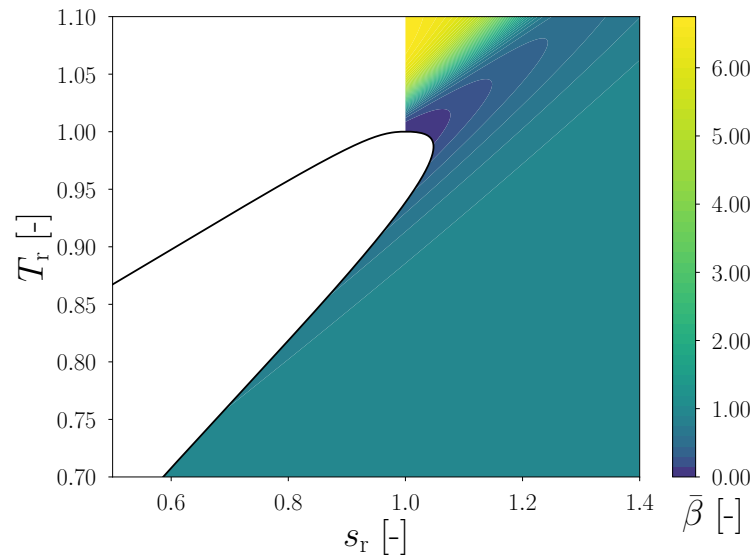


Figure 3.15: Contour plots of non-dimensional bulk modulus on the T-s thermodynamic plane for siloxane MM.

### 3.2.3. Effect of Molecular Interactions

In scientific literature on thermodynamics, the fluid compressibility factor  $Z$  is often used as a measure of non-ideality of a gas. The compressibility factor is defined such that:

$$p = Z\rho RT \quad (3.7)$$

The compressibility factor is plotted for siloxane MM as a function of reduced pressure for different values of reduced temperature in Figure 3.16. From the definition of the compressibility factor the relation between non-dimensional bulk modulus and compressibility factor can be derived:

$$\bar{\beta} = 1 + \left. \frac{1}{Z} \frac{\partial Z}{\partial \rho} \right|_T \quad (3.8)$$

The non-dimensional bulk modulus and compressibility factor are plotted together in Figure 3.17 for siloxane MM at  $T_r = 1.1$  and  $T_r = 1.3$ .

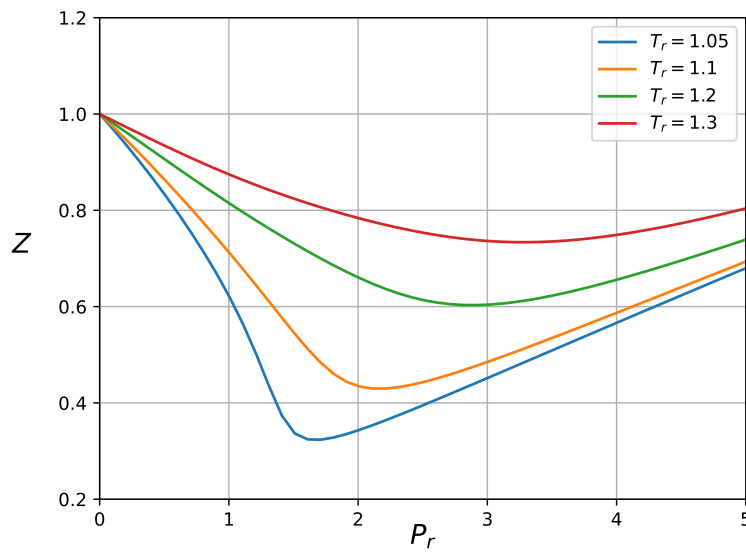


Figure 3.16: Compressibility factor as a function of reduced pressure for siloxane MM.

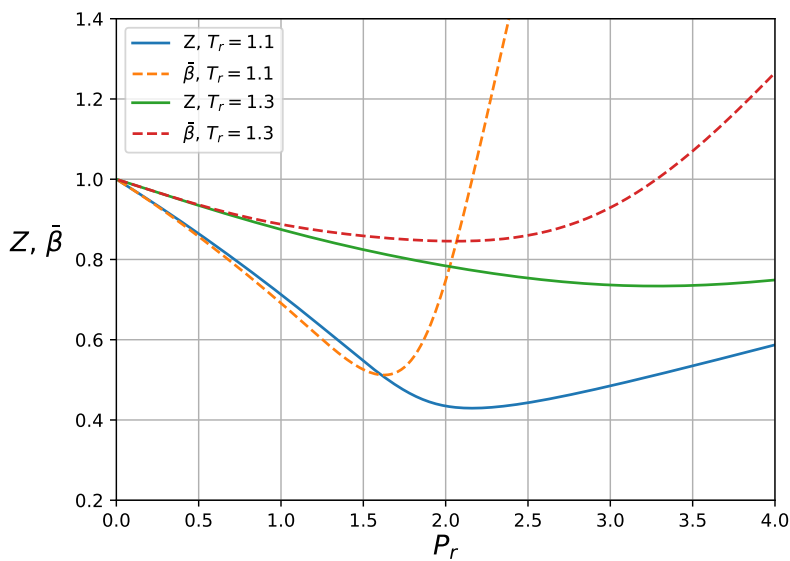


Figure 3.17: Comparison between non-dimensional bulk modulus and compressibility factor for siloxane MM.

For ideal gasses the volume of the gas molecules is negligible and there are no inter-molecular forces. In practice, this assumption becomes reasonable for gasses with increasingly low pressures ( $P_r \rightarrow 0$ ). Figure 3.17 illustrates that the compressibility factor and non-dimensional bulk modulus both equal one for this limiting case. In Figure 3.19 the qualitative behaviour of inter-molecular forces is shown as a function of distance between the molecules. Ideal gasses fit in this figure for the limit as  $R \rightarrow \infty$ . As the reduced pressure and therefore density is increased, the distance between molecules decreases and the intermolecular forces are no longer negligible causing the ideal gas assumption to break down. As shown in Figure 3.19 and schematically in Figure 3.18a the attractive forces between molecules become dominant causing both the compressibility factor and non-dimensional bulk modulus to drop below one. As the density is increased much further the volume of the gas particles becomes non-negligible relative to the volume of the gas causing repulsive forces between molecules. At a

certain value of reduced pressure for a given reduced temperature, the attractive and repulsive forces cancel out and the net inter-molecular force is zero. This corresponds to the minimum point of the compressibility factor  $Z$ . Since  $\left. \frac{\partial Z}{\partial \rho} \right|_T = 0$  at this point, Equation 3.8 states that the non-dimensional bulk modulus is equal to one. Although the ideal gas hypotheses are invalid at this point, the inter-molecular forces approximately cancel out and the non-dimensional bulk modulus has a value equal to the ideal gas value. Upon further increase of the density the repulsive forces between molecules start to dominate as illustrated schematically in Figure 3.18b causing both  $Z$  and  $\bar{\beta}$  to increase. In the limit as the reduced pressure keeps increasing the fluid will behave more and more like an incompressible medium.

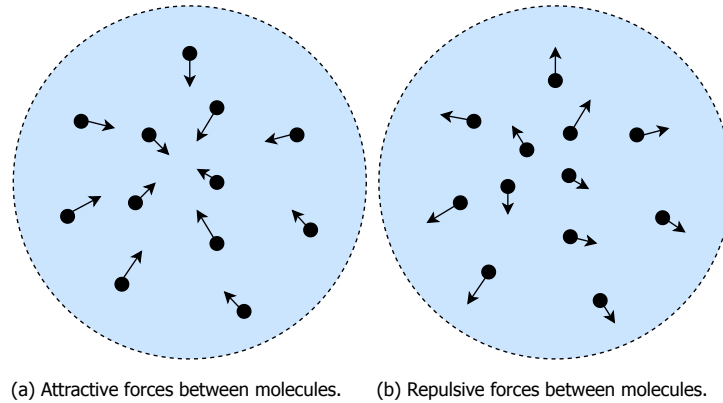


Figure 3.18: Dominant molecular interactions for different fluid regimes.

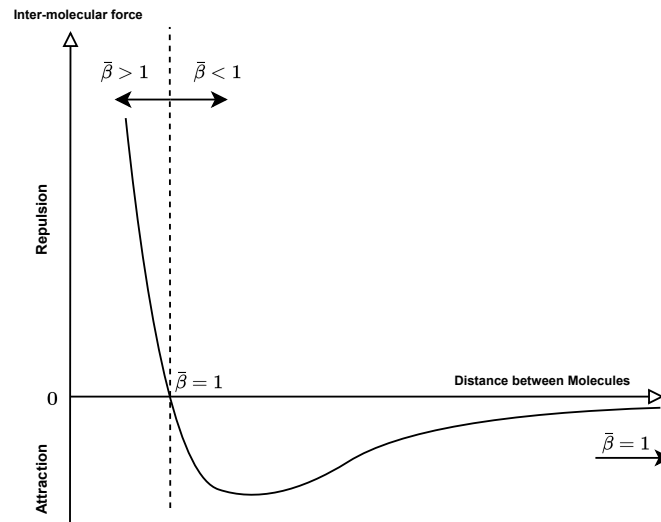


Figure 3.19: Inter-molecular forces as a function of distance between molecules.

The effect of the non-dimensional bulk modulus on the load capacity ratio can be visualized by plotting contours of the load capacity ratio on the reduced T-s thermodynamic plane as shown in Figure 3.20 for a plain journal bearing operating at  $\Lambda = 3.0$  and  $\epsilon = 0.2$  for siloxane MM. For bearings operating near the saturated vapour line, partial condensation of the gas film can occur as a result of the isothermal compression. Since the compressible Reynolds equation Equation 3.4 does not account for condensation these results have been discarded. Note that a strong reduction of load capacity is shown in the proximity of the thermodynamic critical point where the compressibility of the fluid is significant. A strong increase in load capacity is shown in the liquid-like part of the super-critical

flow regime where the fluid becomes incompressible. A strong similarity can be observed in qualitative behaviour between load capacity ratio in Figure 3.20 and non-dimensional bulk modulus in Figure 3.15.

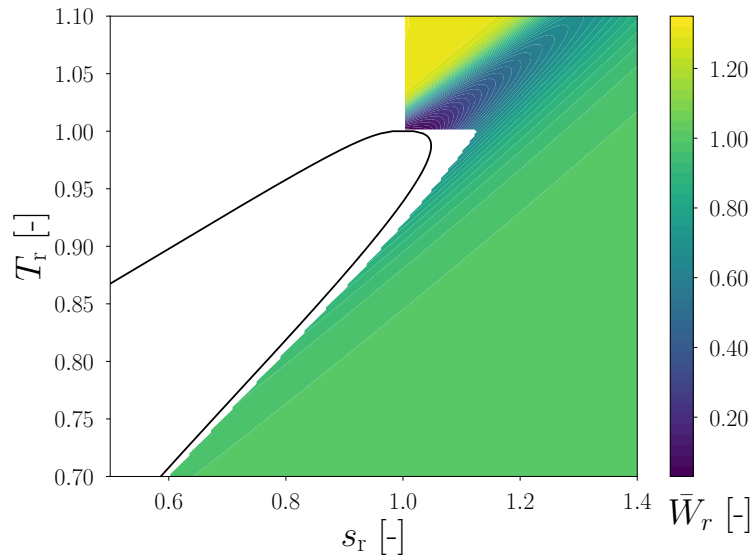
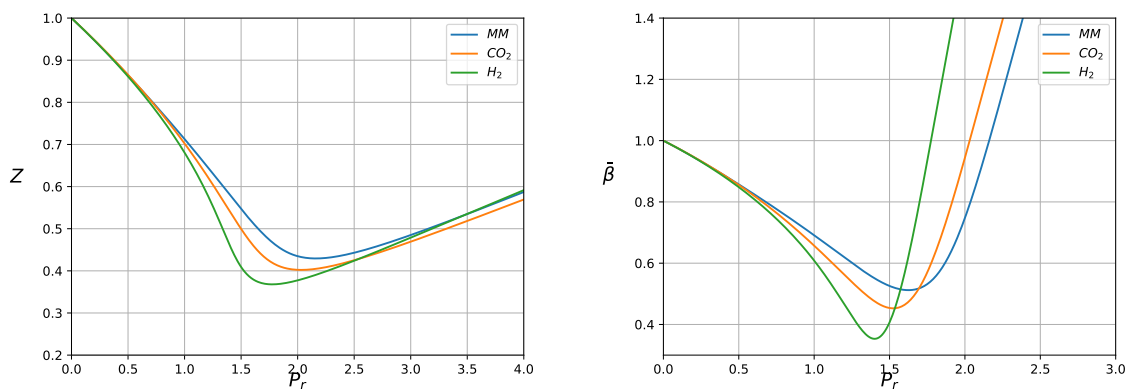


Figure 3.20: Contours of load capacity ratio on the T-s thermodynamic plane for siloxane MM with  $\epsilon = 0.2$  and  $\Lambda = 3.0$ .

### 3.2.4. Effect of Working Fluid

In Figure 3.21 the compressibility factor and non-dimensional bulk modulus are plotted for hydrogen, carbon-dioxide and siloxane MM as a function of reduced pressure for  $T_r = 1.1$ . The three fluids have different molecular complexities with siloxane having the largest molecular weight, followed by carbon dioxide and hydrogen. For larger molecular weights, the slope of the vapour saturation line in the reduced T-s plane tends to be positive, whereas it is negative for simple fluids like hydrogen as illustrated in Figure 3.22. The different molecular complexity of the fluid influences the distribution of  $\bar{\beta}$  on the reduced T-s plane as shown for hydrogen and carbon dioxide in Figure 3.23.



(a) Compressibility factor.

(b) Non-dimensional bulk modulus.

Figure 3.21: Compressibility factor and non-dimensional bulk modulus for fluids with different molecular complexities.

If the dynamic viscosity is assumed constant throughout the gas film, the non-dimensional bulk modulus is the only parameter introducing differences between working fluids. In the limit of an ideal gas, the variation of the non-dimensional bulk modulus throughout the gas film can be written as:

$$\bar{\beta} = \frac{\rho}{p_{ref}} \left. \frac{\partial p}{\partial \rho} \right|_T = \frac{\rho}{p_{ref}} RT_{ref} = \frac{\rho}{\rho_{ref}} = \bar{\rho} \quad \text{for an ideal gas} \quad (3.9)$$

Since the Reynolds equation is solved for the density field, the evaluation of the bulk modulus in the numerical procedure no longer requires the use of a fluid library and the solution is independent from the type of working fluid for a given compressibility number  $\Lambda$ .

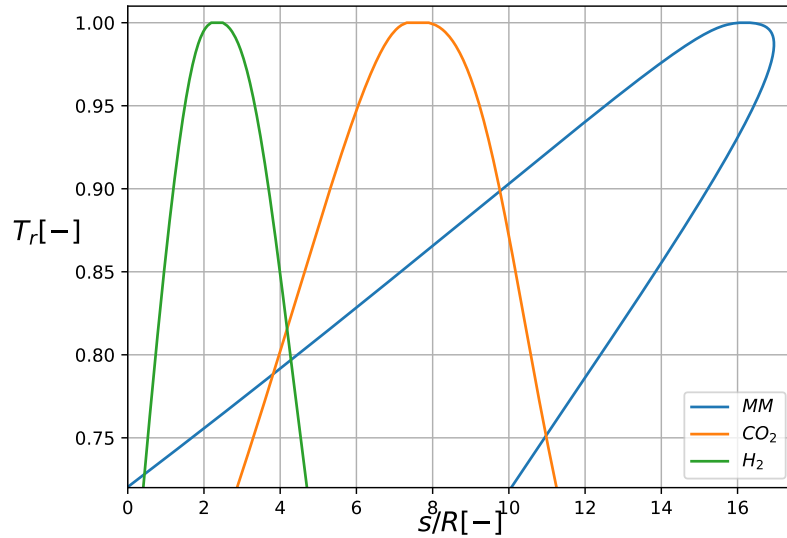
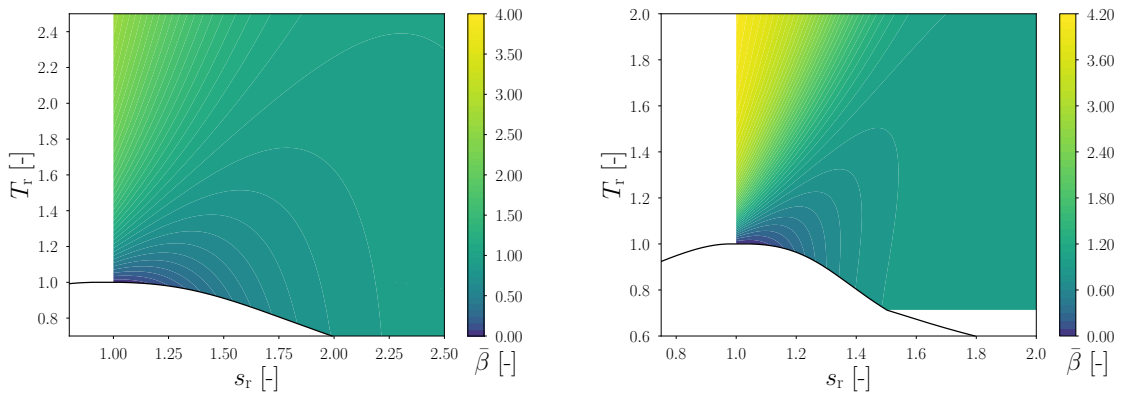


Figure 3.22: Saturation dome for fluids of different molecular complexity in the reduced T-s plane.



(a) Hydrogen.

(b) Carbon-dioxide.

Figure 3.23: Contour plots of non-dimensional bulk modulus for hydrogen and carbon-dioxide.

### 3.2.5. Effect of Bearing Width

Finally, the influence of the bearing width on the steady-state load capacity is addressed. In Figure 3.24 the non-dimensional load capacity divided by the axial width to diameter ratio is plotted for siloxane MM at  $\epsilon = 0.2$ . For increasing bearing width, this ratio asymptotically reaches a constant value. If the bearing gets narrower, however, this ratio is decreased as a result of the dominating axial leakage flow. This leakage flow is a direct result of the axial pressure gradients and is modelled within the Reynolds equation through the presence of the axial Poiseuille flow. For small values of  $L/D$ , Figure 3.24 shows

a reduction in the influence of the non-ideality of the fluid flow. The reduced peak pressures generated in compressible fluids are compensated by the reduced axial leakage flow that these peak pressures generate.

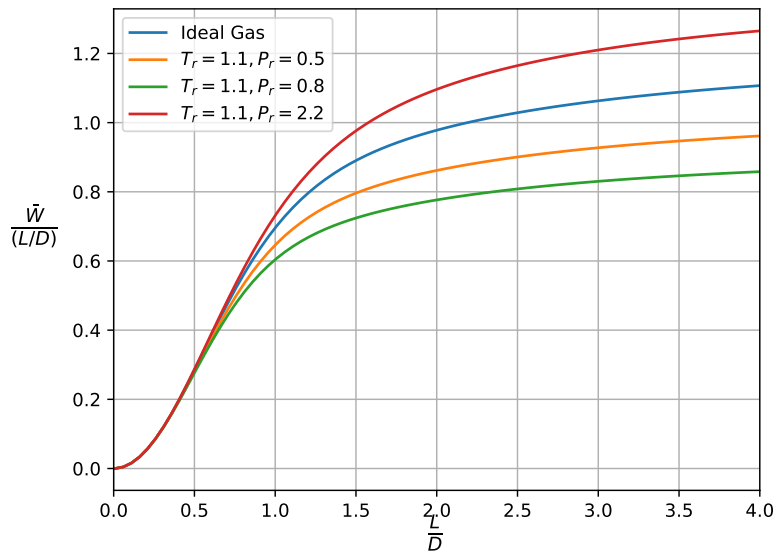


Figure 3.24: Effects of bearing width on non-dimensional load capacity.

The leakage flow caused by finite bearing widths leads to the undesirable effects of reduced load capacity and reduced stability, particularly for small bearings. Another type of rigid bearing that shows promising performance characteristics, particularly for such small-scale bearings is the herringbone grooved journal bearing as shown in Figure 3.25. [4] Within such a bearing, grooves are machined onto the surface of the rotor or bearing housing. Under the action of the driving Couette flow the fluid entrapped within the grooves cannot move exactly in the circumferential direction. Instead, it will follow the geometry of the grooves towards the centre of the bearing. In this way, the gas is effectively pumped towards the centre of the bearing leading to larger peak pressures or reduced axial leakage flows which in turn lead to an increased load capacity and bearing stability.



Figure 3.25: Herringbone grooved journal bearing of EPFL.[4]

### 3.3. Dynamic Bearing Performance

In this section, the dynamic characteristics of plain journal bearings are documented and discussed. The stiffness and damping characteristics are computed numerically with the developed software tool. The non-dimensional critical mass is used in order to analyse the non-ideal thermodynamic effects on bearing stability.

### 3.3.1. Fundamental Operating Principles

As discussed in the previous chapter, the small harmonic motions of the shaft around its equilibrium position introduce perturbations in the density and pressure field. These perturbations cause reaction forces which are introduced in the linearized rotor-dynamic equations of motion through the stiffness and damping coefficients. The schematic in Figure 3.26 shows a simplified analogy between the bearing impedances and a mechanical spring-damper system. The impedances consist of the direct stiffness and damping coefficients ( $k_{xx}, k_{yy}, c_{xx}, c_{yy}$ ) and the cross-coupled stiffness and damping coefficients ( $k_{xy}, k_{yx}, c_{xy}, c_{yx}$ ). The cross-coupled impedances are responsible for the potential occurrence of an instability which is characteristic for journal bearings.

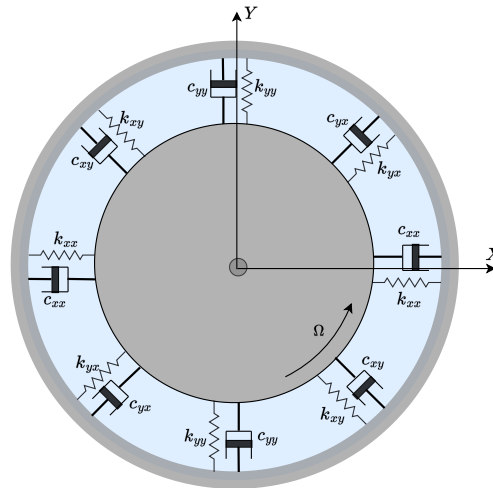


Figure 3.26: Analogy between bearing impedances and mechanical spring-damper systems.

In Figure 3.27 the bearing impedances are plotted as a function of compressibility number  $\Lambda$ . The bearing is lubricated with siloxane MM with  $P_r = 0.5$  and  $T_r = 1.1$  at  $\epsilon = 0.2$ . The direct stiffness is small in both directions for low compressibility numbers and increases with  $\Lambda$ . The magnitude of the cross-coupled stiffness increases rapidly at low compressibility numbers, reaches a maximum, and then drops again as  $\Lambda$  increases. The trends in the behaviour of the direct and cross-coupled damping coefficients are switched as compared to the stiffness coefficients.

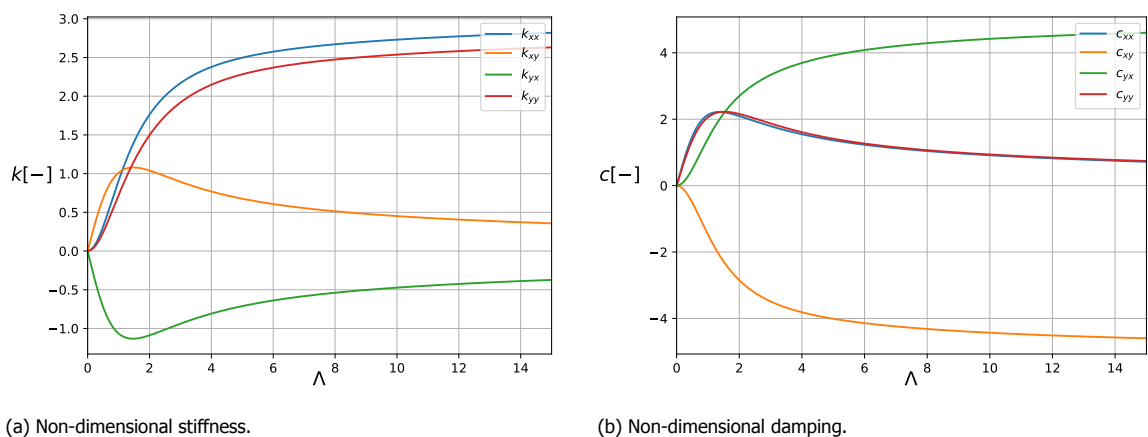


Figure 3.27: Non-dimensional stiffness and damping coefficients for a bearing lubricated with siloxane MM at  $T_r = 1.1$  and  $P_r = 0.5$  with  $\epsilon = 0.2$ .

The increase of the direct stiffness is analogous to the increase in non-dimensional load capacity as presented in the previous section. As the bearing compressibility number is increased the driving

Couette flow will generate larger peak pressures for a change in bearing position which translates into a larger bearing stiffness. The same trend is observed for the cross-coupled stiffness for low  $\Lambda$ .

The occurrence of the cross-coupled stiffness components can be explained by analysing the attitude angle of the bearing. In Figure 3.28 the attitude angle is plotted as a function of the bearing compressibility number. For small  $\Lambda$  the attitude angle reaches values of almost  $90^\circ$  whereas  $\psi$  decreases asymptotically to zero for infinitely large speed numbers. The effect of an increased attitude angle is a more asymmetrical loading condition which leads to increased cross-coupling of stiffness components.

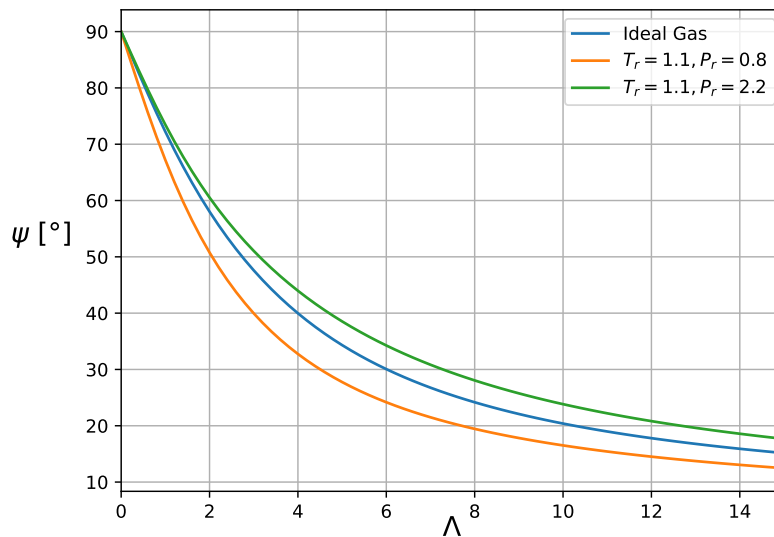


Figure 3.28: Attitude angle as a function of compressibility number for a plain journal bearing lubricated with siloxane MM at  $\epsilon = 0.2$ .

The effect of cross-coupled stiffness is shown schematically in Figure 3.29. A small perturbation of the rotor from its equilibrium position causes a reaction force in an orthogonal direction which can lead to an elliptical rotor orbit around the equilibrium eccentricity. This motion can become unstable leading to growing amplitudes of the rotor orbits. This instability is often referred to as sub-synchronous vibration or half-frequency whirl as this motion typically occurs at a frequency of about half the shaft speed.

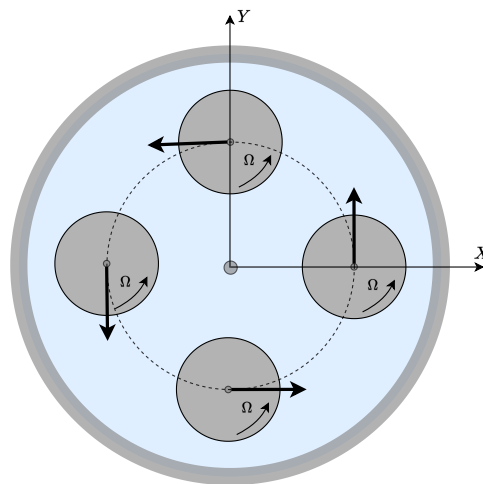


Figure 3.29: Schematic illustration of sub-synchronous whirling motions in a journal bearing.

In order to analyse the effects of non-ideal flows on bearing stability it is useful to consider the physical phenomenon responsible for large attitude angles and cross-coupled stiffness. In [Figure 3.30](#) a schematic is shown of a plain journal bearing supporting an externally applied load  $W_{ext}$ . The bearing is at an equilibrium eccentricity  $\epsilon$  and attitude angle  $\psi$  as shown in the figure. The figure illustrates two distinct regions of the gas film. Region 1 is upstream of the point of minimum film thickness and experiences a positive circumferential pressure gradient. Region 2 is downstream of the point of minimum film thickness and experiences a negative circumferential pressure gradient.

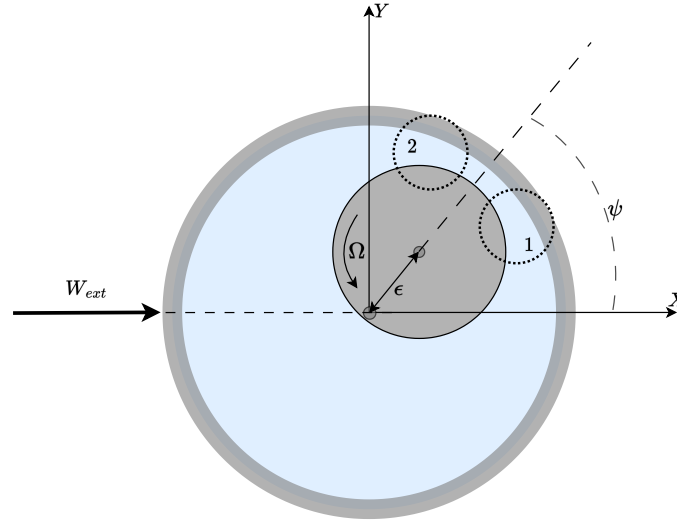


Figure 3.30: Schematic of a bearing at attitude angle  $\psi$  supporting an external load  $W_{ext}$ . Regions 1 and 2 experience positive and negative circumferential pressure gradients, respectively.

The adverse pressure gradient in region 1 causes the pressure-induced Poiseuille flow to be in the opposite direction of the driving Couette flow. In region 2 the pressure gradient is favourable and the Poiseuille and Couette flow are in the same circumferential direction. An exaggerated representation of the velocity profiles over the film thickness for both regions is shown in [Figure 3.31](#). A mean velocity over the film thickness can be defined as:

$$u_m = \frac{1}{h} \int_0^h u dy \quad (3.10)$$

And the mean velocity in region 1 will be smaller than in region 2:

$$u_{m,1} < u_{m,2} \quad (3.11)$$

If region 1 and 2 are taken at circumferential locations such that the film thicknesses are equal, conservation of mass requires the mass fluxes to be equal which in turn requires the density in region 1 to be larger than in region 2:

$$\begin{aligned} \rho_1 u_{m,1} &= \rho_2 u_{m,2} \\ \rho_1 &> \rho_2 \end{aligned} \quad (3.12)$$

The increased density causes increased pressure and an asymmetrical loading condition. The previous argument shows the connection between large attitude angles and large Poiseuille flow components. Increasing the compressibility number reduces the relative importance of the Poiseuille flow terms in the Reynolds equation and leads to smaller differences in density and pressure between region 1 and 2.

### 3.3.2. Non-dimensional Bulk Modulus & Compressibility Number

The reduced attitude angle and cross-coupled stiffness at larger bearing speed numbers are reflected in [Figure 3.32](#) which shows the non-dimensional critical mass for a bearing lubricated with siloxane MM at  $\epsilon = 0.2$ . By increasing the compressibility number the non-dimensional mass threshold for

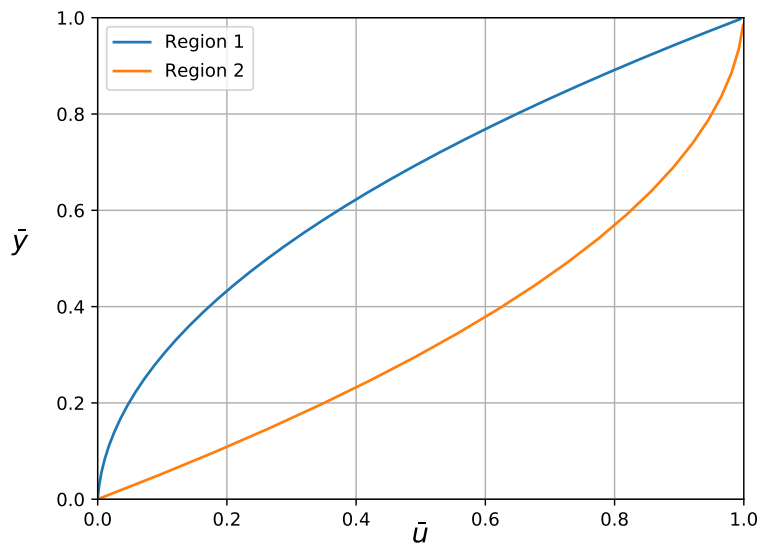


Figure 3.31: Exaggerated velocity profiles over the film thickness for region 1 and 2 corresponding to positive and negative pressure gradients.

instability increases. At infinitely large  $\Lambda$  the non-dimensional critical mass asymptotically reaches a constant value which is in agreement with the observation in Figure 3.27 where the direct stiffness and cross-coupled damping reach a plateau and the cross-coupled stiffness and direct damping reduce to near zero. The figure shows results for ideal gases as well as for non-ideal flows at  $T_r = 1.1$  with  $P_r = 0.5$ ,  $P_r = 0.8$  and  $P_r = 2.2$ . Note that the effect of the non-ideal thermodynamic state of the fluid is either to increase or decrease the bearing stability depending on the non-dimensional bulk modulus and bearing compressibility number.

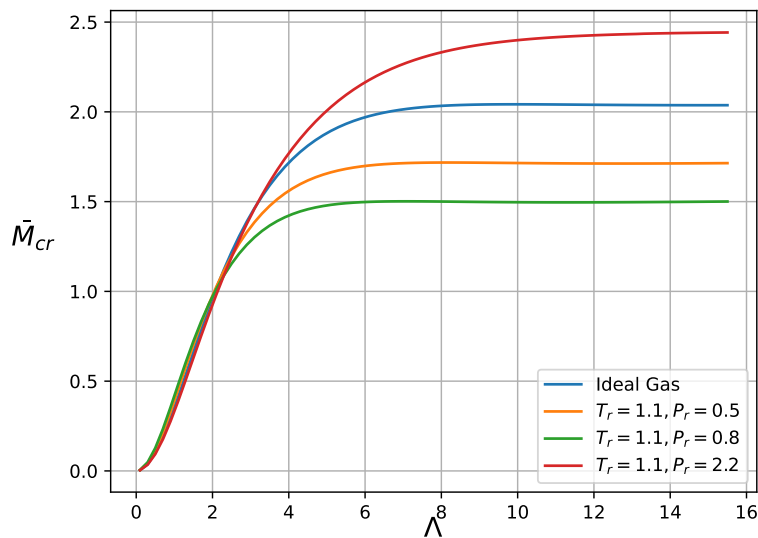


Figure 3.32: Non-dimensional critical mass as a function of bearing compressibility number at  $\epsilon = 0.2$  for a bearing lubricated with siloxane MM.

To investigate the effect of fluid compressibility the critical mass ratio is plotted in Figure 3.32 for a bearing operating in the aforementioned thermodynamic conditions. The figure shows a decreased

stability for fluids with  $\bar{\beta} < 1$  and an increased stability for fluids with  $\bar{\beta} > 1$  relative to an ideal gas for large  $\Lambda$ . Interestingly, the opposite is true for small  $\Lambda$ .

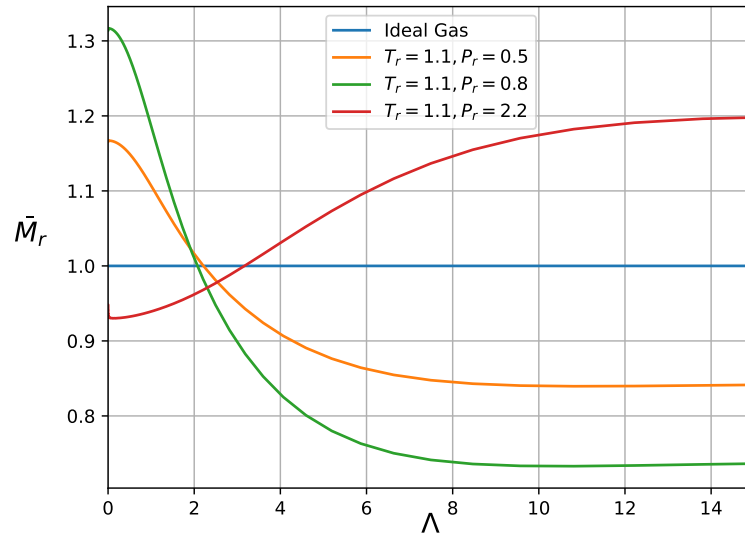


Figure 3.33: Critical mass ratio as a function of bearing compressibility number at  $\epsilon = 0.2$ .

The increased or decreased stability as a result of the compressibility of the fluid as a function of  $\Lambda$  can be explained by using the ratio of non-ideal to ideal attitude angle:

$$\bar{\psi}_r = \frac{\psi_{ng}}{\psi_{ig}} \quad (3.13)$$

The ratio of attitude angles is plotted in Figure 3.33. Note that  $\psi_r$  tends to one for infinitely large values of  $\Lambda$  which is beyond the range of values shown on the horizontal axis in the figure. The reduced attitude angle and therefore increased stability at low  $\Lambda$  for  $\bar{\beta} < 1$  can be explained using two arguments. First, the reduced values of  $\bar{\beta}$  cause a reduced significance of the Poiseuille flow term in the Reynolds equation Equation 3.4. As discussed earlier, this causes a more symmetric density field between regions upstream and downstream of the point of minimum film thickness. Furthermore, the increased compressibility of the fluid causes a lower peak pressure responsible for the asymmetry which ultimately leads to a reduced attitude angle as compared to an ideal gas with  $\bar{\beta} = 1$ .

This favourable effect of fluid compressibility fades out at large bearing speed numbers since the attitude angle naturally reduces under such conditions. The compressibility of the fluid then acts mainly to reduce the direct stiffness components causing a more unstable bearing.

Contours plots of the critical mass ratio on the reduced T-s thermodynamic plane have been created using NiceProp for two different operating conditions. In Figure 3.35a the critical mass ratio is shown for siloxane MM at  $\epsilon = 0.2$ . In Figure 3.35b the same contour plot is shown for a bearing operating at  $\Lambda = 3.0$ . The different flow regimes become apparent by comparing the figures. For  $\Lambda = 0.1$  an increased relative stability is shown for compressible fluids as a result of the Poiseuille flow dominated lubricating flow. For  $\Lambda = 3.0$  the Couette flow has become dominant and the plot shows reduced stability for increased compressibility in proximity to the thermodynamic critical point.

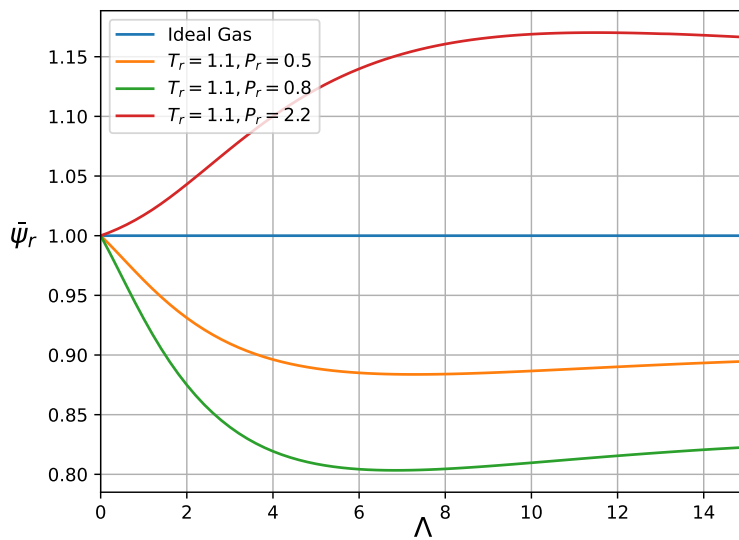
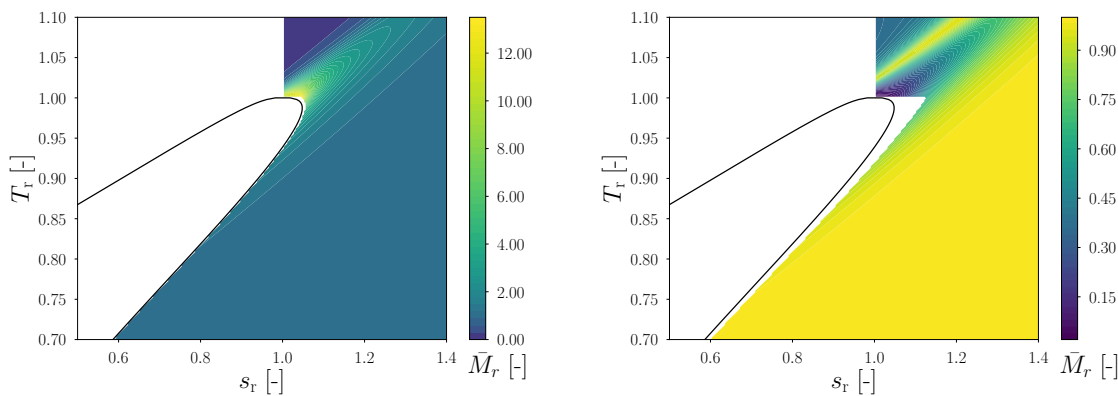


Figure 3.34: Normalized attitude angle for siloxane MM at different operating conditions with  $\epsilon = 0.2$ .



(a) Critical mass ratio for  $\Lambda = 0.1$ .

(b) Critical mass ratio for  $\Lambda = 3.0$ .

Figure 3.35: Contours of critical mass ratio on the T-s thermodynamic plane for siloxane MM with  $\epsilon = 0.2$  at  $\Lambda = 0.1$  and  $\Lambda = 3.0$ .

### 3.4. Effect of Viscosity

In the previous sections, the discussion mainly focused on the effect of the non-dimensional bulk modulus to characterize the non-ideal thermodynamic effects. The presented results assumed iso-viscous flow in which the dynamic viscosity did not vary throughout the gas film. In Equation 3.4 it can be seen, however, that the dynamic viscosity does enter the Reynolds equation. In this section, the effect of viscosity variations throughout the lubricating film will be discussed.

In order to see how the viscosity might influence the load capacity and critical mass of a bearing, the dynamic viscosity is plotted relative to the viscosity of ambient pressure air in Figure 3.36 for siloxane MM using NiceProp. It is shown that the viscosity changes are relatively modest and mostly a function of temperature in the dense gas regime but they can become significant for super-critical fluids in the liquid-like regime.

In the limiting case of an ideal gas, the dynamic viscosity is typically modelled by Sutherland’s law as shown in Equation 3.14. [32] The law is derived using kinetic theory and idealized inter-molecular force potentials. It shows that for an ideal gas, viscosity is a function of temperature only and is independent from pressure and density. It was shown in the previous section that the non-dimensional

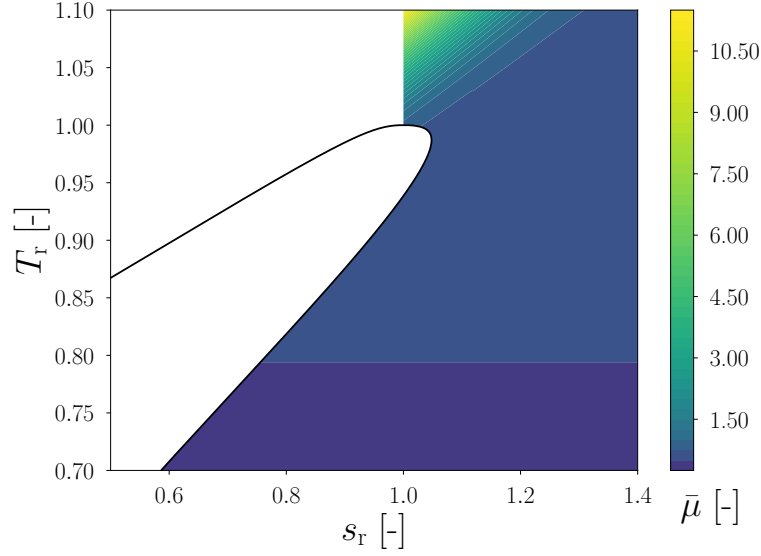


Figure 3.36: Contour plots of normalized dynamic viscosity on the T-s thermodynamic plane relative to sea level pressure air.

bulk modulus reduces to the non-dimensional density and therefore there is no dependency on the type of working fluid if the gas behaves in an ideal way. Sutherland's law implies that, for an ideal gas, the iso-thermal analysis does not model any viscosity variations throughout the gas film. The normalized dynamic viscosity will be one throughout the domain and its evaluation no longer requires the use of a fluid library. The resulting load capacity and critical mass will therefore be independent from the type of working fluid for an ideal gas and the solution of the Reynolds equation does not require the use of a thermodynamic software program.

$$\frac{\mu}{\mu_{ref}} = \left( \frac{T}{T_{ref}} \right)^{3/2} \frac{T_{ref} + S}{T + S} \quad (3.14)$$

For a non-ideal gas, the variations in viscosity should, in theory, be taken into account by using the fluid library. In practice, however, the changes in viscosity as a function of density are relatively small for the practical bearing speed numbers of interest in this research. For the effect of variations in viscosity to be significant in terms of the resulting bearing characteristics, the bearing would typically operate in the super-critical regime. Furthermore, the compressibility number  $\Lambda$  should be large in order to facilitate the iso-thermal compression required to achieve substantial viscosity gradients. It should be noted, however, that under these conditions the assumption of negligible thermal expansion in the thin film as presented in [section 2.2](#) might not hold.

### 3.5. Turbulence Effects

In the analysis presented in the previous sections, the thin film flow was assumed to be laminar. However, the regions where flow non-ideality becomes relevant are typically characterized by high densities and pressures. Furthermore, some fluids of interest can have low values of viscosity. NASA has performed experimental research on the power losses in gas foil bearings operating at increased pressures. [18] The experiments show that at increased pressures the inertia of the flow is no longer negligible relative to the viscous shear stresses. The fluid inertia can cause transition to occur in the gas film, ultimately leading to turbulent flow. In this section, the effects of fluid inertia are considered by introducing the turbulence correction factors into the solution of the Reynolds equation. The effects of varying Reynolds number on bearing load capacity and critical mass is discussed. Finally, the connection between flow non-ideality and turbulence in plain journal bearings is addressed.

In order to investigate the effect of different Reynolds numbers, the ambient Reynolds number based on the rotor rotational speed  $\Omega$  and nominal bearing clearance  $h_0$  is recalled:

$$Re = \frac{\rho_{ref} \Omega R h_0}{\mu_{ref}} \quad (3.15)$$

Note that the local Reynolds number can vary throughout the gas film since properties such as the film thickness, density and viscosity can change.

### 3.5.1. Effect on Steady-State Characteristics

In [Figure 3.37](#) the non-dimensional load capacity is shown for a bearing lubricated with siloxane MM at  $P_r = 0.5$  and  $T_r = 1.1$ . Results are plotted for laminar flow and for turbulent flow at  $Re = 5000$  and  $Re = 15000$ . The figure shows an increased load capacity at low bearing compressibility numbers as a result of the turbulent flows. For larger Reynolds numbers the increase becomes more significant. As the bearing speed number increases the effects of Reynolds number on load capacity diminishes and in the limit for very large  $\Lambda$  the laminar and turbulent solutions approach the same constant value.

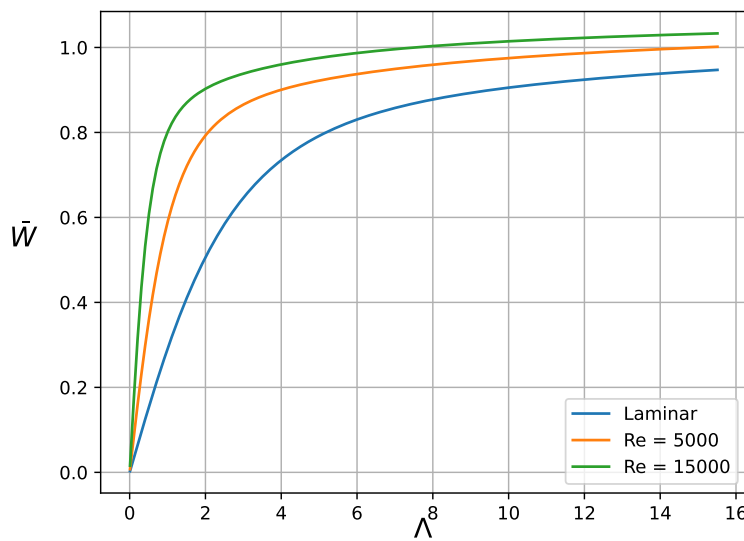


Figure 3.37: Non-dimensional load capacity for siloxane MM at  $T_r = 1.1$  and  $P_r = 0.5$  with  $\epsilon = 0.2$  for various ambient Reynolds numbers.

The effect of turbulence on the Reynolds equation can be explained by reference to [Equation 3.4](#). The turbulence correction factors  $G_{0x}$  and  $G_{0z}$  appear in the circumferential and axial Poiseuille flow terms respectively. Note that according to [Equation 2.42](#) and [Equation 2.43](#) the turbulence correction factors will have values smaller than one. Consequently, the effect of turbulent flow in the Reynolds equation is to decrease the significance of the Poiseuille flow terms. Turbulence effects in the Reynolds equation, therefore, seem to have a similar effect as the bearing speed number  $\Lambda$  and decreases in the non-dimensional bulk modulus as discussed in the previous sections.

The effects of turbulence on the Reynolds equation can be explained by reference to [Figure 3.38](#). The figure shows the qualitative shapes of the velocity profiles for laminar and turbulent Poiseuille and Couette flows. The effect of the turbulent fluctuations in the flow is to transport kinetic energy to the walls. This leads to increased velocity gradients and wall shear stresses as indicated in the figure. Similar to the previous section, a mean velocity over the film thickness can be defined as:

$$u_m = \frac{1}{h} \int_0^h u dy \quad (3.16)$$

For pure Couette flow it can be shown that this mean velocity over the film thickness is equal for laminar and turbulent flow:

$$u_{m,turb} = u_{m,lam} \quad (3.17)$$

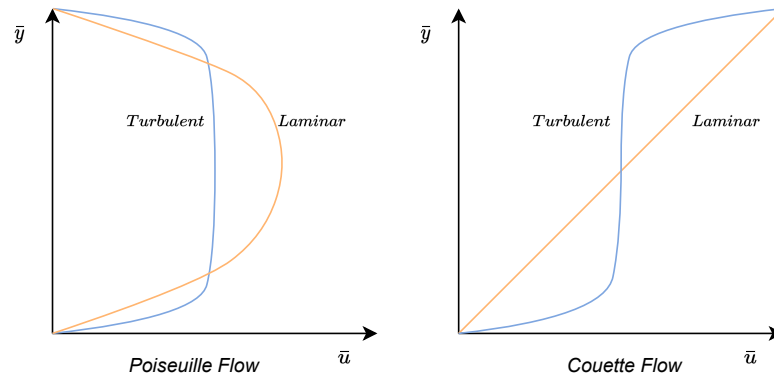


Figure 3.38: Qualitative shapes of the velocity profiles for laminar and turbulent Poiseuille and Couette flow.

For pure Poiseuille flow, however, the turbulence effectively acts as an increased viscosity leading to more resistance to pressure induced flow. The result is a decreased mean velocity for Poiseuille flow:

$$u_{m,turb} < u_{m,lam} \quad (3.18)$$

Within the Reynolds equation, the driving Couette flow therefore becomes increasingly dominant for increased Reynolds numbers. This in turn leads to larger peak density and pressures generated within the gas film with an increased load capacity as indicated in Figure 3.37 as a result. Since the Poiseuille flow terms within the Reynolds equation naturally become less significant at large  $\Lambda$ , the effect of turbulence at a given Reynolds number for larger bearing compressibility numbers becomes less important. Note, however, that increasing the bearing compressibility number in practice typically means operating the bearing at a larger rotational speed which will also increase the ambient Reynolds number.

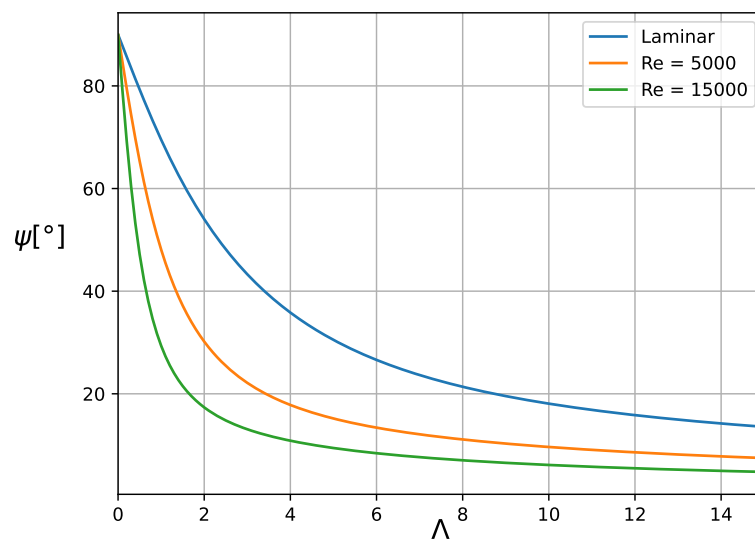


Figure 3.39: Attitude angle for siloxane MM at  $T_r = 1.1$  and  $P_r = 0.5$  with  $\epsilon = 0.2$  for various ambient Reynolds numbers.

### 3.5.2. Effect on Dynamic Characteristics

In Figure 3.39 the attitude angle is plotted for the laminar and turbulent flow cases. The figure shows a significant decrease in attitude angle for moderate values of  $\Lambda$  which is in agreement with the discussion of the previous sections where the reduction in attitude angle was linked to a reduced pressure flow.

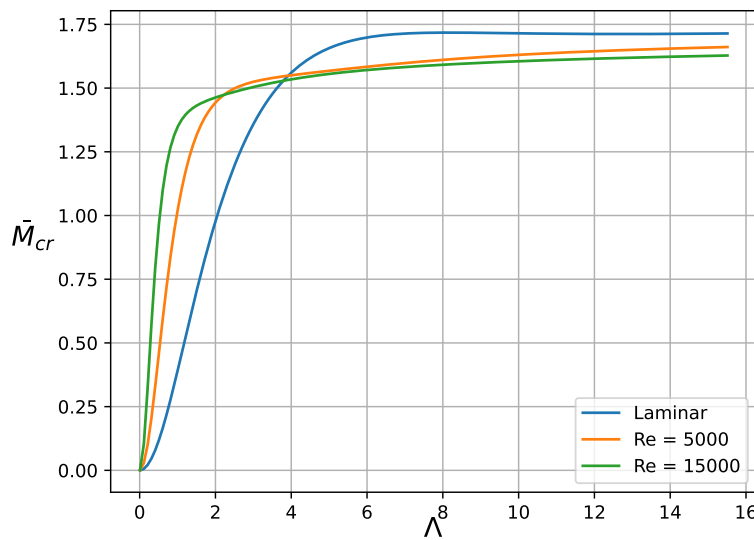
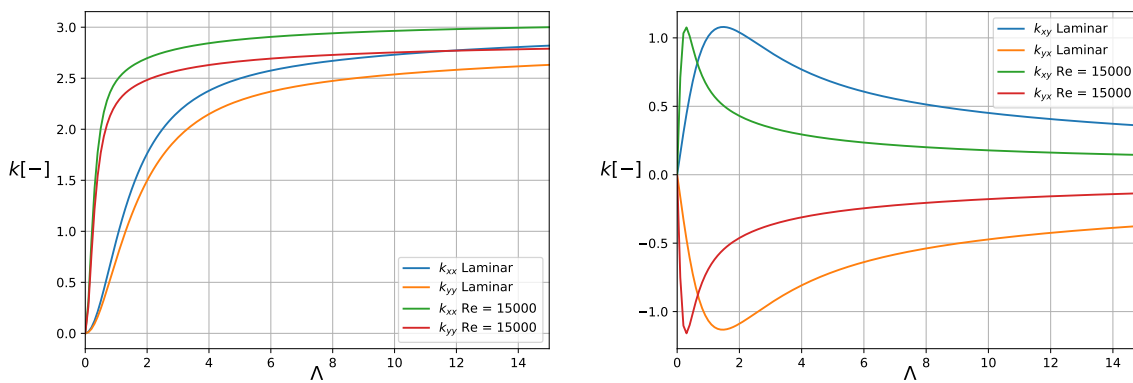


Figure 3.40: Non-dimensional critical mass for siloxane MM at  $T_r = 1.1$  and  $P_r = 0.5$  with  $\epsilon = 0.2$  for various ambient Reynolds numbers.

The effect of turbulent flows on bearing stability is analysed by reference to the non-dimensional critical mass in Figure 3.32. The results are plotted again for siloxane MM at  $T_r = 1.1$  and  $P_r = 0.5$  for  $\epsilon = 0.2$ . An increased stability is shown for low values of  $\Lambda$  whereas the stability is reduced as compared to laminar flows for large  $\Lambda$ .



(a) Non-dimensional direct stiffness.

(b) Non-dimensional cross-coupled stiffness.

Figure 3.41: Non-dimensional direct and cross-coupled stiffness coefficients for a bearing lubricated with siloxane MM at  $T_r = 1.1$  and  $P_r = 0.5$  with  $\epsilon = 0.2$  at various Reynolds numbers.

In order to conceptualize the effects of turbulence on bearing stability the stiffness and damping coefficients are plotted for laminar and turbulent flows. The stiffness coefficients are compared in Figure 3.41 and the damping coefficients are shown in Figure 3.42. The figures show that the direct stiffness coefficients are larger for turbulent flows at low  $\Lambda$  and asymptotically reach equal values for large  $\Lambda$ . This trend is analogous to the trend of non-dimensional load capacity as discussed earlier. The cross-coupled stiffness coefficients peak at lower bearing speed numbers for turbulent flows. As  $\Lambda$  increases after this peak, the turbulent flows show smaller cross-coupling between the two orthogonal directions which might explain the increased stability observed in Figure 3.40 for low speed numbers.

The plots of non-dimensional damping coefficient indicate a quicker rise of both direct and cross-

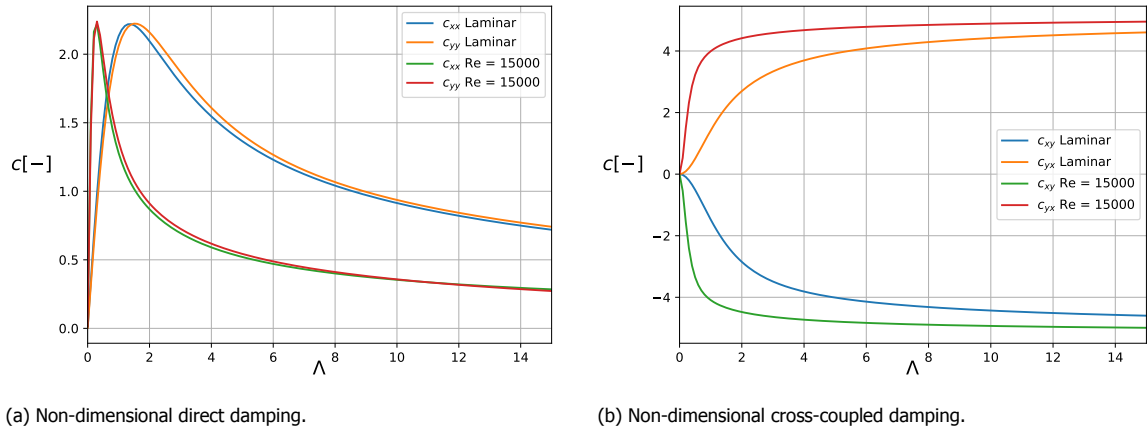


Figure 3.42: Non-dimensional direct and cross-coupled damping coefficients for a bearing lubricated with siloxane MM at  $T_r = 1.1$  and  $P_r = 0.5$  with  $\epsilon = 0.2$  at various Reynolds numbers.

coupled damping coefficients at small bearing speed numbers. The direct damping coefficients peak at relatively low  $\Lambda$  and are significantly smaller for turbulent flows as  $\Lambda$  increases to moderate values. Furthermore, the cross-coupled damping coefficients seem to be slightly larger in magnitude for larger Reynolds numbers. Since the cross-coupled damping coefficients seem to have a detrimental effect and the direct damping a beneficial effect in terms of stability this might explain the reduced critical mass in Figure 3.40 for moderately increased compressibility numbers.

### 3.5.3. Connection with Non-Ideal Thermodynamic Effects

The connection between turbulence and non-ideal thermodynamic effects is shown in Figure 3.43. Similar results have first been presented for R134a at comparable conditions by Guenat.[11] The plots show a stronger decrease in load capacity and critical mass ratios at low compressibility numbers for turbulent flows. This trend can again be explained by the larger pressure flows for low Reynolds numbers leading to a smoother density and pressure field. Larger variations and increased peak densities for turbulent flows will introduce the effect of flow non-ideality in a more significant way as indicated in the figures.

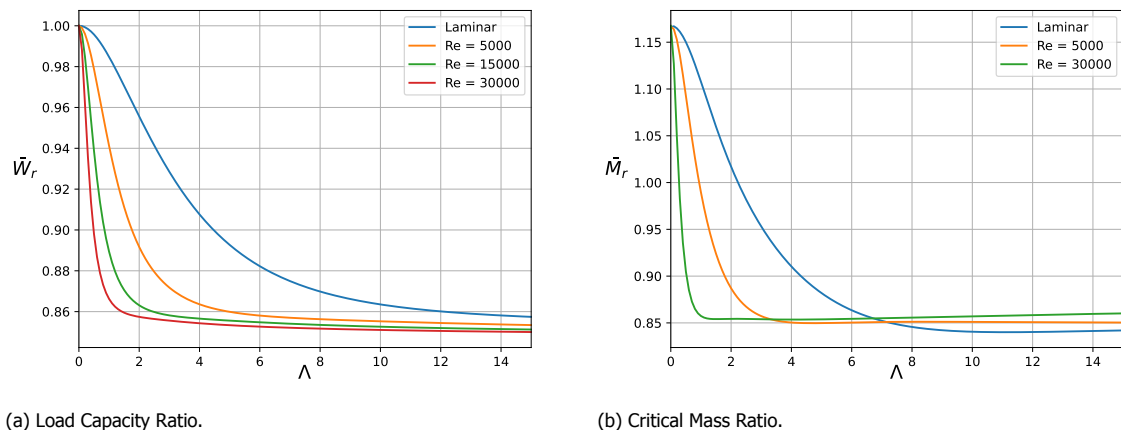


Figure 3.43: Load capacity and critical mass ratios for a bearing lubricated with siloxane MM at  $T_r = 1.1$  and  $P_r = 0.5$  with  $\epsilon = 0.2$  at various Reynolds numbers.

The contours of load capacity and critical mass ratios for turbulent flow at  $Re = 15000$  are plotted on the reduced T-s thermodynamic plane in Figure 3.44. Comparing these figures to the same plots of a laminar flow bearing operating at similar conditions in Figure 3.20 and Figure 3.35b it is observed that

both load capacity and critical mass ratios deviate from unity more significantly, indicating the more pronounced effect of non-ideal flows in turbulent flow lubrication.

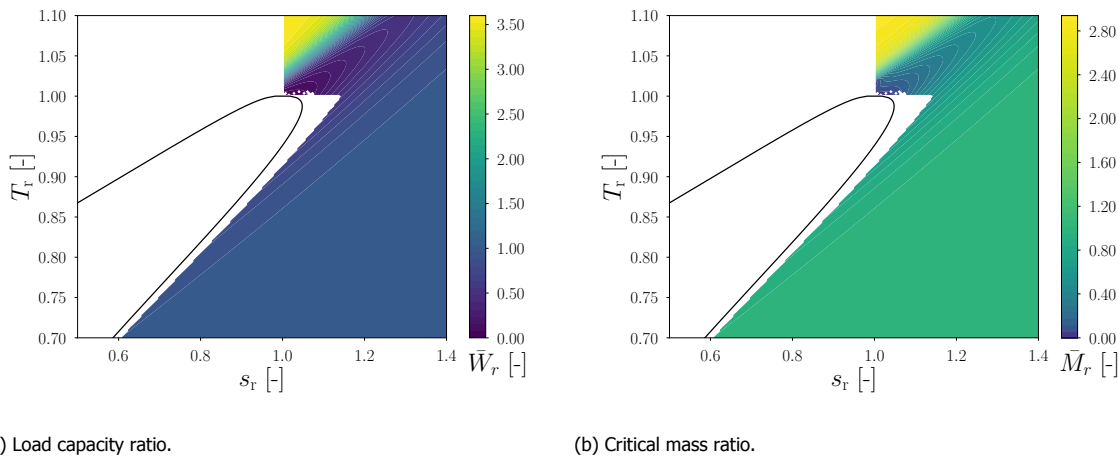


Figure 3.44: Contours of load capacity and critical mass ratio on the reduced T-s thermodynamic plane for siloxane MM with  $\epsilon = 0.2$  and  $\Lambda = 3.0$  for turbulent flow at  $Re = 15000$ .

### 3.6. Chapter Conclusion

In this chapter, the performance characteristics of rigid gas bearings have been considered. The numerical solver was verified using openly available data from scientific literature. The impact of non-ideal thermodynamic effects on the non-dimensional load capacity and critical mass of plain journal bearings was discussed.

The non-ideal thermodynamic effects affect bearing performance mainly through the non-dimensional bulk modulus. Compressible flows in the dense gas regime or near the thermodynamic critical point typically have a non-dimensional bulk modulus smaller than one whereas super-critical fluids in the liquid-like regime can have values larger than one. In the limit of an ideal gas, the non-dimensional bulk modulus becomes exactly equal to one. Values of the non-dimensional bulk modulus smaller than one typically act to reduce the load capacity as compared to ideal gasses. The same is true for the critical mass parameter at large compressibility numbers. Dynamic viscosity is shown to have limited influence when it comes to introducing non-ideal thermodynamic effects in thin films.

For high-pressure gasses, the thin lubrication film can become turbulent. Increased Reynolds numbers are shown to increase the non-dimensional load capacity at low bearing numbers. The stability of the bearing is either increased or decreased depending on whether the compressibility number is small or large. Turbulence has the tendency to increase the significance of non-ideal thermodynamic effects in thin film flows.



# 4

## Results for Gas Foil Bearings

For practical applications, plain journal bearings typically lack sufficient stability and load capacity for reliable operation. Compliant foundations as used in gas foil bearings can be designed to significantly increase the bearing load capacity and stability.[9] In order to tailor the stiffness of the bump foil structure as done in second or third-generation gas foil bearings a numerical tool capturing the relevant fluid-structure interaction would be useful. In this chapter, the numerical model for gas foil bearings as discussed in [chapter 2](#) is verified. Furthermore, the characteristics of the compliant bearings such as load capacity and attitude angle will be analysed and compared to plain journal bearings. The current work focuses on the analysis of so-called first-generation gas foil bearings in which the bump foil stiffness is uniform in both axial and circumferential directions. Up till now, the analysis has been done using non-dimensional numbers which allowed for conceptual understanding of the ongoing physical phenomena. In the final section of this chapter, the dimensional load capacity will be computed for gas foil bearings of suitable dimensions for operation with the laboratory mini-ORC turbine of the ORCHID facility of the TU Delft.

### 4.1. Verification

The simple elastic foundation model of the compliant bump foil will be verified by comparison with data from scientific literature. In particular, the work of Kim and San Andrés is used as a reference.[5] In their work a heavily loaded gas foil bearing operating with ambient pressure air is simulated. Results of the static load are plotted versus the minimum film thickness, attitude angle and journal eccentricity. For the dynamic bearing characteristics the stiffness and damping coefficients are plotted as a function of excitation frequency. Kim and San Andrés have validated their data using experimental test results.

The steady-state bearing characteristics are calculated first using the developed numerical model. The results are plotted along with the reference data in [Figure 4.1](#). The figures show the dimensional journal eccentricity, attitude angle and minimum film thickness plotted against the load capacity. The dimensions and operating conditions of the gas foil bearing under consideration are summarized in [Table 4.1](#).

Parameter	Value
Bearing Radius, $R$	19.05 mm
Bearing Width, $L$	38.1 mm
Nominal Bearing Clearance, $h_0$	31.8 $\mu\text{m}$
Compliance Ratio, $S$	0.67
Rotational Speed, $\Omega$	30000 RPM
Loss Coefficient, $\gamma_S$	0.0

Table 4.1: Bearing parameters used in the work of Kim and San Andrés. [5]

The figures show an increasing bearing load capacity for an increasing journal eccentricity as was also observed for plain journal bearings in the previous chapter. Note that the journal eccentricity

is increased significantly beyond the nominal bearing clearance indicating that the bearing is heavily loaded. Increasing the eccentricity beyond the nominal bearing clearance is possible only if the bump foil deflections are large enough to avoid physical contact. In order to compute the density and pressure field within the gas film of a bearing operating at such conditions it was found that the relaxation factor in the Gauss-Seidel iterative method had to be reduced to  $\kappa \approx 0.1$  in order for the solution to converge. In particular, during the first iterations of the numerical procedure, under-estimation of the pressure in the minimum film thickness region can lead to under-estimation of the structural deflections. This in turn causes the calculated local film thickness to be negative leading to divergence of the solution. Proper initialization of the density field along with sufficient under-relaxation has shown to solve the issue.

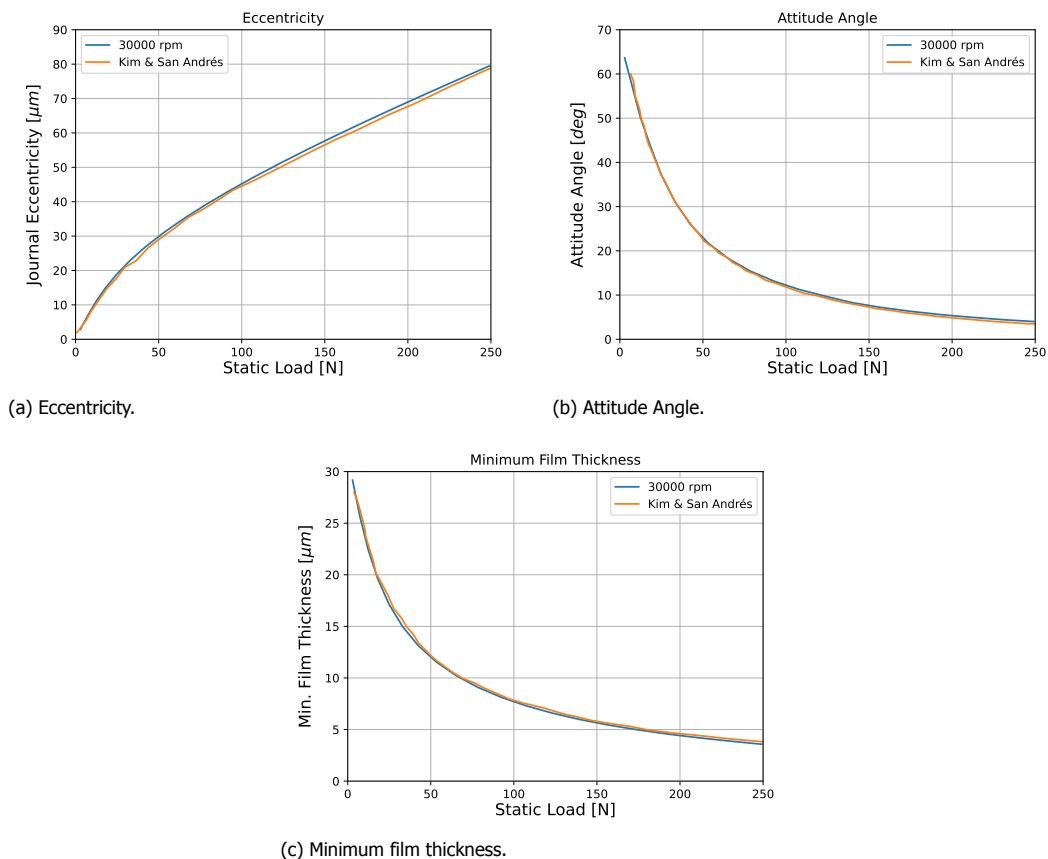
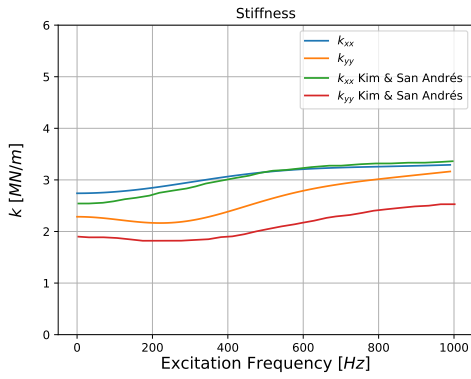


Figure 4.1: Verification of the eccentricity, attitude angle and minimum film thickness versus load capacity for a gas foil journal bearing.

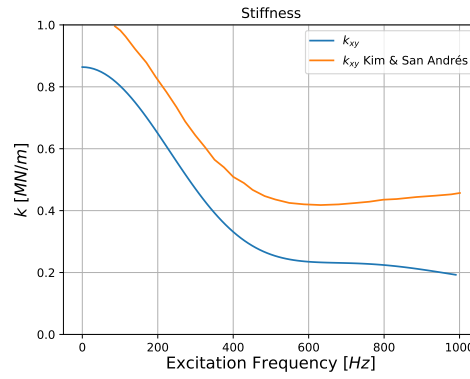
As the static load and the eccentricity increase, the attitude angle decreases as shown in [Figure 4.1b](#). The minimum film thickness also decreases with increasing bearing loading as a larger aerodynamic wedge is required to generate sufficient pressure ([Figure 4.1c](#)). The results obtained using the developed computational tool seem to agree well with the computational results presented by Kim and San Andrés for the steady-state performance.

Finally, the computed dynamic characteristics of the bearing will be compared to the reference data. In order to do so, the steady state eccentricity, attitude angle and pressure field are first obtained for a gas foil bearing supporting a 50N static load using the Newton-Raphson method discussed in [chapter 2](#). The bearing impedances can then be computed as a function of the excitation frequency. The resulting direct and cross-coupled stiffness coefficients are plotted in [Figure 4.2](#). The direct damping coefficients are plotted in [Figure 4.3](#). Note that both the computed stiffness and damping coefficients do not completely agree with the reference data. The direct stiffness is slightly overestimated by the developed tool. In contrast, the cross-coupled stiffness is underestimated.

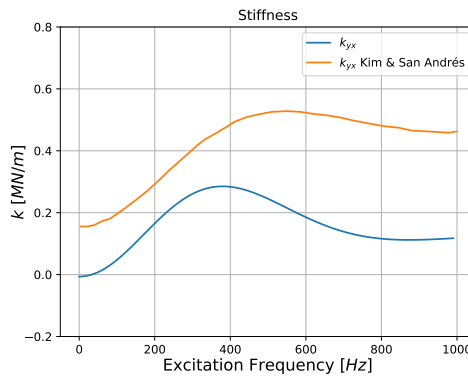
Although the exact numerical values of the computed impedances do not fully match with the



(a) Direct stiffness coefficients.



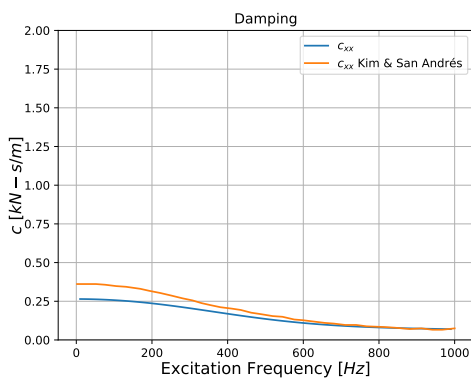
(b) Cross-coupled  $k_{xy}$  coefficient.



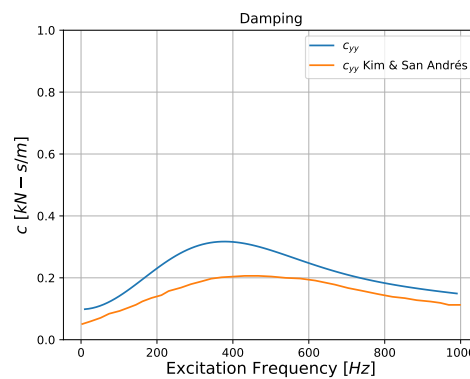
(c) Cross-coupled  $k_{yx}$  coefficient.

Figure 4.2: Verification of the direct and cross-coupled dimensional stiffness coefficients.

reference data, the qualitative patterns of the behaviour of the impedances as a function of excitation frequency are very similar. The error is likely caused by a bug in the code. Within this chapter, the statements made on the dynamical characteristics such as stiffness, damping and the critical mass will therefore only be qualitative. For further quantitative analysis of dynamical aspects related to gas foil bearings the software model requires improvement. The steady-state characteristics, however, seem to match well with the data provided by Kim and San Andrés and the results related to the load capacity or attitude angle as discussed in this chapter can be considered more accurate.



(a) Direct  $c_{xx}$  coefficient.



(b) Direct  $c_{yy}$  coefficient.

Figure 4.3: Verification of the direct damping coefficients.

## 4.2. Analysis of Gas Foil Bearings

The performance characteristics of gas foil bearings are compared to plain journal bearings at similar operating conditions in this section. The presented results are under the assumption of laminar flow. The bearings are lubricated with siloxane MM with the ambient fluid in the bearing compartment at a reduced pressure and temperature of  $P_r = 0.8$  and  $T_r = 1.1$ , respectively.

### 4.2.1. Load Capacity

In the previous chapter, plain journal bearings operating at different ambient thermodynamic conditions were compared by enforcing equal eccentricity ratio. For gas foil bearings, however, the bump foil structure deforms allowing for eccentricity ratios larger than one at heavily loaded conditions. In order to compare the results with rigid bearings, operation at equal minimum film thickness is considered instead of equal eccentricity. A plot showing the dimensional load capacity as a function of minimum film thickness is shown in Figure 4.4. The gas foil bearing has a compliance ratio of  $S = 0.4$ . This compliance ratio was defined in chapter 2 as the ratio of the reference pressure to the product of nominal bearing clearance  $h_0$  and bump foil stiffness per unit area  $K_f$ . The local structural deflection can then be calculated using the pressure difference between the gas film and the fluid underneath the top foil:

$$\bar{w}_d = S\delta\bar{p} \approx S \left. \frac{\partial \bar{p}}{\partial \bar{\rho}} \right|_T (\bar{\rho} - 1) \quad (4.1)$$

In chapter 2 it was stated that the compliance ratio defines the ratio of the stiffness of the fluid to the stiffness of the structure. Furthermore, in chapter 3 the bulk modulus was presented as a measure of the stiffness of the fluid. Then from the above equation and the definition of the compliance ratio the following relation holds:

$$S \left. \frac{\partial \bar{p}}{\partial \bar{\rho}} \right|_T = \frac{p_{ref}}{h_0 K_f} \left. \frac{\partial \bar{p}}{\partial \bar{\rho}} \right|_T = \frac{\rho_{ref}}{h_0 K_f} \left. \frac{\partial p}{\partial \rho} \right|_T \quad (4.2)$$

The final term in the equation above shows that the compliance ratio is connected to the bulk modulus. This justifies the interpretation of this parameter as a ratio of fluid stiffness to structural stiffness. For ideal gasses, the bulk modulus and thus the fluid stiffness reduces to the pressure of the gas.

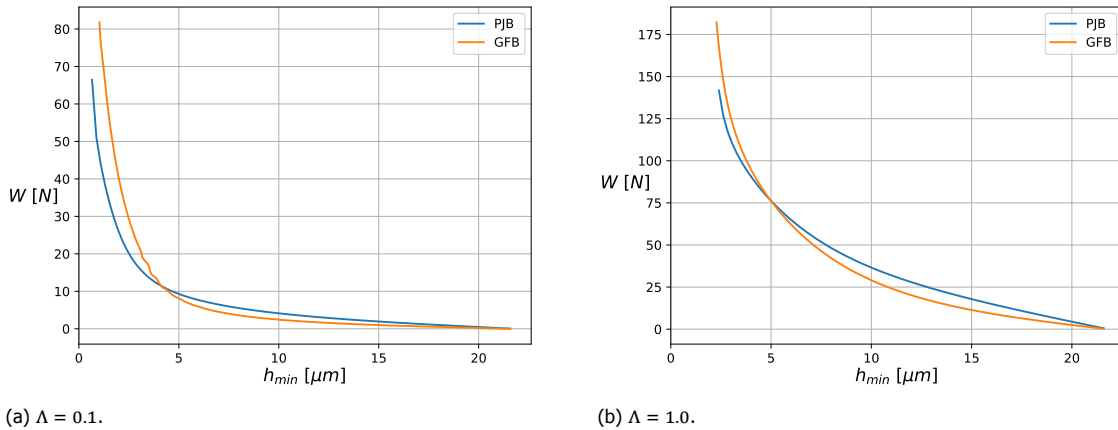


Figure 4.4: Dimensional load capacity as a function of minimum film thickness for a gas foil bearing (GFB) and a plain journal bearing (PJB) at  $\Lambda = 0.1$  and  $\Lambda = 1.0$  for a nominal film thickness of  $h_0 = 21.8 \mu\text{m}$ .

For plain journal bearings, the surface is infinitely stiff and therefore the compliance ratio is zero. The behaviour of both bearing types is shown in the figures. The load capacity increases as the eccentricity is increased from zero and the minimum film thickness is accordingly reduced from the nominal value of  $h_0 = 21.8 \mu\text{m}$ . The figures show that this increase is slightly more pronounced for plain journal bearings upon initial decrease of the minimum film thickness. As the eccentricity is increased further,

the load capacity increases non-linearly. The deflection of the bump foils allows the gas foil bearing to reach larger eccentricities for the same value of the minimum film thickness. Figure 4.4 shows a slightly larger load capacity for the gas foil bearing as the minimum film thickness gets small. Another way to interpret the plots is by stating that the gas foil bearing can generate the same load capacity at a larger minimum film thickness for highly loaded conditions. A larger minimum film thickness will in turn lead to smaller power losses for example.

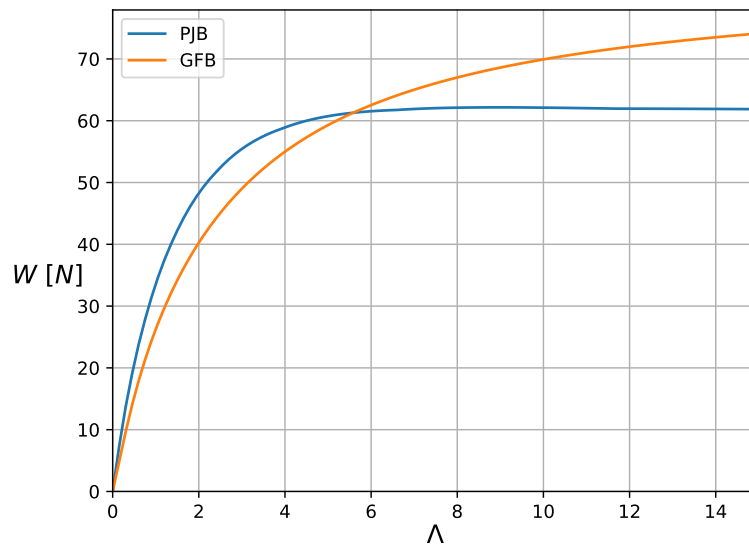


Figure 4.5: Dimensional load capacity as a function of bearing speed number  $\Lambda$  for a PJB and a GFB.

The bearing load capacity is plotted as a function of the compressibility number for a PJB and a GFB in Figure 4.5. The gas foil bearing is operating at an eccentricity of  $\epsilon = 0.6$ . The eccentricity of the plain journal bearing is such to create an equal minimum film thickness. The plot shows a slightly larger load capacity at low rotational speeds for the PJB. As the rotational speed or compressibility number increases, larger pressures are generated in the gas films which ultimately results in a slight advantage in terms of load capacity for the GFB.

Overall, the plots in Figure 4.4 and Figure 4.5 show that the rigid gas bearing and the first-generation gas foil bearing exhibit approximately equal load capacities. This conclusion is in agreement with the findings in scientific literature.[9] Furthermore, this indicates the necessity of tailoring the bump foil stiffness to really benefit from the potential performance increase that gas foil bearings have to offer. In a second-generation gas foil bearing, for example, the stiffness can be varied in axial direction such as to reduce the fluid leakage from the foil edges. According to literature, this could approximately double the load capacity as compared to first-generation gas foil bearings.[9] These effects can be captured by the Reynolds equation through the reduced axial Poiseuille flow as discussed in chapter 3. Further analysis of gas foil bearings with enhanced bump foil structures is, however, beyond the scope of the current work.

#### 4.2.2. Attitude Angle and Stability

The steady-state attitude angle is plotted as a function of the compressibility number in Figure 4.6. Both the rigid and the compliant bearing show a decrease in attitude angle with  $\Lambda$ . At low bearing speed numbers, however, the gas foil bearing shows significantly lower attitude angles. In the previous chapter, the attitude angle was linked to the effect of the Poiseuille flow on the pressure distribution. Upstream of the point of minimum film thickness, an increased pressure is observed and a reduced pressure is observed downstream of the minimum film thickness. For a gas foil bearing the increased pressure upstream will increase the foil deflection, leading to a larger local film thickness. This will in turn lead to a smaller pressure locally as compared to a rigid bearing. The opposite effect occurs downstream of the minimum film thickness. This redistribution of the film thickness through foil

deflections in a gas foil bearing causes the effect of the Poiseuille flow to be less significant compared to rigid bearings which leads to smaller attitude angles.

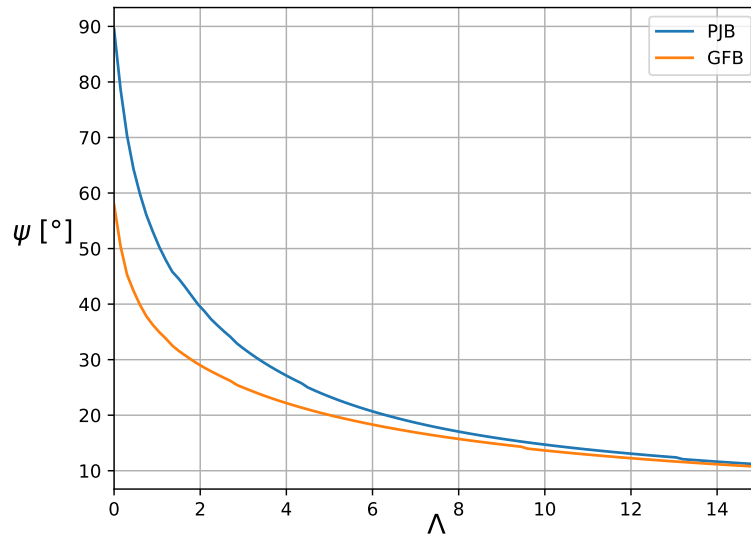


Figure 4.6: Attitude angle as a function of bearing speed number  $\Delta$  for a PJB and a GFB.

The overall reduction of attitude angle for gas foil bearings allows for a more symmetrical loading condition. As discussed in [chapter 3](#) this is favourable for the stability of the bearing. This increased stability is one of the main advantages of using gas foil bearings as compared to plain journal bearings. The non-dimensional critical mass for both bearings is plotted in [Figure 4.7](#) where a loss coefficient of  $\gamma_S = 0.4$  is assumed for the GFB. The plot shows a larger critical mass for the gas foil bearing, hinting at an improved dynamic performance compared to the rigid bearing. It is noted, however, that this figure should only be interpreted in a qualitative sense given the inaccuracy in the computed bearing impedances for the GFB as discussed in the previous section.

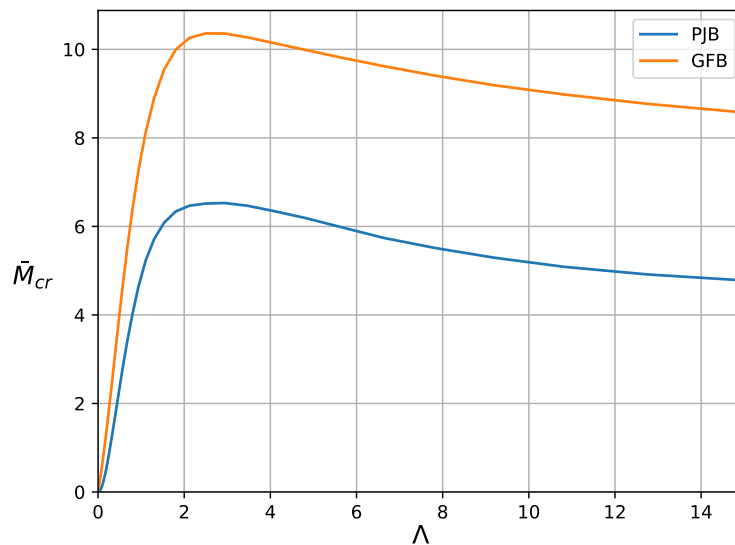


Figure 4.7: Non-dimensional critical mass as a function of bearing speed number  $\Delta$  for a PJB and a GFB.

### 4.3. Application to the ORCHID turbine

The feasibility of applying gas foil bearings to support the rotor of a mini-ORC turbine is finally investigated. The laboratory mini-ORC turbine of interest is used in the Organic Rankine Cycle Hybrid Integrated Device (ORCHID) at the TU Delft. The working fluid of the turbine is siloxane MM and in order to prevent contamination of the organic fluid in the thermodynamic cycle this will also be used as a lubricant in the bearing. Note that this research only considers the application of journal bearings and the use of gas foil thrust bearings is to be investigated further in future work. At design conditions, the thermodynamic state in the bearing compartment is assumed to be defined by  $P_r = 0.94$  and  $T_r = 1.1$  corresponding to the turbine inlet conditions. This thermodynamic state is shown in the reduced T-s plane along with the contours of the generalized isentropic pressure-volume exponent in Figure 4.8.

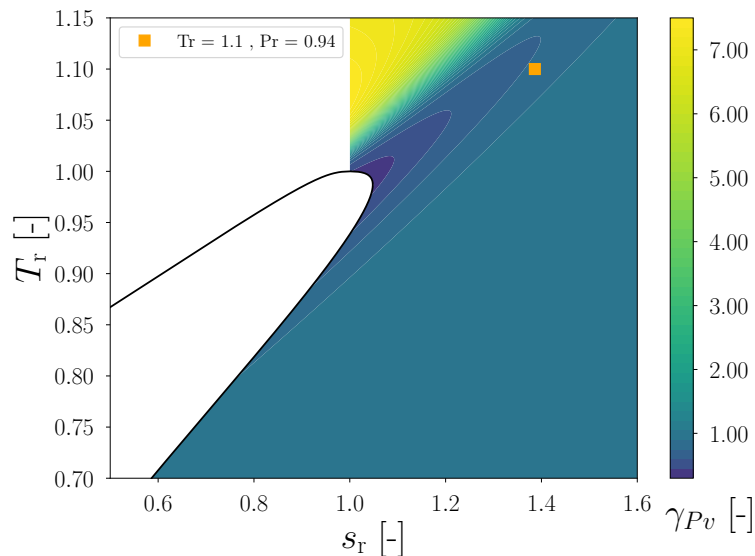


Figure 4.8: Assumed bearing operating conditions for siloxane MM for operation with the ORCHID turbine plotted on the reduced T-s thermodynamic plane.

The rotational speed of the rotor is 98000 rotations per minute. The dimensions of the gas foil bearing are set to allow compatibility with the mini-ORC turbine. Initially, the compliance ratio is set to 0.4 as this provides a reasonable starting point for the current analysis. This compliance ratio can, however, be tuned for improved performance in future work. The nominal bearing clearance is assumed to be  $h_0 = 31.8 \mu\text{m}$ . This nominal bearing clearance is partially dependent on the accuracy of the manufacturing of the bearing and the value chosen here is taken equal to existing GFBs presented in literature.[5] The geometry and operating conditions used for the simulations are summarized in Table 4.2.

Parameter	Value
Lubricant	Siloxane MM
Reduced Pressure, $P_r$	0.94
Reduced Temperature, $T_r$	1.10
Bearing Radius, $R$	5 mm
Bearing Width-to-Diameter Ratio, $L/D$	1
Nominal Bearing Clearance	31.8 $\mu\text{m}$
Design Rotational Speed, $\Omega$	98000 RPM
Compliance Ratio, $S$	0.4

Table 4.2: Bearing geometry and design operating conditions of the ORCHID turbine.

Using the data presented in the table, the bearing compressibility number is found to be  $\Lambda = 0.01$ .

The low value of the bearing speed number is a direct result of the relatively high pressure of the lubricant in combination with the small size of the considered bearing. The consequence is potentially low stability of the rotor supported by gas dynamic bearings. The Mach number based on the peripheral speed is given as  $M_U = 0.39$  at the reference thermodynamic state and design rotational speed. In order to check the validity of the assumptions used in the derivation of the compressible Reynolds equation the product of the Grüneisen parameter, the Mach number squared and the Prandtl number is shown in Figure 4.9a. The figure shows that the effect of thermal expansions is negligible at operating conditions sufficiently far away from the thermodynamic critical point. Furthermore, the assumption of constant density over the film thickness is valid away from the critical point as well as shown by the ratio of specific heats in Figure 4.9b.

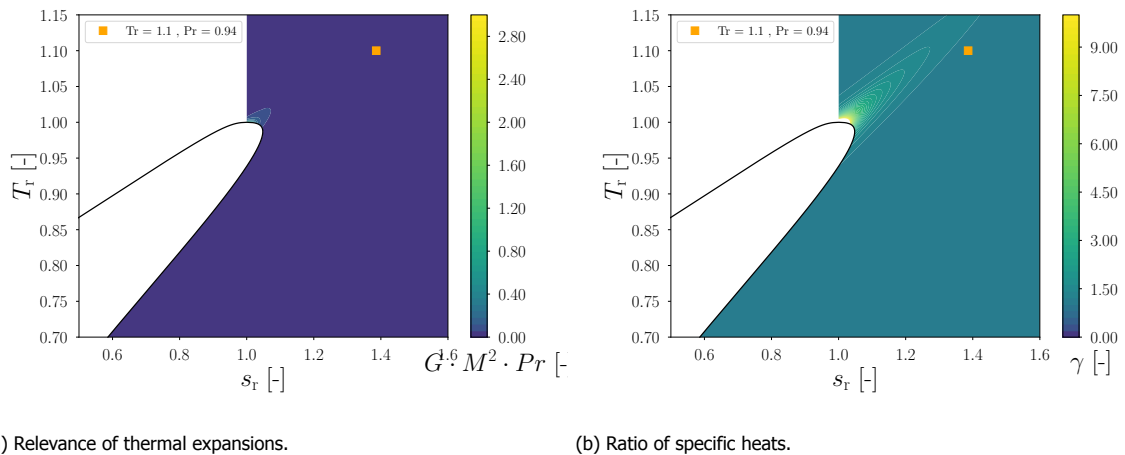


Figure 4.9: Plot showing the validity of the assumptions of the compressible Reynolds equation for the GFB operating with siloxane MM at 98000 RPM.

Under the aforementioned conditions, the steady-state bearing performance is computed. The results are shown in Figure 4.10. The flow regime is considered turbulent and the Reynolds number based on the nominal bearing clearance is calculated as  $Re = 11045$  which is within the range of validity of the turbulence correction factors of Constantinescu.

The bearing load capacity is plotted as a function of journal eccentricity ratio in Figure 4.10a for rotational speed of 30000 RPM, 60000 RPM and the design condition of 98000 RPM. Note that the eccentricity ratio can be increased beyond a value of one particularly for larger rotational speeds as this will generate the required pressure in the gas film to deflect the bump foil.

The minimum film thickness is plotted against load capacity in Figure 4.10b for the same rotational speeds. At design rotational speed, the maximum estimated load capacity is in the order of 20N. Although the exact mass of the rotor is not known it is assumed to stay below 1kg. If this will be the case, the figures indicate sufficient load capacity at design speed considering that the rotor would be carried by two gas foil journal bearings.

Finally, the attitude angle is plotted against load capacity in Figure 4.10c. A steep drop of attitude angle is shown with increased loading as expected. This reduction of the attitude angle is favourable for bearing stability as discussed in previous sections.

The plots of the steady-state load capacity against journal eccentricity, minimum film thickness and attitude angle show the potential of using a gas foil journal bearing to support the rotor of a mini-ORC turbine. Further investigation will be required, however, to accurately predict the critical mass and stability of the rotor-bearing system. The critical mass is not plotted since the values might be inaccurate as discussed. It should also be noted that the gas foil bearing considered in this section is of very small size. The feasibility of manufacturing such bearings should be taken into account in further analysis and design work. Finally, in order to optimize the design, parameters like the compliance ratio might be varied to yield larger load capacity and critical mass as well as to reduce windage power losses.

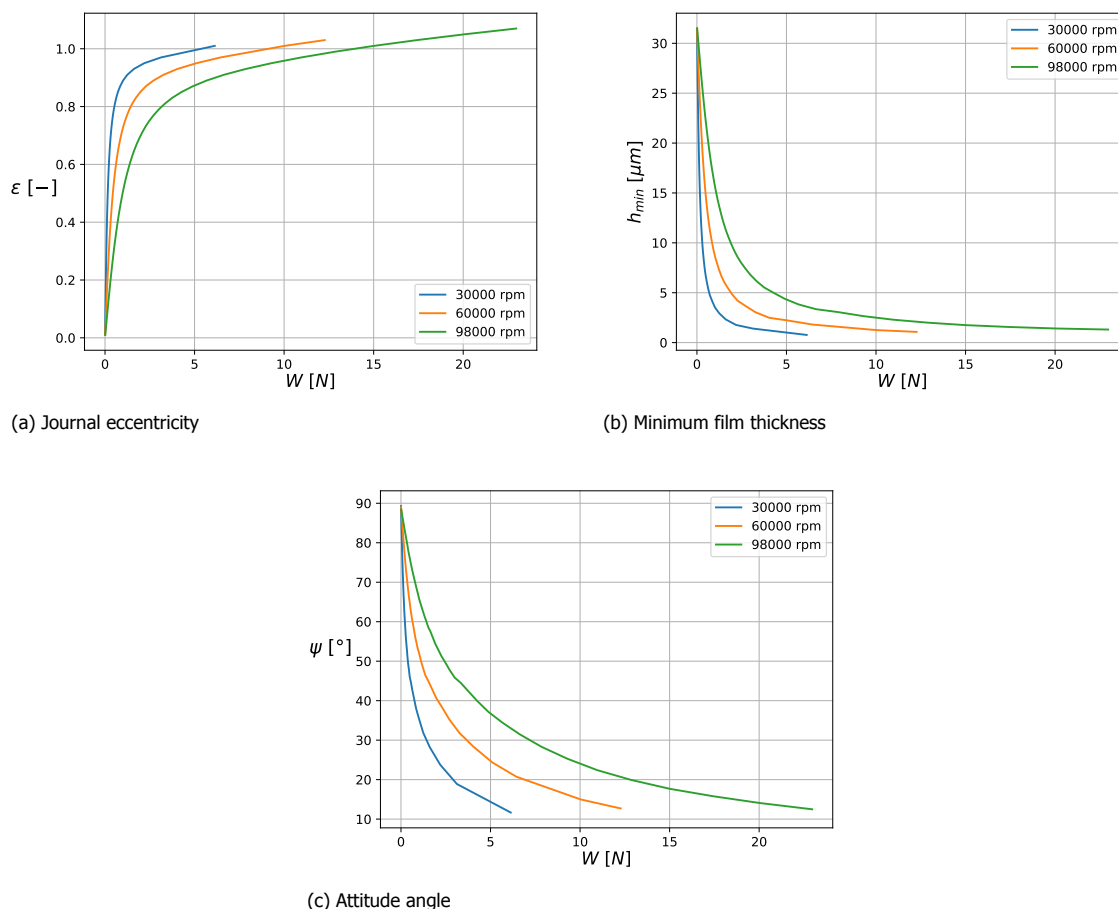


Figure 4.10: Journal eccentricity, minimum film thickness and attitude angle versus load capacity for a gas foil journal bearing with suitable dimensions for operation with the ORCHID turbine.

## 4.4. Chapter Conclusion

In this chapter, the numerical models predicting the performance of gas foil bearings have been discussed. The models have been verified using the numerical results of Kim and San Andrés for heavily loaded gas foil bearings lubricated with ambient pressure air.[5] Although the steady-state performance parameters match well with the reference data, there seems to be a bug in the part of the code calculating the stiffness and damping coefficients. Results of a first-generation gas foil bearing have been compared with a plain journal bearing of equal size. Both bearings exhibit approximately equal load capacities as also indicated in scientific literature. A significant increase in load capacity of the gas foil bearing can, however, be obtained by tailoring the bump foil stiffness in future work. The attitude angle of gas foil bearings appears to be significantly smaller which is favourable for rotor-dynamic stability. The numerical model has finally been applied to compute the steady-state performance that can be obtained if the technology is used to support the ORCHID turbine. A load capacity of up to 20N is predicted for a single gas foil journal bearing at design operating conditions. It should be noted that no attempt was made to optimize the current design of the bearing. Furthermore, the analysis of the rotor-dynamic stability and the thrust bearings should be considered in future work.



# 5

## Conclusion & Recommendations

### 5.1. Conclusion

The work documented in this dissertation investigated the performance of gas dynamic bearings lubricated with non-ideal compressible flows. To this end, a sophisticated numerical model has been developed to solve the steady-state Reynolds equation for three-dimensional, turbulent lubricating flows leading to the prediction of the bearing load capacity. By means of a perturbation method, the perturbed density field was obtained leading to the definition of the linearized stiffness and damping coefficients and the rotor-dynamic critical mass. The influence of non-ideal thermodynamic effects was analysed in a conceptual way by means of non-dimensional numbers. Finally, the effect of structural compliance has been introduced, leading to the prediction of the steady-state load capacity of a gas foil bearing suitable for operation with the ORCHID turbine. The main conclusions drawn from this research are listed below:

- Gas dynamic bearings operating within the dense gas or supercritical flow regime are characterized by high pressures leading to low bearing speed numbers ( $\Lambda$ ). This leads to an increased significance of pressure-induced flow or Poiseuille flow within the bearing. The result is a limited non-dimensional load capacity and critical mass.
- The effect of non-ideal thermodynamic properties of the fluid on the non-dimensional load capacity is mainly characterized by the non-dimensional bulk modulus of the fluid. Increased fluid compressibility leads to a non-dimensional bulk modulus below one ( $\bar{\beta} < 1$ ). This lowers the peak pressures within the gas film, resulting in reduced load capacity as compared to ideal gas lubrication flows.
- The effect of non-ideal thermodynamic properties of the fluid on the bearing non-dimensional critical mass is mainly characterized by the non-dimensional bulk modulus of the fluid as well. For compressible flows with  $\bar{\beta} < 1$ , low bearing speed numbers lead to an increased non-dimensional critical mass as compared to ideal gas flows. Large bearing speed numbers lead to a decreased non-dimensional critical mass compared to ideal gas flows. This effect is opposite for fluid flows with  $\bar{\beta} > 1$ .
- The effect of different working fluids has been analysed for bearings operating at equal film thickness distribution and bearing speed numbers. For non-ideal compressible flows under these conditions, the effect of different working fluids is introduced through variations in the non-dimensional bulk modulus and dynamic viscosity. The iso-thermal variations in non-dimensional dynamic viscosity, however, have negligible influence for practical bearing speed numbers of  $\Lambda < 5$ . There is no effect of different working fluids for ideal gas flows under the given conditions.
- The effects of turbulence on lubrication flows have been considered. Turbulence at increased Reynolds numbers tends to resist the pressure-induced Poiseuille flow in the thin film. This leads to larger pressure peaks and larger non-dimensional load capacity compared to laminar flows, particularly at low bearing speed numbers. The non-ideal thermodynamic effects are more pronounced for increased Reynolds numbers as a result of the larger pressure peaks.

- The performance of a first-generation gas foil bearing has been compared to a plain journal bearing. Siloxane MM at a reduced pressure of  $P_r = 0.8$  and a reduced temperature of  $T_r = 1.1$  was used as a lubricant considering a nominal bearing clearance of  $h_0 = 21.8\mu m$ . Both bearings exhibit approximately equal load capacities as a function of minimum film thickness and bearing speed number. The gas foil bearing operates at an attitude angle up to  $30^\circ$  lower at low bearing speed numbers. This indicates the potential increase in bearing stability with respect to plain journal bearings.
- Results obtained using the computational model show the potential feasibility of applying gas foil bearings to support the rotor of the ORCHID turbine in terms of steady-state load capacity. At design operating conditions, the gas foil bearing considered shows a predicted maximum load capacity of up to  $20N$ .

## 5.2. Recommendations

The present work has aimed to address the knowledge gap related to the application of gas dynamic bearings and gas foil bearings in particular for systems operating at high pressures and with non-conventional working fluids in ideal and non-ideal thermodynamic conditions. Some recommendations are presented for future work related to the developed computational tool and in particular to the analysis of gas foil bearings for application with the ORCHID turbine:

- The implementation of the numerical method for obtaining the stiffness and damping coefficients for gas foil bearings should be re-evaluated. The discrepancy of the results compared to data from scientific literature as presented in [chapter 4](#) should be understood and addressed.
- The critical mass should be analysed for a gas foil journal bearing of appropriate dimensions for operation with the ORCHID turbine. The present work shows the potential of gas foil bearings in terms of increased stability as compared to rigid bearings. The bearing stability will remain, however, an important design constraint that is likely to be more stringent than bearing load capacity.
- The power loss within the gas (foil) bearing should be analysed for turbulent lubricating flows. As discussed in this manuscript, experimental results show a strong increase in power loss for high-pressure lubricants which could be detrimental to the system performance.
- More advanced design configurations of gas foil bearings should be investigated in an attempt to improve bearing load capacity and stability. Examples include the variation of structural stiffness in circumferential and axial directions, including a bearing pre-load or combining the advantages of gas foil bearings and grooved dynamic bearings as was presented by Guenat.[11]
- The potential inclusion of thermal effects within the modelling might be considered. As mentioned, viscous dissipation can be significant for high-pressure fluids leading to non-negligible temperature effects and thermal expansions of the fluid and/or structure.
- The computational tool could be extended to allow performance predictions of gas foil thrust bearings capable of supporting axial loads on the rotors. To this end, the Reynolds equation can be converted to cylindrical coordinates and the appropriate boundary conditions are to be selected.
- The implementation of the bearing models in the design process of the turbomachinery and rotor components should be investigated further. Optimal system performance might be obtained by considering an integrated design approach. To this end, the computational cost of the numerical tools discussed in this work should be reduced or the application of model order reduction techniques might be considered.

# Bibliography

- [1] P. Colonna, E. Casati, C. Trapp, T. Mathijssen, J. Larjola, T. Turunen-Saaresti, and A. Uusitalo, *Organic Rankine Cycle Power Systems: From the Concept to Current Technology, Applications, and an Outlook on the Future*, *Journal of Engineering for Gas Turbines and Power* **137(10)**, 100801 (2015).
- [2] L. San Andrés and T. H. Kim, *Analysis of gas foil bearings integrating FE top foil models*, *Tribology International* **42(1)**, 111 (2009).
- [3] A. Giuffré and M. Pini, *NiceProp: An interactive Python-based educational tool for non-ideal compressible fluid dynamics*, *SoftwareX* **17**, 100897 (2022).
- [4] École Polytechnique Fédérale de Lausanne, *Herringbone Grooved Journal Bearing*, <https://www.epfl.ch/labs/lamd/research/bearings/> (2021), accessed: January 20, 2023.
- [5] L. San Andrés and T. Ho Kim, *Heavily Loaded Gas Foil Bearings: A Model Anchored to Test Data*, *Journal of Engineering for Gas Turbines and Power* **130(1)**, 012504 (2008).
- [6] European Commission Directorate-General for Research and Innovation, *Fly the Green Deal: Europe's Vision for Sustainable Aviation*, Tech. Rep. 978-92-76-43368-2 (Publications Office of the European Union, Brussels, Belgium, 2022).
- [7] T. Kadyk, R. Schenkendorf, S. Hawner, B. Yildiz, and U. Römer, *Design of Fuel Cell Systems for Aviation: Representative Mission Profiles and Sensitivity Analyses*, *Frontiers in Energy Research* **7**, 35 (2019).
- [8] D. D. Fuller, *A Review of the State-of-the-Art for the Design of Self-Acting Gas-Lubricated Bearings*, *Journal of Lubrication Technology* **91(1)**, 1 (1969).
- [9] C. DellaCorte, K. C. Radil, R. J. Bruckner, and S. A. Howard, *Design, Fabrication, and Performance of Open Source Generation I and II Compliant Hydrodynamic Gas Foil Bearings*, *Tribology Transactions* **51(3)**, 254 (2008).
- [10] T. Conboy, S. Wright, J. Pasch, D. Fleming, G. Rochau, and R. Fuller, *Performance Characteristics of an Operating Supercritical CO<sub>2</sub> Brayton Cycle*, *Journal of Engineering for Gas Turbines and Power* **134(11)**, 111703 (2012).
- [11] E. P. Guenat, *Advanced design methods and non-ideal gas lubrication applied to aerodynamic bearings*, Ph.D. thesis, École Polytechnique Fédérale de Lausanne, Lausanne, Switzerland (2020).
- [12] B. Dykas, R. J. Bruckner, C. DellaCorte, B. Edmonds, and J. Prael, *Design, Fabrication, and Performance of Foil Gas Thrust Bearings for Microturbomachinery Applications*, *Journal of Engineering for Gas Turbines and Power* **131(1)**, 012301 (2008).
- [13] O. Reynolds, *IV. On the theory of lubrication and its application to Mr. Beauchamp tower's experiments, including an experimental determination of the viscosity of olive oil*, *Philosophical Transactions of the Royal Society A* **177**, 157 (1886).
- [14] T. M. Conboy, *Real-Gas Effects in Foil Thrust Bearings Operating in the Turbulent Regime*, *Journal of Tribology* **135(3)**, 031703 (2013).
- [15] D. Kim, *Design Space of Foil Bearings for Closed-Loop Supercritical CO<sub>2</sub> Power Cycles Based on Three-Dimensional Thermohydrodynamic Analyses*, *Journal of Engineering for Gas Turbines and Power* **138(3)**, 032504 (2015).

- [16] S. Y. Chien, M. S. Cramer, and A. Untaroiu, *Compressible Reynolds equation for high-pressure gases*, *Physics of Fluids* **29(11)**, 116101 (2017).
- [17] E. M. Greitzer, C. S. Tan, and M. B. Graf, *Internal Flow: Concepts and Applications*, Cambridge Engine Technology Series (Cambridge University Press, Cambridge, 2004).
- [18] R. J. Bruckner, *Windage Power Loss in Gas Foil Bearings and the Rotor-Stator Clearance of High Speed Generators Operating in High Pressure Environments*, Proceedings of the ASME Turbo Expo 2009: Power for Land, Sea, and Air, Vol. Volume 5: Microturbines and Small Turbomachinery; Oil and Gas Applications (Orlando, Florida, USA, 2009).
- [19] V. N. Constantinescu, *On Turbulent Lubrication*, *Proceedings of the Institution of Mechanical Engineers* **173(1)**, 881 (1959).
- [20] A. Z. Szeri, *Fluid Film Lubrication*, (Cambridge University Press, Cambridge, 2010) Chap. 7 - Turbulence, pp. 254–284, 2nd ed.
- [21] J. Durany, J. Pereira-Pérez, and F. Varas, *About the Constantinescu turbulent model in hydrodynamic lubrication: A comparison with 3-D LES models*, *Tribology International* **83**, 33 (2015).
- [22] J. W. Lund, *Calculation of Stiffness and Damping Properties of Gas Bearings*, *Journal of Lubrication Technology* **90(4)**, 793 (1968).
- [23] E. P. Guenat and J. Schiffmann, *Real-gas Effects on Aerodynamic Bearings*, *Tribology International* **120**, 358 (2018).
- [24] C. Bi, D. Han, and J. Yang, *The Frequency Perturbation Method for Predicting Dynamic Coefficients of Supercritical Carbon Dioxide Lubricated Bearings*, *Tribology International* **146**, 106256 (2020).
- [25] H. Heshmat, J. A. Walowit, and O. Pinkus, *Analysis of Gas-Lubricated Foil Journal Bearings*, *Journal of Tribology* **105(4)**, 647 (1983).
- [26] M. Carpino and G. Talmage, *A Fully Coupled Finite Element Formulation for Elastically Supported Foil Journal Bearings*, *Tribology Transactions* **46(4)**, 560 (2003).
- [27] C. H. T. Pan and D. Kim, *Stability Characteristics of a Rigid Rotor Supported by a Gas-Lubricated Spiral-Groove Conical Bearing*, *Journal of Tribology* **129(2)**, 375 (2007).
- [28] J. Schiffmann and S. Spakovszky, *Foil Bearing Design Guidelines for Improved Stability*, *Journal of Tribology* **135(1)**, 011103 (2013).
- [29] M. T. C. Faria and L. San Andrés, *On the Numerical Modeling of High-Speed Hydrodynamic Gas Bearings*, *Journal of Tribology* **122(1)**, 124 (2000).
- [30] E. W. Lemmon, I. H. Bell, M. L. Huber, and M. O. McLinden, *NIST Standard Reference Database 23: Reference Fluid Thermodynamic and Transport Properties-REFPROP, Version 10.0*, National Institute of Standards and Technology, (2018).
- [31] I. H. Bell, J. Wronski, S. Quoilin, and V. Lemort, *Pure and Pseudo-pure Fluid Thermophysical Property Evaluation and the Open-Source Thermophysical Property Library CoolProp*, *Industrial & Engineering Chemistry Research* **53(6)**, 2498 (2014).
- [32] W. Sutherland, *LII. The viscosity of gases and molecular force*, *The London, Edinburgh, and Dublin Philosophical Magazine and Journal of Science* **36(223)**, 507 (1893).

# Appendices





## Link to the Python Repository

The numerical solver developed during this research is a Python-based computational tool that discretizes the partial differential equations and solves the associated systems of equations. The code is contained in a GitHub repository which can be found using the following link:

<https://github.com/Wesseldewaart/GasBearingSim.git>

In order to gain access to the GitHub repository please contact Dr. Ir. Matteo Pini (M.Pini@tudelft.nl) or Wessel de Waart (wesseldewaart@gmail.com).

The code is written in Python 3.6 and has the following pre-requisites:

- NumPy
- SciPy
- Pandas
- Matplotlib
- tqdm
- tkinter
- CoolProp
- RefProp (optional, for certain fluids)

The code is run from the 'GBSmain' script. This will open up a graphical user interface in which the various bearing properties of interest can be entered. Alternatively, the bearing properties can be read from a configuration file by checking the box 'Input from configuration file' in the graphical user interface. A number of predefined configuration files are included in the 'Input' folder of the repository.